Doctorado en Oceanografía y Cambio Global
Universidad de Las Palmas de Gran Canaria

Tesis Doctoral

Shelf circulation, hydrography and chlorophyll-a variability northwest of the Antarctic Peninsula

Marta Veny López

Las Palmas de Gran Canaria, Marzo de 2025

UNIVERSIDAD DE LAS PALMAS DE GRAN CANARIA

ESCUELA DE DOCTORADO

Programa de doctorado en Oceanografía y Cambio Global.

Título de la Tesis: Shelf circulation, hydrography and chlorophyll-a variability northwest of the Antarctic Peninsula.

Tesis Doctoral presentada por Dª Marta Veny López.

Dirigida por el Dr. D Miguel Borja Aguiar González y por la Dra. Dª María de los Ángeles Marrero Díaz.

Las Palmas de Gran Canaria, a 11 de marzo de 2025.

Los Directores, La Doctoranda,

A tots es meus,

Agradecimientos

Acknowledgements

El momento de redactar esta tesis parecía algo lejano. Cada vez que me preguntaban "¿y cuándo terminas?", solía responder "falta mucho, en 2025", pero de repente… Aquí estamos.

En primer lugar, quería agradecer a mis directores, Borja Aguiar González y Ángeles Marrero Díaz, y a mi tutor, Ángel Rodríguez Santana, por querer guiarme y ayudarme para poder llevar a cabo esta tesis. Quién iba a imaginar que aquella estudiante de máster que entró al despacho alucinada con el tema antártico iba a terminar escribiendo su tesis sobre ello. Gracias a todos de corazón por ayudarme a abrir paso a mi carrera como investigadora. Y, Borja, gracias por no soltarme nunca la mano. Este logro también es tuyo.

Además, me gustaría dar las gracias a todos los que me acogieron durante mis estancias de investigación. A Sheila Natalí Estrada Allis y a Julio Sheinbaum Pardo, por recibirme en México con una calidez y humanidad que reflejan lo mejor de su país, así como por compartir su excelente manera de trabajar en este ámbito. A Simón Ruiz Valero y a Bàrbara Barceló Llull, gracias por acogerme en nuestra isla y hacerme sentir una más del equipo; el cariño y la cercanía de casa son inigualables. A Tammy Morris, Els Vermeulen y Mia Wege por hacer de Sudáfrica un lugar donde me sentí bienvenida desde el primer día, thank you for your kindness and warmth.

A toda mi familia, por ser un pilar incondicional durante todos estos años. Especialment a tu, padrinet. A mis padres y a mi hermana, por estar siempre ahí cuando regreso, recordándome que no quieren que me vaya más, y preguntándome: “¿Cuándo vuelves? O mejor nos vamos contigo a vivir en Playa Chica”. Y a los míos, quienes siempre tenían un buen plan al volver a casa y me recibían como si el tiempo no pasara y la distancia no existiera. Pero sin olvidarme del grupo de

cabras, un buen equipo canario adoptando a una gallega y una mallorquina, la mejor combinación.

A Cris, Tania, Dani, David, Neus, Javi, Pepelu, Kevin, Natalia, Diego, Nacho… Los que hicieron los días mucho más amenos, con pausas para un café o simplemente una charla. Aunque no podemos negar que los mejores planes siempre eran fuera de la universidad; esos momentos juntos sabían aún mejor, ya fuera en la playa o con una cervecita en la mano. Cris, tampoc no ho hauria pogut fer sense tu; aquest camí, de la mà, ha estat molt més senzill i agradable compartit. No saps com em fa de feliç tenir-te al meu costat per sempre. Y Tania, no sabes la ilusión que fue tu unión al grupo, el cual ha ido creciendo con Alex, Marina, Laia… Gracias por quedarte, por tu ayuda en los momentos más críticos, por darlo todo y ser tan buena. Ahora te quedas con el relevo de veterana, ¡te lo ganaste!

També a tu, cuquet. Per voler estar a n'es meu costat i tenir casa nostra, junts. Gràcies per acompanyar-me durant tot aquest camí. Hem viscut increïbles experiències, aquí i a moltes parts del món. No hagués estat tan fàcil sense el teu suport i confiança en mi. A per moltes més aventures!

Abstract

This doctoral thesis investigates the physical and ecological dynamics of the Bransfield Strait (BS), a complex marine system located between the Bellingshausen and Weddell seas. The strait is characterized by two coastal currents that transport different water masses and converge along the Peninsula Front (PF). The Bransfield Current (BC) flows northeastward along the southern slope of the South Shetland Islands (SSI), transporting stratified, less saline, and warmer Transitional Zonal Water with Bellingshausen influence (TBW). In contrast, the Antarctic Coastal Current (CC) flows southwestward along the northern slope of the Antarctic Peninsula (AP), transporting well-mixed, colder, and saltier Transitional Zonal Water with Weddell influence (TWW).

Using a multidisciplinary approach that combines *in situ* observations, remotely sensed data, global ocean reanalysis products, and climatological analyses, this work explores the interplay between boundary currents, interbasin exchanges, and ecological dynamics in response to regional environmental variability.

The first component of this thesis provides the first observational-based assessment of the BC as a year-round, surface-intensified coastal jet. SADCP (Shipboard Acoustic Doppler Current Profiler) velocity measurements from 375 cruises between 1999 and 2014 reveal that the BC maintains a consistent northeastward flow, with core velocities reaching 60 cm s^{-1} in summer and approximately 40 cm s^{-1} in other seasons, extending to depths of 200–250 m. Upstream of Nelson Strait, the BC exhibits seasonal variability in volume transport integrated between 30 and 250 m, peaking at 0.93 ± 0.15 Sv during summer and reducing to 0.50 ± 0.04 Sv in winter. Downstream, transport remains relatively consistent at 1.31 ± 0.20 Sv, driven by inflows through Nelson Strait.

The second component examines the spatiotemporal variability of the BC and CC using 30 years of remotely sensed observations. The BC consistently strengthens downstream, with transport in the first 100 m showing a seasonal range of 0.24–0.33 Sv in the western transect, increasing to 0.52–0.64 Sv in the eastern transect in the BS. In contrast, the CC weakens downstream, with transport showing a seasonal range of 0.19–0.38 Sv in the western transect, and decreasing to 0.05–0.33 Sv in the eastern transect in the BS, indicating stronger transport upstream. Heat transport analyses show the BC contributes up to 5.44×10^{12} W eastward in summer (0–100 m depth), while the CC peaks at 2.13×10^{12} W westward. During winter, net heat transport approaches zero, driven by homogenous temperatures and sea ice coverage. The evaluation of two global ocean reanalysis products (GLORYS12V1 and HYCOM) reveals their inability to accurately represent the BS circulation. This underscores the importance of high-resolution observational data and improved models to better resolve boundary current dynamics in this region.

The final component focuses on the seasonal variability of chlorophyll-a (chl-a) blooms in the BS, based on remotely sensed observations from 1998 to 2018. Phytoplankton dynamics are strongly influenced by the PF, effectively delineating two distinct ecological niches: the TBW and TWW pools. The summer climatological PF aligns with the 0.6°C isotherm and the 0.5 mg m^{-3} chl-a isoline, defining zones of peak phytoplankton productivity around the SSI. This framework underscores the PF's role in shaping seasonal and interannual phytoplankton variability.

These findings provide a detailed baseline for understanding the processes driving boundary current dynamics and their influence on hydrography, sea ice, and marine Antarctic ecology in the AP region. By integrating sea surface temperature, velocity, and chl-a data, this work highlights the importance of high-resolution observations and remote sensing to monitor the interconnected physical and biological processes in this climatically sensitive region.

Resumen

Esta tesis doctoral investiga la dinámica física y ecológica del Estrecho de Bransfield (BS), un complejo sistema marino ubicado entre los mares de Bellingshausen y Weddell. El estrecho se caracteriza por dos corrientes costeras que transportan diferentes masas de agua y convergen a lo largo del Frente de Península (PF). La Corriente de Bransfield (BC) fluye hacia el noreste a lo largo de la pendiente sur de las Islas Shetland del Sur (SSI), transportando agua zonal transicional estratificada, menos salina y más cálida con influencia de Bellingshausen (TBW). En contraste, la Corriente Antártica Costera (CC) fluye hacia el suroeste a lo largo de la pendiente norte de la Península Antártica (AP), transportando agua zonal transicional bien mezclada, más fría y salina con influencia de Weddell (TWW).

Utilizando un enfoque multidisciplinario que combina observaciones *in situ*, datos satelitales, productos de reanálisis oceánicos globales y análisis climatológicos, este trabajo explora la interacción entre las corrientes de frontera, los intercambios entre cuencas y la dinámica ecológica en respuesta a la variabilidad ambiental regional.

El primer componente de esta tesis proporciona la primera evaluación basada en observaciones de la BC como un *jet* costero intensificado en la superficie durante todo el año. Las mediciones de velocidad de SADCP (Perfilador Acústico de Corrientes por Efecto Doppler a Bordo) en 375 campañas entre 1999 y 2014 revelan que la BC mantiene un flujo consistente hacia el noreste, con velocidades máximas que alcanzan los 60 cm s^{-1} en verano y en torno a 40 cm s^{-1} en otras estaciones, extendiéndose hasta profundidades de 200-250 m. Corriente arriba del estrecho de Nelson, la BC presenta variabilidad estacional en el transporte de volumen integrado entre 30 y 250 m, alcanzando un máximo de 0.93 ± 0.15 Sv durante el verano y reduciéndose a 0.50 ± 0.04 Sv en invierno. Corriente abajo, el

transporte se mantiene relativamente constante en 1.31 ± 0.20 Sv, impulsado por los flujos a través del estrecho de Nelson.

El segundo componente examina la variabilidad espaciotemporal de la BC y la CC utilizando 30 años de datos satelitales. La BC se fortalece de manera constante corriente abajo, con un transporte en los primeros 100 m que muestra un rango estacional de 0.24-0.33 Sv en el transecto oeste, aumentando a 0.52-0.64 Sv en el transecto este del BS. En contraste, la CC se debilita corriente abajo, con un transporte que muestra un rango estacional de 0.19-0.38 Sv en el transecto oeste, y disminuye de 0.05-0.33 Sv en el transecto este del BS, indicando un transporte más fuerte corriente arriba. Los análisis de transporte de calor muestran que la BC contribuye hasta 5.44×10^{12} W hacia el este en verano (profundidades de 0-100 m), mientras que la CC alcanza un máximo de 2.13×10^{12} W hacia el oeste. Durante el invierno, el transporte neto de calor se aproxima a cero, impulsado por temperaturas homogéneas y la cobertura de hielo marino. La evaluación de dos productos de reanálisis oceánicos globales (GLORYS12V1 y HYCOM) revela su incapacidad para representar con precisión la circulación del BS. Esto subraya la importancia de los datos observacionales de alta resolución y modelos mejorados para resolver mejor la dinámica de las corrientes de frontera en esta región.

El componente final se centra en la variabilidad estacional de las floraciones de clorofila-a (chl-a) en el BS, basándose en datos satelitales de 1998 a 2018. La dinámica del fitoplancton está fuertemente influenciada por el PF, delimitando eficazmente dos nichos ecológicos distintos: los reservorios de TBW y TWW. El PF climatológico de verano se alinea con la isoterma de 0.6ºC y la isolínea de chl-a de 0.5 mg m^{-3}, definiendo zonas de máxima productividad fitoplanctónica alrededor de las SSI. Este marco resalta el papel del PF en la modelización de la variabilidad fitoplanctónica estacional e interanual.

Estos hallazgos proporcionan una base detallada para entender los procesos que impulsan la dinámica de las corrientes de frontera y su influencia en la hidrografía, el hielo y la ecología marina antártica en la región de la AP. Al integrar datos de temperatura de la superficie del mar, velocidad y chl-a, este trabajo destaca la importancia de las observaciones de alta resolución y datos satelitales para monitorear los procesos físicos y biológicos interconectados en esta región sensible al clima.

Contents

List of Figures

List of Tables

List of Abbreviations

ACC	Antarctic Circumpolar Current
ADCP	Acoustic Doppler Current Profiler
AE	Anticyclonic Eddy
AI	Akademik Ioffe
AOML	Atlantic Oceanographic and Meteorological Laboratory
AP	Antarctic Peninsula, *Península Antártica*
ASV	Akademik Sergeyy Vavilov
BC	Bransfield Current, *Corriente de Bransfield*
BF	Bransfield Front, *Frente de Bransfield*
BS	Bransfield Strait, *Estrecho de Bransfield*
CATS	Circum-Antarctic Tidal Simulation
CC	Antarctic Coastal Current, *Corriente Antártica Costera*
CDW	Circumpolar Deep Water
Chl-a	Chlorophyll-a, *Clorofila-a*
CMEMS	Copernicus Marine Environment Monitoring Service
CODAS	Common Ocean Data Access System
CT	Central Transect
CTD	Conductivity, Temperature and Depth
DAC	Drifter Data Assembly Center
DI	Deception Island
DUACS	Data Unification Altimeter Combination System
ESA CCI	European Space Agency Climate Change Initiative
ET	East Transect
FP	Frontal Probability

GDP	Global Drifter Program
GI	Greenwich Island
GLORYS	GLobal Ocean ReanalYsis and Simulation
GOFS	Global Ocean Forecasting System
GS	Gerlache Strait
HNLC	High-Nutrient Low-Chlorophyll
HYCOM	HYbrid Coordinate Ocean Model
JASADCP	Joint Archive for SADCP
KGI	King George Island
LADCP	Lowered Acoustic Doppler Current Profiler
LI	Livingston Island
LIM	Louvain-la-Neuve-Ice Model
MEOP	Marine Mammals Exploring the Oceans Pole to Pole
NCODA	Navy Coupled Ocean Data Assimilation
NEMO	Nucleus for European Modelling of the Ocean
NI	Nelson Island
NS	Nelson Strait
OI SST	Optimum Interpolation Sea Surface Temperature
OSTIA	Operational Sea Surface Temperature and Ice Analysis, *Análisis Operacional de la Temperatura Superficial del Mar y Hielo*
PF	Peninsula Front, *Frente de Península*
RI	Robert Island
SADCP	Shipboard Acoustic Doppler Current Profiler, *Perfilador Acústico de Corrientes por Efecto Doppler a Bordo*
SEM	Standard Error of the Mean
SIC	Sea Ice Coverage

SO	Southern Ocean
SSI	South Shetland Islands, *Islas Shetland del Sur*
SST	Sea Surface Temperature, *Temperatura Superficial del Mar*
Sv	Sverdrup
TBW	Transitional Zonal Water with Bellinghausen influence, *Agua Zonal Transicional con influencia de Bellingshausen*
TWW	Transitional Zonal Water with Weddell influence, *Agua Zonal Transicional con influencia de Weddell*
UHDAS	University of Hawaii Data Acquisition System
UML	Upper Mixed Layer
wAP	West of the Antarctic Peninsula
WOD	World Ocean Database
WT	West Transect
XBT	Expendable Bathythermograph

Chapter 1

Introduction

This chapter presents a review of observations, laboratory experiments, and modeling studies from the existing literature on the Bransfield Strait circulation. First, Section 1.1 introduces the most relevant features of the Bransfield Strait, highlighting its oceanographic and ecological importance. Second, Section 1.2 focuses on the oceanography of the Bransfield Strait, divided into two parts: the hydrography and circulation, specifically addressing the two main boundary currents: the Bransfield Current and the Antarctic Coastal Current (Section 1.2.1); and the biophysical coupling occurring within the strait (Section 1.2.2). Last, Section 1.3 outlines the thesis purposes and structure.

1.1 Oceanographic and ecological importance of the Bransfield Strait

Nestled within the Southern Ocean, the Bransfield Strait (BS) emerges as a natural laboratory of unique oceanographic features and profound ecological importance. This narrow channel is situated between the South Shetland Islands (SSI) and the northwest tip of Antarctica (AP; Figure 1.1). The BS plays an essential role in the region's climate dynamics due to its geographic location, serving as a gateway for the exchange of ocean properties driven by water masses of remote origin, mainly, the Bellingshausen and Weddell seas (Grelowski *et al.*, 1986; Hofmann *et al.*, 1996; Zhou *et al.*, 2006; Sangrà *et al.*, 2017), thereby also influencing the Antarctic marine ecosystem (Mura *et al.*, 1995; García-Muñoz *et al.*, 2013; Mendes *et al.*, 2013, 2023; Gonçalves-Araujo *et al.*, 2015; Mukhanov *et al.*, 2021; Costa *et al.*, 2023).

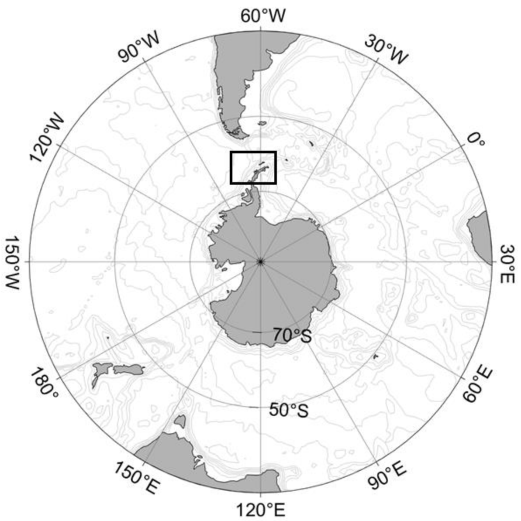

Figure 1.1. Schematic map of the Southern Ocean showing the location of the Bransfield Strait in Antarctica.

Additionally, the BS holds significant implications as a proxy region for observing alterations in the dense water masses of the Weddell Sea shelf due to the limited connections with the surrounding oceans and relatively straightforward access to the strait (Dotto *et al.*, 2016). In this region, substantial inflows of cold water entering from the continental shelf of the Weddell Sea to the BS can be monitored since these water masses act as a crucial precursor to the formation of Antarctic Bottom Water.

Acknowledging the importance of the northwest AP region, encompassing the BS, and conducting comprehensive analyses of these water pathways and their variability are fundamental steps toward obtaining a comprehensive understanding of the climate dynamics within the Southern Ocean. This knowledge is also essential for discerning the region's response to climate change and its broader impact on global climate dynamics.

1.2 Oceanography of the Bransfield Strait

The Bransfield Strait is a dynamic marine region that serves as a key transition zone, connecting the Bellingshausen Sea in the west with the Weddell Sea in the east. The confluence of water masses from distinct origins drives dynamic processes that shape its physical and biological systems.

1.2.1 Hydrography and circulation

Two major inflows—the Bransfield Current (BC) and the Antarctic Coastal Current (CC)— shape the strait's circulation and frontal systems (Figure 1.2; Grelowski *et al.*, 1986; Hofmann *et al.*, 1996; Zhou *et al.*, 2006; Sangrà *et al.*, 2017). The BC, a northeastward coastal jet, transports relatively warm (θ > -0.4ºC; Figure 1.3) and fresh (salinity < 34.45) Transitional Bellingshausen Water (TBW) along the southern slope of the SSI (Figure 1.3). Conversely, the CC flows southwestward along the northern slope of the AP, carrying colder (θ < -0.4ºC) and saltier (salinity > 34.45) Transitional Weddell Water (TWW; Figure 1.3). These water masses interact forming prominent mesoscale features such as the surface Peninsula Front (PF) and the subsurface Bransfield Front (BF), which govern the region's biophysical coupling. The PF, a shallow mesoscale structure (~100 m depth), emerges from the confluence of TBW and TWW, approximately at 20-30 km from the peninsula slope, with a width of 10 km. In contrast, the BF delineates a deeper subsurface boundary (~50–400 m depth), extending from 10 to 20 km along the SSI slope, and is wider and shallower at the beginning of the BC pathway (Sangrà *et al.*, 2011).

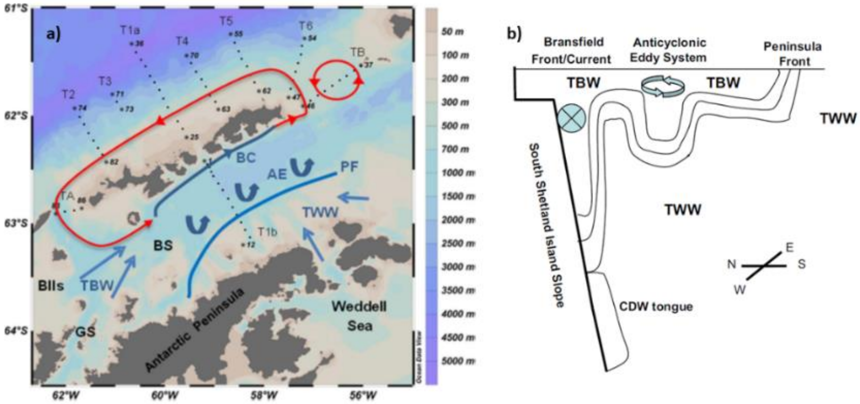

Figure 1.2. a) Location of the CTD stations along the survey transects around the SSI during the COUPLING cruise superposed on the bathymetry of the region (Schlitzer, 2016). Transects and transect end stations are numbered. We have also included a schematic of the Bransfield Current System from Sangrà *et al.*'s (2011) observations in blue; those from this study's observations are in red. SSI is South Shetland Islands; Blls, Bellingshausen Sea; GS, Gerlache Strait; BS, Bransfield Strait. The components of the Bransfield Current system from Sangrà *et al.*'s (2011) are the Peninsula Front (PF), where Transitional Zonal Waters with Bellingshausen Sea and Weddell Sea influence (TBW, TWW) converge, a system of anticyclonic eddies (AE), and the Bransfield Current (BC). [From Sangrà *et al.* (2017) - Figure 1]; and b) Schematics of the main components of the Bransfield Current System along a vertical section crossing the Strait. [From Sangrà *et al.* (2011) - Figure 14].

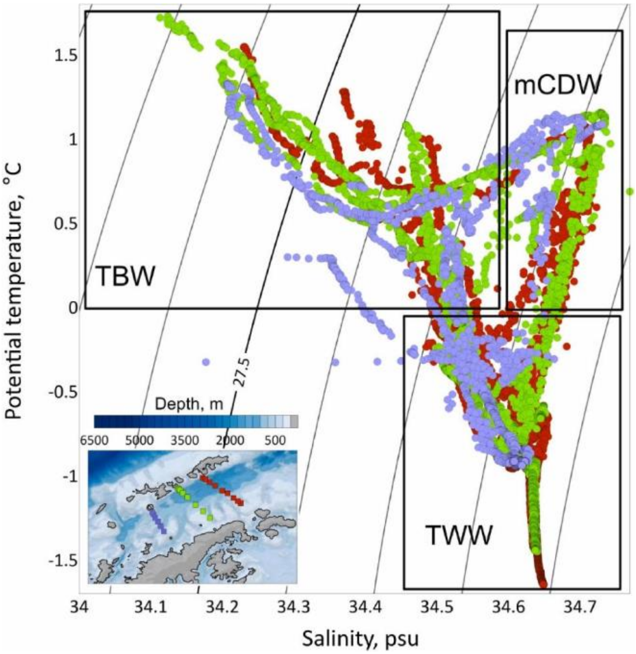

Figure 1.3. Potential temperature-salinity diagram based on the data of CTD transects made in cruise AMK87. Red transect was performed on January 21–23, 2022, green transect was performed on January 24–26, 2022, blue transect was performed on January 26–27, 2022. The boundaries of the water masses indicated by black rectangles are based on (Sangrà *et al.*, 2011; Huneke *et al.*, 2016; Morozov *et al.*, 2021). [From Gordey *et al.* (2024) - Figure 4].

Initially, Niller *et al.* (1991) and Zhou *et al.* (2002, 2006) characterized the BC as a western boundary current driven by a negative wind stress curl and the β-effect within the interior of the strait. However, subsequent *in situ* hydrographic observations and laboratory experiments by Sangrà *et al.* (2011, 2017) revealed that the BC behaves more consistently as a buoyant gravity current (see the experimental set-up in Figure 1.4, and the laboratory simulation in Figure 1.5). Following this reasoning, the less-dense TBW flows along the SSI slope over the denser TWW, confined to a narrow coastal band by both the Coriolis force and a buoyancy-driven pressure gradient.

Expanding on summertime hydrographic data, Sangrà *et al.* (2017) defined the Bransfield Current System, identifying TBW also north of the SSI, which suggests a recirculation pathway of the BC around the SSI, a conclusion further supported by laboratory experiments (see the experimental set-up in Figure 1.6, and the laboratory simulation in Figure 1.7) and surface drifter trajectories (Figure 1.8).

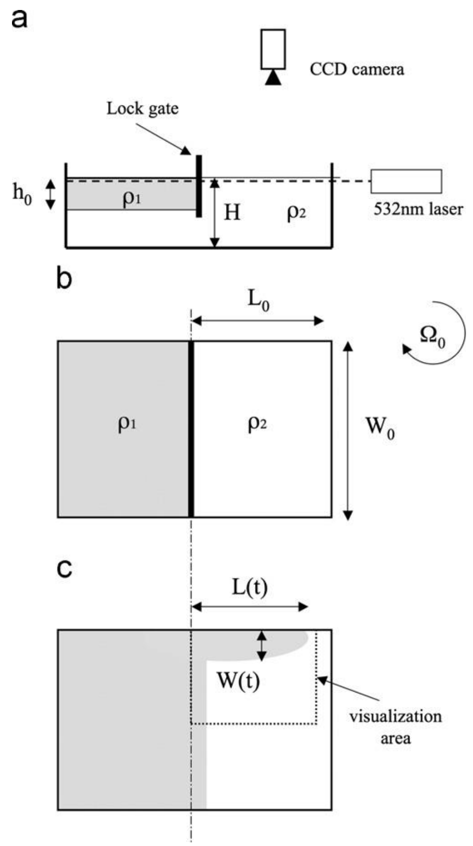

Figure 1.4. Side (a) and top (b) view of the rotating tank experiment. Once the lock-gate is released (c) we measure the typical extension L(t) and the width W(t) of the buoyant coastal current flowing along the wall. The typical width was measured at a fix location in the center of the downstream end (eastern basin). The dotted lines in panel (c) correspond to the visualization area of the CCD camera (shown in Fig. 11). [From Sangrà *et al*. (2011) - Figure 10].

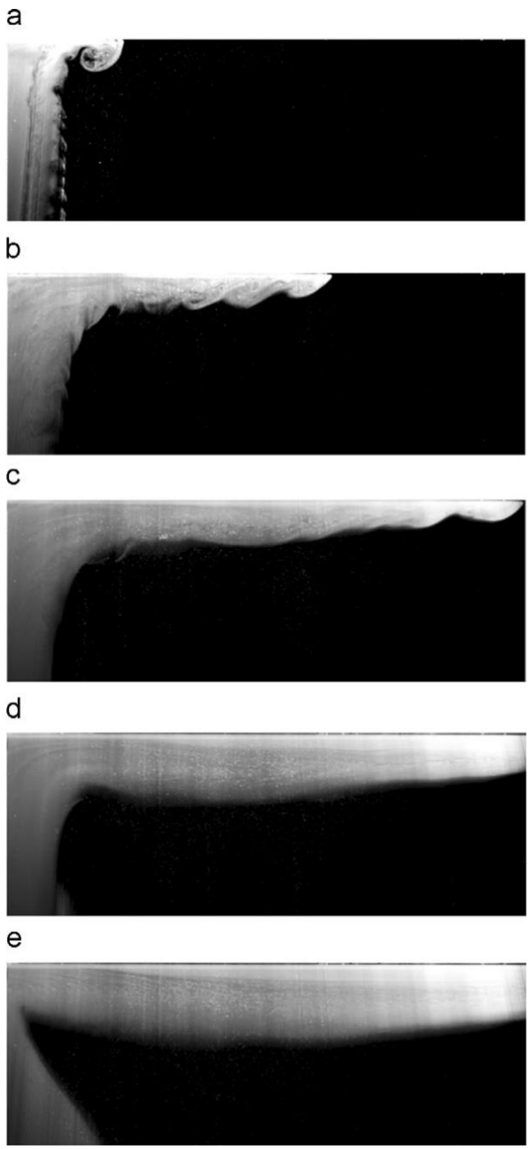

Figure 1.5. Top view visualization, using laser induced fluorescence, of the buoyant coastal current at (a) $t = 0.2T_0$, (b) $t = 0.6T_0$, (c) $t = T_0$, (d) $t = 2T_0$ and (e) $t = 4T_0$, where T_0 is the rotation period. [From Sangrà *et al.* (2011) - Figure 11].

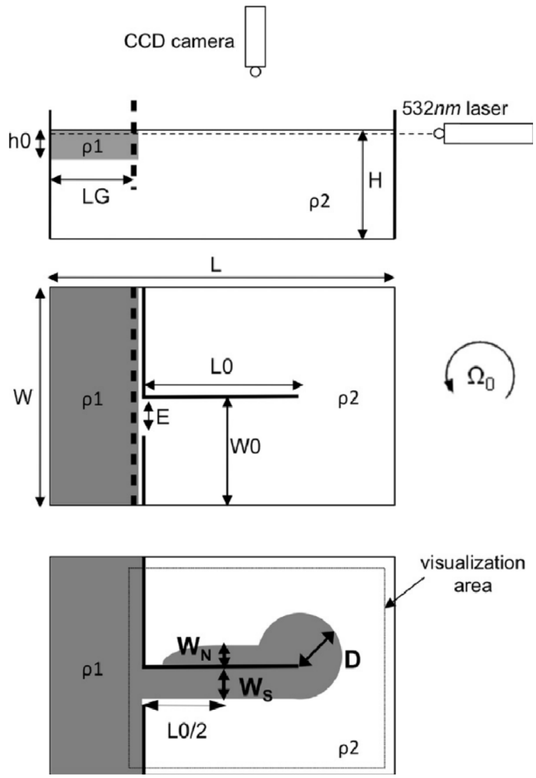

Figure 1.6. Side view and top view of the experimental setup. The grey area corresponds to the light fluid of density ρ_1. Black solid lines correspond to vertical boundaries in the tank, while the black dashed line indicates the position of a lock gate, which is released at the initial time t=0. The southern W_S and the northern W_N widths of the coastal current were measured at mid-distance $L_0/2$=25 cm of the central wall, which mimics the SSI. The extension of the anticyclonic circulation D was measured at 45° north from the wall tip. [From Sangrà *et al.* (2017) - Figure 8].

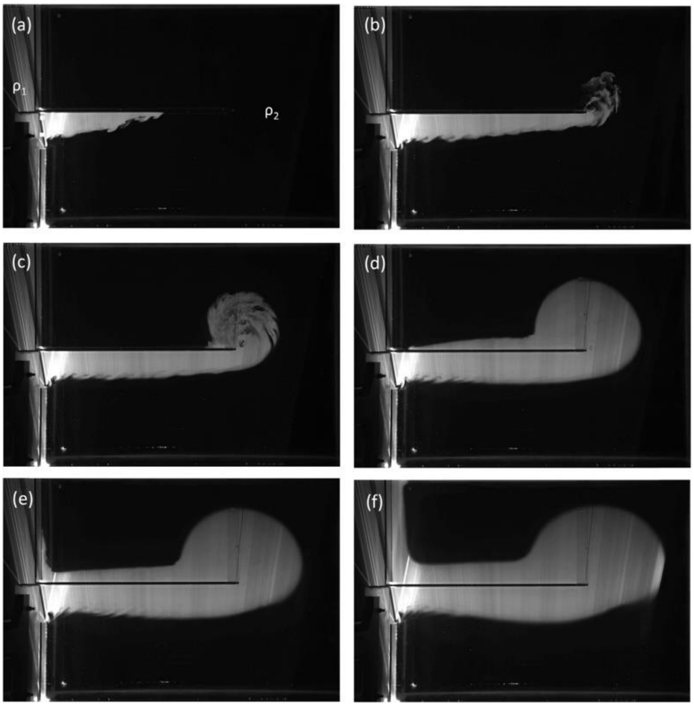

Figure 1.7. LIF visualization of the horizontal extension of the light water of density ρ_1 at (a) 0.33, (b) 0.8, (c) 1.2, (d) 2.2, (e) 2.7 and (f) 3.3 T_0, where T_0=19.8 s is the rotating period of the tank. The baroclinic deformation radius is R_d=7 cm for this experiment, while α=4.1 and λ=0.43. [From Sangrà *et al*. (2017) - Figure 9].

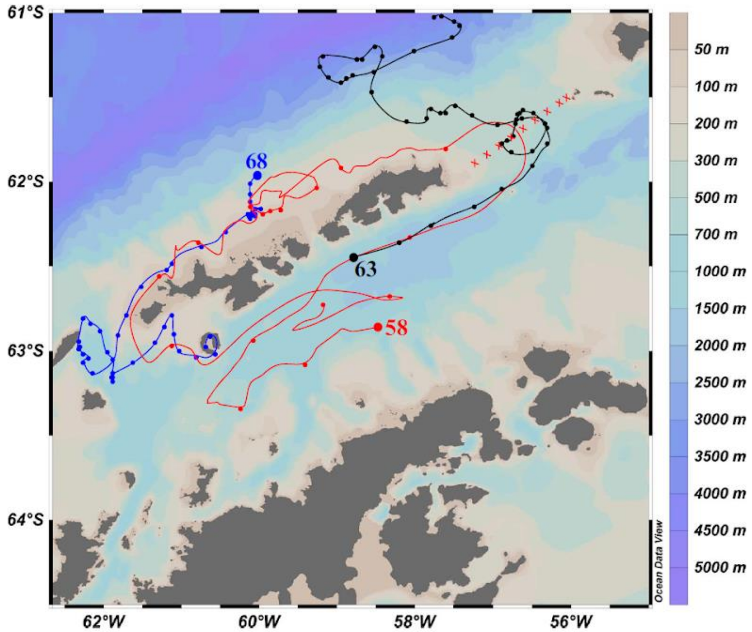

Figure 1.8. Drifter trajectories around the SSI. Dots are drawn every day for drifter 63 (black line) and drifter 68 (blue line) and every 10 days for drifter 58 (red line). Deployment locations are indicated by large dots. Red crosses locate CTD stations of transect TB. [From Sangrà *et al*. (2017) - Figure 3].

Prior to the publication of the studies presented in this thesis, the only observational-based vertical section depicting the circulation throughout the entire Bransfield Strait, as seen from direct velocity measurements was presented in Morozov (2007; Figure 1.9).

Typically, the BC has a width of about 20 km, with central jet velocities reaching 40-50 cm s^{-1} near the surface (Zhou *et al*., 2002, 2006), and decreasing linearly towards the bottom (Morozov, 2007; Savidge and Amft, 2009; Poulin *et al*., 2014). On the contrary, the CC appears to flow deeper in the water column intruding into the Bransfield Strait with maximum velocities around 5 cm s^{-1} (Morozov, 2007).

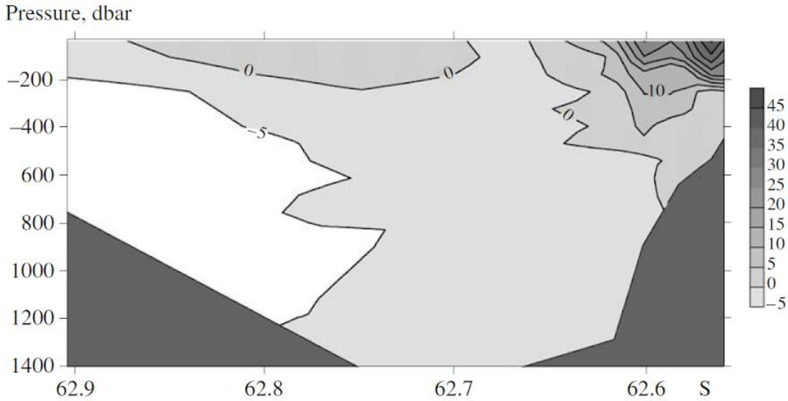

Figure 1.9. Current velocities measured by lowered Doppler profiler LADCP over the section across Bransfield Strait. Positive values correspond to the northeastern direction. A velocity grayscale is shown on the right. [From Morozov (2007) - Figure 3].

More recently, Frey *et al*. (2023) show the average velocity profile along the strait for the two main currents in the region, the BC and the CC, where the latter presents a nearly barotropic profile around 5 cm s^{-1} (Figure 1.10). The empirical orthogonal function modes presented in this analysis provide a representation of how the vertical profiles of the BC and CC velocities vary over depth. The differences between the two current systems are evident, with the BC showing a distinct baroclinic profile with a subsurface core at ~60 m depth while the CC is mostly barotropic, as previously noted.

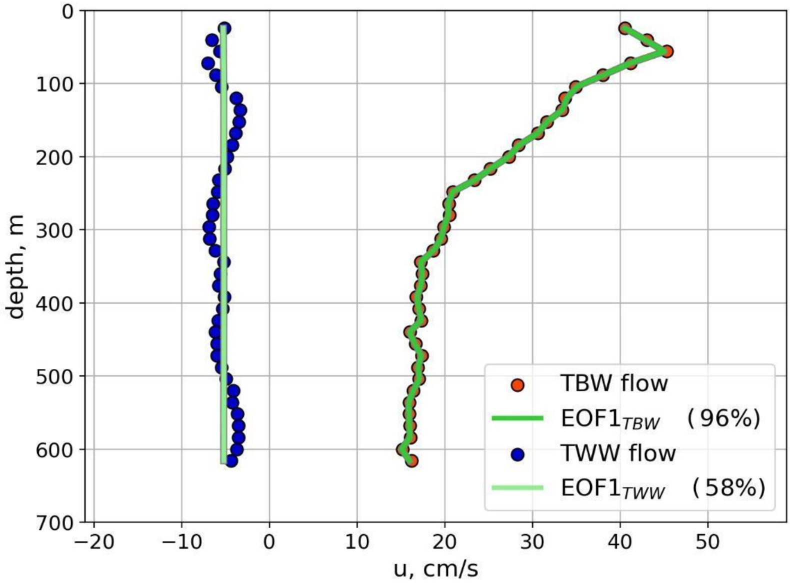

Figure 1.10. The averaged SADCP along-strait velocity profile in the BC (red dots) and CC (blue dots). Their first EOFs are shown by green and light green lines, respectively. The EOF first modes were scaled to match the mean speed profiles. The percentage of variability explained by the first empirical mode are shown in parentheses. [From Frey *et al*. (2023) - Figure 9].

Additionally, circulation maps based on surface drifter data depict the BC as a coherent northeastward-flowing jet with speeds of up to 40 cm s^{-1} (Zhou *et al*., 2002, 2006; Thompson *et al*., 2009). In contrast, the CC often appears as a more fragmented structure with discontinuities and counterflows near the Antarctic Peninsula (Figure 1.11). Importantly, the interaction between the BC and CC in the cross-strait direction remains not well defined. Lastly, we must note that observational-based studies prior to this thesis do not address the seasonal variations of the system.

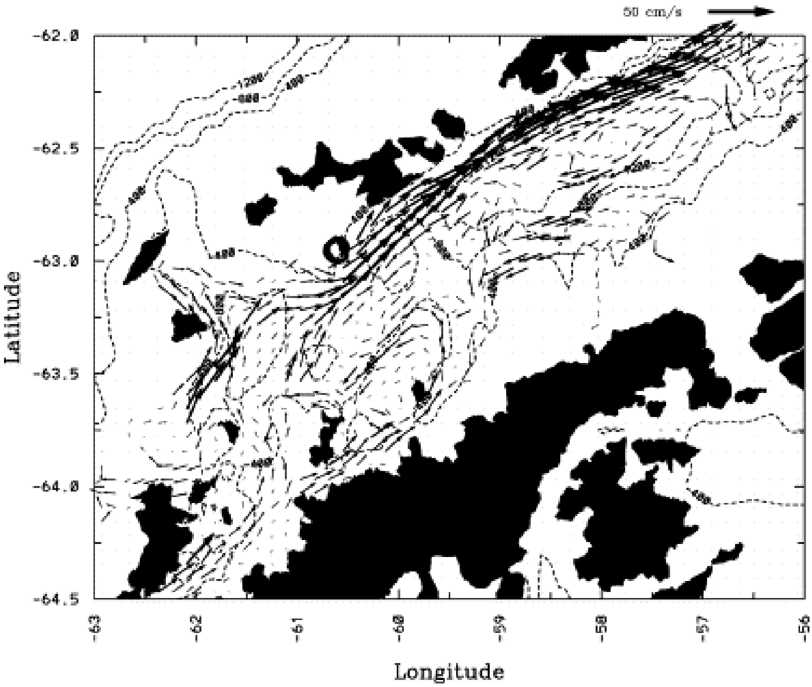

Figure 1.11. Ensemble mean surface velocity vectors in the Bransfield and Gerlache Straits in 7×7 km^2 bins. [From Zhou *et al.* (2002) - Figure 3].

Regarding the vertical structure of the BC, limited research has been reported following direct velocity measurements (Morozov, 2007; Savidge and Amft, 2009; Poulin *et al.*, 2014). The most comprehensive observational study to date, conducted by Savidge and Amft (2009), used extensive shipboard ADCP data collected from 1997 to 2003 aboard the *R/V Nathaniel B. Palmer* and *R/V Laurence M. Gould*. Their findings provided a thorough description of the BC's summer circulation, revealing that the jet deepens, and transport increases downstream of Livingston Island. Velocities reached up to 50 cm s^{-1}, with transport increasing from 1 Sv near Boyd Strait to 2 Sv east of Livingston Island (Figure 1.12a).

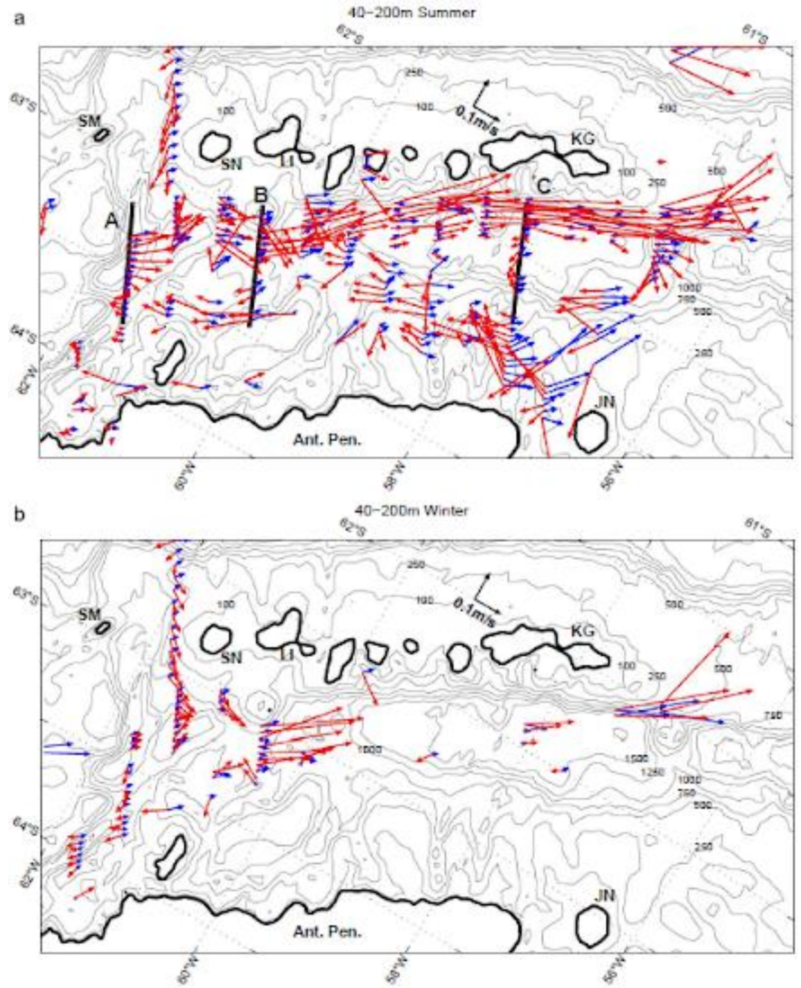

Figure 1.12. (Panel a) summer and (panel b) winter means (red) and standard errors (blue) from detided, binned shipboard ADCP velocities between 40 and 200 m depth. Note the blue arrows are all oriented to the northeast, as the standard errors in the north and east directions are expressed as positive values. Lines indicate locations of sections shown in Fig. 11. [From Savidge and Amft (2009) - Figure 10].

In winter, Savidge and Amft (2009) reported flow through Boyd Strait turning eastward into the Bransfield Strait to feed the BC (Figure 1.12b). However, downstream observations were insufficient to confirm the existence of a strong eastward jet along the southern shelf of the SSI during winter. Their binned velocity data primarily represented summer conditions, with no measurements collected during spring or autumn. Consequently, the BC's seasonal variability during these transitional periods has remained unexamined until recently. Wang *et al.* (2022) conducted a model-based study that includes summer and winter model output data (Figure 1.13); however, the absence of the spring and autumn views in their analyses keeps leaving critical gaps in understanding the BC's complete seasonal cycle. Studies on the CC are even more limited and entirely absent regarding the description of its seasonal variations based on observations.

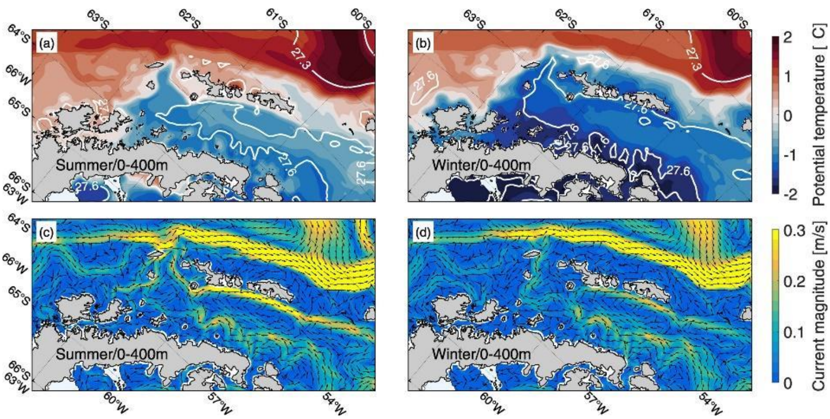

Figure 1.13. Summer (left panels) and winter (right panels) vertically-averaged (0–400 m) potential temperature and current from model simulations. (a), (b) Potential temperature (°C) and density (kg/m^3, white contours). (c), (d) Current direction (arrows) and magnitude (m/s, color), sub-sampled every six grid points. [From Wang *et al.* (2022) - Figure 5].

1.2.2 Biophysical coupling

Former studies highlight the BS as a patchy yet highly productive region, with chlorophyll-a (chl-a) concentrations often exceeding 3 mg m^{-3} during summer (Hewes *et al.*, 2009; Aracena *et al.*, 2018). This contrasts with the surrounding Southern Ocean, where chl-a concentrations generally range from 0.05 to 1.5 mg m^{-3} (Arrigo *et al.*, 1998; El-Sayed, 2005).

The elevated productivity in the inshore waters of BS is closely tied to the presence of TBW, which exhibits higher chl-a concentrations compared to TWW (Figure 1.14). Factors such as the depth of the upper mixed layer (UML), surface water stratification, and increased temperatures and iron availability have been linked to these enhanced chl-a levels (Hewes et al., 2009).

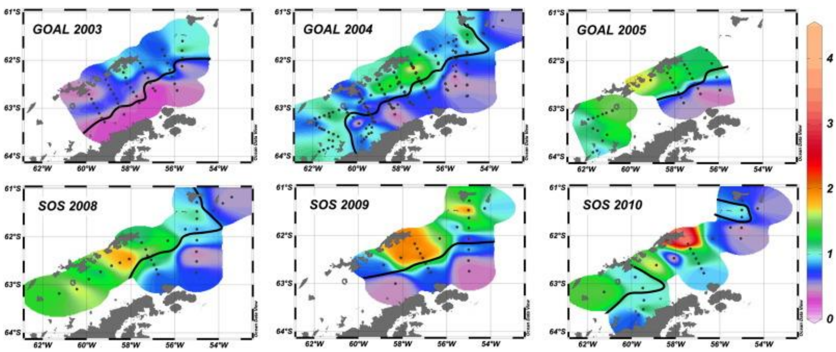

Figure 1.14. Surface Chl-*a* (mg m^{-3}) distribution during the six summer cruises conducted along the Bransfield Strait. Black dots indicate the position of sampling stations and the black lines represent the 0.9ºC isotherm, which separates the TWW (southeast) and TBW (northwestern). [From Gonçalves-Araujo *et al.* (2015) - Figure 2].

Some studies have advanced understanding of phytoplankton dynamics in the BS. García-Muñoz *et al.* (2013) reported that phytoplankton assemblages are linked to the Bransfield Current system, with nanophytoplankton dominating the stratified TBW and larger diatoms more prevalent near the AP (Figure 1.15). These findings underscore the potential for the PF to modulate phytoplankton community structure and biomass distribution seasonally.

However, chl-a variability in polar regions is not solely driven by water mass ocean characteristics. Sea ice dynamics and atmospheric forcing also play crucial roles in regulating primary production (Garibotti *et al.*, 2003; Smith *et al.*, 2008). Wind-driven variations in sea ice extent and concentration influence light availability and nutrient upwelling, further complicating the seasonal and interannual patterns of chl-a (Holland and Kwok, 2012; Kusahara *et al.*, 2019).

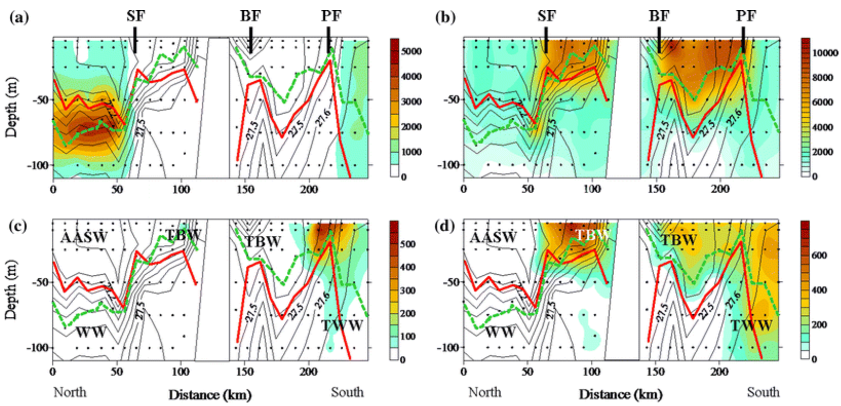

Figure 1.15. Vertical distribution of the abundance (Cells mL^{-1}) of nanoplankton groups detected with FCM along T.1. a 'Nano small', b 'Nano medium', c 'Cryptophytes', d 'Nano large'. Dots represent sampling depths. The locations of the fronts are indicated above in a and b. BF Bransfield Front, PF Peninsula Front, SF Shetland Front. The locations of water masses are indicated in c and d. AASW Antarctic Surface Water, TBW Transitional Bellingshausen Water, TWW Transitional Weddell Water, WW Winter Water. Isolines represent isopycnals. Red line is the MLD. Dashed line is the DFM. [From García-Muñoz *et al.* (2013) - Figure 4].

1.3 Thesis purposes and outline

As suggested in previous studies, monitoring the ocean dynamics within the Southern Ocean is important to assess variations and trends. Therefore, we analyse the northwest of the Antarctic Peninsula focusing on physical and biological features.

This thesis aims to assess quantitatively and qualitatively, for the first time, the spatiotemporal variability of the ocean circulation of the Bransfield Current and the Antarctic Coastal Current, as well as their implications on the distribution of chlorophyll-a, a key element in the marine ecosystem food web.

The working hypothesis is that the Bransfield Current remains present throughout most of the year, despite being described so far only during the Antarctic summer. Complementarily, it is hypothesized that the Antarctic Coastal Current also plays a recurring role in the oceanic dynamics of the Bransfield Strait, although its presence throughout the year and its seasonal variability have not yet been documented. Evaluating the seasonal variability of both boundary currents will provide critical physical oceanographic context for understanding biophysical coupling processes across the Bransfield Strait. This effort will deliver the scientific community a comprehensive series of hydrographic, dynamic, and biological climatologies for reference. These climatologies will not only enhance our understanding of the natural variability along the western margin of the Antarctic Peninsula—a key polar region in the context of global climate change—but will also provide seasonal average fields, enabling more statistically robust quantification of the significance of anomalous events and trends over larger time scales (e.g., interannual, decadal).

Complementarily, it is hypothesized that the spring-to-summer biophysical coupling, which controls the spatiotemporal variability of the phytoplankton assemblage across the Peninsula Front in the Bransfield Strait, could also be monitored through a combination of remotely sensed observations of chlorophyll-a concentrations, sea surface temperature, and sea ice concentration.

Following the above, this thesis is structured into five chapters. Chapter 1 serves as the introduction, providing the context and objectives of the study. Chapters 2, 3, and 4 focus on specific studies, each including a dedicated introduction, a description of the data and methods used, the results obtained, a discussion of these results, and the main conclusions.

Chapter 2 presents a climatology of the seasonal variations driven by the Bransfield Current (velocity and volume transport patterns) throughout all seasons using direct velocity observations. It is published in *Progress in Oceanography* (Veny *et al.*, 2022).

Chapter 3 analyses the monthly variability of the two boundary currents flowing through the Bransfield Strait —the Bransfield Current and the Antarctic Coastal Current— using satellite data. This chapter has been accepted for publication in *Frontiers in Marine Science* (Veny *et al.*, 2025).

Chapter 4 examines the seasonal biophysical coupling throughout the Bransfield Strait using observational and remotely sensed measurements. It is published in *Ocean Science* (Veny *et al.*, 2024).

Lastly, Chapter 5 presents the general conclusions, integrating the findings from the previous chapters and offering a broader perspective.

Chapter 2

Seasonal dynamics of the Bransfield Current

This chapter has been published as:

Veny, M., Aguiar-González, B., Marrero-Díaz, Á., & Rodríguez-Santana, Á. (2022). Seasonal circulation and volume transport of the Bransfield Current. *Progress in Oceanography*, *204*, 102795. https://doi.org/10.1016/j.pocean.2022.102795.

2.1 Introduction

The Bransfield Strait (BS) is a semi enclosed region located between the Antarctic Peninsula (AP) and the South Shetland Islands (SSI). Based on summertime data, previous studies have described the circulation in BS as consisting of western and eastern inflows circulating cyclonically (Grelowski *et al.*, 1986; Hofmann *et al.*, 1996; Zhou *et al.*, 2006; Sangrà *et al.*, 2017) with a street of mesoscale anticyclonic eddies (AEs) of Transitional Zonal Water with Bellingshausen influence (TBW) characteristics in between (Sangrà *et al.*, 2011, 2017). A sketch of this summertime circulation and major water masses is presented in Figure 2.1a. The schematics of the vertical structure of the Bransfield Current system are presented in Figure 2.1b.

The western inflow, namely the Bransfield Current (BC; Niller *et al.*, 1991; Zhou *et al.*, 2002, 2006), travels northeastward along the southern slope of the SSI as a coastal jet transporting TBW (θ > -0.4ºC and salinity <34.45 at 0-300 m depth). TBW is a well-stratified and relatively warm and fresh water, seasonally originated in the Bellingshausen Sea and Gerlache Strait due to summer heating and ice melting (Tokarczyk, 1987; García *et al.*, 1994; Sangrà *et al.*, 2011). At deeper levels (>300 m), a continuous tongue of cooled Circumpolar Deep Water (CDW) of about $-0.4<\theta<0.8$ºC and $34.4<S<34.5$ (Sangrà *et al.*, 2017) flows also hugging the southern SSI slope underlying the BC.

The eastern inflow in BS, the Antarctic Coastal Current (CC), travels southwestward transporting Transitional Zonal Water with Weddell Sea influence, TWW (θ < -0.4ºC and salinity >34.45), countering the northern Antarctic Peninsula coastline and spreading through the interior of the Strait. TWW is distinguished by colder and saltier waters than TBW, coming from the Weddell Sea (Tokarczyk, 1987; García *et al.*, 1994) and being rather homogeneous throughout the water column (Grelowski *et al.*, 1986; Hofmann *et al.*, 1996; García *et al.*, 2002c; Zhou *et al.*, 2002).

At surface and about 20-30 km from the peninsula slope, TBW encounters TWW forming the Peninsula Front, PF (García *et al.*, 1994; López *et al.*, 1999), a mesoscale shallow structure of 10 km wide, extending from the surface down to 100 m (Sangrà *et al.*, 2011). At depth, TWW widens its domain over the whole Strait and encounters TBW being transported by the BC near the southern SSI slope, where they form the subsurface Bransfield Front (BF) between 50 to 400 m (Niller *et al.*, 1991; García *et al.*, 1994; López *et al.*, 1999). Generally, the BF extends from 10 to 20 km, and is wider and shallower at the beginning of the BC pathway (Sangrà *et al.*, 2011).

Initially, both Niller *et al.* (1991) and Zhou *et al.* (2002, 2006) described the BC as a western boundary current driven in the interior of the strait by a negative wind stress curl and the ß-effect. However, following *in situ* hydrographic observations and laboratory experiments, Sangrà *et al.* (2011, 2017) and Poulin *et al.* (2014) showed that the BC propagates more consistently as a buoyant gravity current; the buoyant less-dense TBW flows along the SSI slope over the denser TWW, constrained in a narrow coastal band by the Coriolis force and by the buoyancy-induced pressure gradient. The width of the BC is typically 20 km, where central jet velocities reach 40-50 cm s^{-1} near the surface (Zhou *et al.*, 2002, 2006), decaying linearly towards the bottom (Morozov, 2007; Savidge and Amft, 2009, Poulin *et al.*, 2014).

Based on summertime hydrographic data, Sangrà *et al.* (2017) completed the description of the Bransfield Current System with the identification of TBW also north of the SSI, suggestive of the recirculation pathway of the BC around the SSI (Figure 2.1a), as also supported by surface drifter trajectories and laboratory experiments.

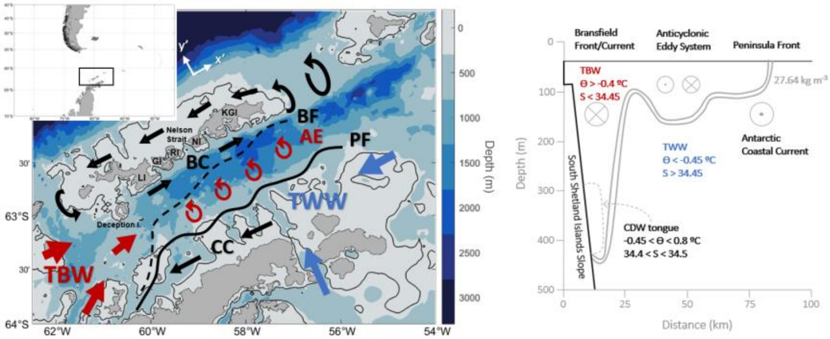

Figure 2.1. (a) Bathymetric map of the Bransfield Strait and summertime circulation pattern of the Bransfield Current System as described in Sangrà *et al*. (2011, 2017). Acronyms for SSI are LI (Livingston Island), GI (Greenwich Island), RI (Robert Island), NI (Nelson Island) and KGI (King George Island). The plotted axes indicate the rotation of the coordinate system in along-slope, x', and cross-slope, y', directions. The isobath of 200 m is highlighted with a black contour. Acronyms for major features follow: AE (Anticyclonic Eddy), BC (Bransfield Current), BF (Bransfield Front), CC (Antarctic Coastal Current), PF (Peninsula Front), TBW (Transitional Bellingshausen Water), TWW (Transitional Weddell Water). (b) Sketch of the main components of the Bransfield Current System along a vertical section crossing the Strait (modified from Figure 14 in Sangrà *et al*. (2011)) and the location of TBW (red) and TWW (blue). The Circumpolar Deep Water (CDW, black) tongue is distinguished by its temperature which is relatively higher than the surrounding waters. The spatial scales and ocean property ranges of each feature are indicated.

Given the above scenario, accounting for a proper description of the seasonal variability, modulating the circulation in BS is relevant for achieving a better understanding of the warm/cold water pathways defining the oceanic forcing to glacier retreat in this basin (Cook *et al*., 2016). However, only a handful of summertime studies investigate the full path of the BC flowing along the SSI slope.

Based on geostrophic estimates (0-500 db), the summertime volume transport of the BC has been reported to range between 0.38 Sv to 0.88 Sv along the southern SSI slope (Sangrà *et al*., 2011, 2017). After arrival to the northeastern tip of King George Island, and recirculation around the archipelago, the southwestward volume transport driven by the BC along the northern shelf of the SSI decreases to 0.10-0.19 Sv (Sangrà *et al.*, 2017).

Notably, few works have presented and analysed the BC vertical structure based on direct velocity measurements (Morozov, 2007; Savidge and Amft, 2009; Poulin *et al*. 2014). Up to date, the most comprehensive description of the circulation and transport in the Bransfield Strait was developed based on an extensive dataset of direct velocity measurements routinely collected along ship tracks performed by R/V *Nathaniel B. Palmer* and R/V *Laurence M. Gould* between 1997 and 2003 (Savidge and Amft, 2009). This study provided the first description of the summer velocity field and transport along the full pathway of the BC south of the SSI, finding that the jet deepens, and transport increases downstream south of Livingston Island. Velocities in the jet were reported to reach 50 cm s^{-1}, exceeding 35 cm s^{-1} in the averaged layer between 40-200 m depth. The increase in volume transport was estimated as 1 Sv in the vicinity of Boyd Strait to 2 Sv east of Livingston Island (Savidge and Amft, 2009). With regards to winter, these authors report a flow through Boyd Strait turning eastward into the Bransfield Strait and feeding directly into the BC (Savidge and Amft, 2009); however, downstream of Deception Island their data collection lack measurements to confirm the BC also drives a strong eastward jet along the southern shelf of the SSI (see Figure 10 in Savidge and Amft, 2009). Thus, the record long means from the binned shipboard ADCP velocities between 40 and 200 m depth (their Figure 6) is constructed from, most of the BC extent, on summertime data. This prevents the confirmation of a strong eastward jet present in all seasons, especially when spring and autumn fields are omitted in their summer-winter view of the circulation.

In this work we use the same dataset of direct velocity measurements as in Savidge and Amft (2009), but here extended to a total of 375 cruises performed between 1999 and 2014. This data extension (about ten more years of observations) allows us to update the view presented in Savidge and Amft (2009), providing the first description of the velocity field and volume transport driven by the BC through all seasons and over nearly its entire pathway of circulation south of the SSI. The paper is organized as follows. In Section 2.2, we describe data and methods. In Section 2.3, we present the results. First, we focus on the seasonal and spatial variability of the horizontal and vertical structure of the BC velocity field (Sections 2.3.1 and 2.3.2, respectively). Second, we estimate the seasonal volume transport driven by the BC along the southern slope of the SSI (Section 2.3.3). Last, we perform a mass balance analysis to elucidate the origin of the year-round increase in volume transport occurring east off Nelson Strait (Section 2.3.4). In Section 2.4, we discuss the observed variability of the BC against the literature. Section 2.5 closes the paper with a summary of the main conclusions.

2.2 Data and methods

We use an updated version of the data collection analysed in Savidge and Amft (2009), which extends the initial period 1997-2003 towards 2014. The data collection originates from two extensive datasets of direct velocity measurements collected with 150 kHz 'narrow band' Shipboard Acoustic Doppler Current Profilers (SADCPs) along ship tracks from R/V *Nathaniel B. Palmer* and R/V *Laurence M. Gould*, which navigated routinely from South America to Antarctica for logistical operations during all the seasons. Data acquisition and initial processing were accomplished by Dr. Eric Firing (University of Hawaii) and Dr. Teresa Chereskin (Scripps Institution of Oceanography). Velocity profiles were acquired and processed with UHDAS (University of Hawaii Data Acquisition System) and CODAS (Common Ocean Data Access System), respectively. The processed 5 min averaged transect data we use in this work can be found at the Joint

Archive for Shipboard ADCP (JASADCP) webpage, http://ilikai.soest.hawaii.edu/sadcp/index.html. For additional processing details the reader is referred to Lenn *et al*. (2007) and Firing *et al*. (2012).

Initially, in the updated data collection we analyse, R/V *Nathaniel B. Palmer* contributes with 820,146 profiles from 100 cruises, performed between 1999 and 2013; and, R/V *Laurence M. Gould* contributes with 130,280 profiles from 275 cruises, performed between 1999 and 2014. Profiles collected from R/V *Nathaniel B. Palmer* have a vertical resolution of 8 m from 31-503 m depth, while profiles collected from R/V *Laurence M. Gould* have a vertical resolution of 10 m from 30-1040 m depth. We address vertical interpolation on standard depth levels through both datasets towards a common 10 m vertical resolution starting at 30 m depth. Additionally, all individual data points outside a two-standard-deviation threshold were removed (Fischer and Visbeck, 1993) and replaced by linear interpolation.

Before gridding the data, as will be detailed in the following section, the barotropic tidal signal was removed using the Circum-Antarctic Tidal Simulation (CATS2008), an update to the model described by Padman *et al*. (2002). The derived model predictions for each measurement, at a given location and time, were taken as the best estimate of tidal magnitude and phase to remove from the data. Using a previous version of this same model, Savidge and Amft (2009) reported that predicted tidal velocities of mixed nature (diurnal and semidiurnal tides) were present at the shelf-edge and near the SSI in the Bransfield Strait. Thus, the four major tidal constituents (diurnal and semidiurnal) were accounted for the removal of the tidal signal in this work. However, we observe that the resulting fields turn out to be rather insensitive to the removal of the tidal signal (as it occurred in Savidge and Amft (2009)), given that mean and seasonal circulation features appear similarly using either detided or undetided data.

Finally, we must note that the nature of the present observations, obtained in an opportunistic manner (ship tracks from logistic operations), introduce some data limitations in the form of irregular samplings in space and time. Hence, in the following subsections, we address the gridding procedure, data density analyses, and error analyses such that we account for the impact of these data limitations when discussing later our results.

2.2.1 Climatology of the seasonal circulation

The procedure followed to construct the climatology we used to analyse the variability of the seasonal velocity field is described in this section. Seasons are defined following Zhang *et al.* (2011) and Dotto *et al.* (2021), as: summer (January-February-March), autumn (April-May-June), winter (July-August-September) and spring (October-November-December).

To account for the irregular nature of the data distribution, which is not uniform in space, we need to select the largest possible size still capturing mesoscale structures so we can retain the highest velocity profile population per each grid cell. To this aim, we select as cell size the Rossby radius of deformation, which is on the order of 10 km (Chelton *et al.*, 1998). The resulting grid domain is shown in Figure 2.2.

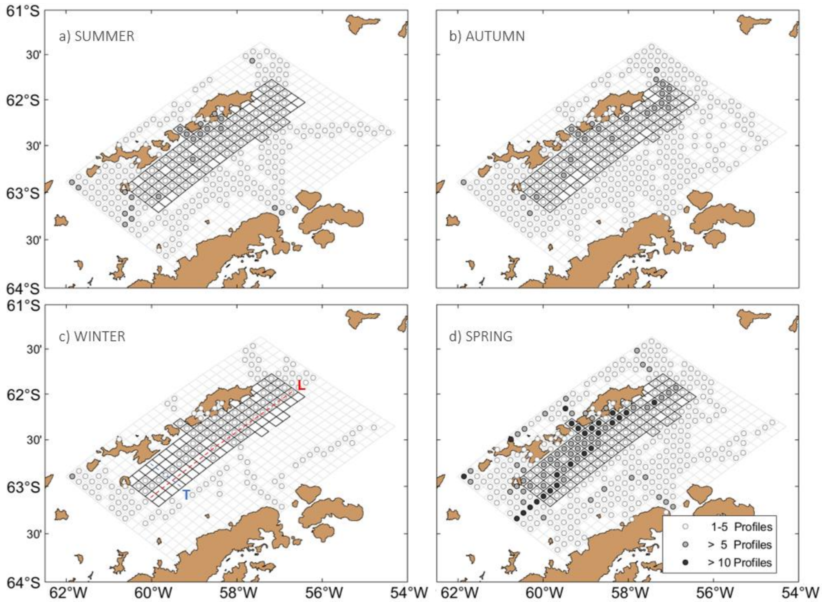

Figure 2.2. Maps of seasonal data density showing the amount of climatological seasonal velocity profiles per year obtained for each grid cell of 10x10 km in the area of study, from 1999 to 2014 (see legend). Panels follow seasons as: a) summer, b) autumn, c) winter, and d) spring. The grid cells highlighted in black indicate the domain used to construct along-slope (L) and cross-slope (T) transects (see panel c) for the study of the variability of the BC.

Because the data distribution is also irregular in time, we apply the step-by-step time-averaging scheme in Figure 2.3 where for every grid cell, and at all depth levels, velocity profiles are averaged at increasing timescales. Then, velocity profiles are first averaged when sampling the same month and year. Second, the resulting monthly velocity profiles are averaged when sampling the same season and year. Finally, the seasonal profiles of every year are averaged per grid cell into climatological seasonal profiles. Thus, the number within each grid cell in Figure 2.2 indicates how many seasonal profiles exists at a given location (i. e., a number of 5 indicates that there are 5 velocity profiles of a given season from 5 different years).

Through the time-averaging scheme, and given that some months and years are undersampled, we take a key assumption: ocean dynamics occurring through a given season evolve similarly through every month of that given season for any year. This assumption attempts to account for the fact that certain months and years are absent at some locations. We make the reader aware of this through the data density maps in Figure 2.2 not to observe our end results as the product of equally weighted averages at all locations (a situation otherwise unachievable when counting with an irregular sampling).

Importantly, through the time-averaging scheme, we apply a vertical minimum coverage criterium of 90% of data availability between 30 to 250 m depth (the vertical range of study, as explained in the following section). We do this to prevent the rise of artificial staircases, which could appear as an artifact of averaging profiles with different vertical ranges of depth.

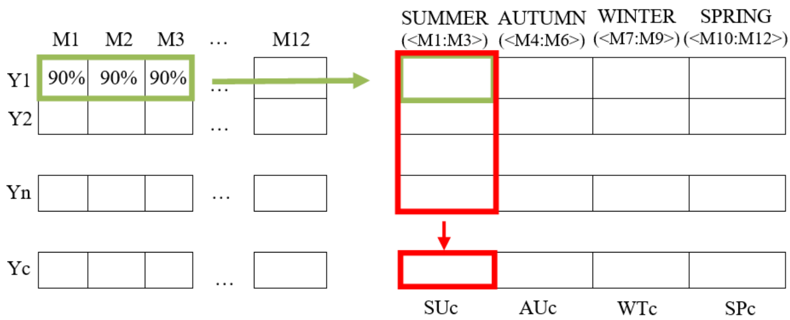

Figure 2.3. Time-averaging scheme for the generation of the climatological velocity profiles falling within each grid spatial cell showed in Figure 2.2. The time-averaging codes are defined as follows: M#, is the monthly averaged velocity of the month #; Y#, is the yearly averaged velocity of the year #; SUc, AUc, WTc and SPc, are the seasonal climatological averages. The computation of the climatological velocity profiles per grid cell includes only those profiles of which have measurements in, at least, a 90% of the first 250 m of the profile to prevent artificial stepwise structures.

Based on these data density distributions, we select as the focus of our study the cells highlighted in black in Figure 2.2, which capture the pathway of the BC at its best spatial coverage possible. Then, we use the seasonal velocity profiles over this domain to construct maps of the horizontal velocity field. To this aim, we apply the 2D interpolation tool developed by D'Errico (2022). Based on sparse linear algebra and PDE discretizations, this tool attains consistency with the original data field.

Error estimates are computed considering the instrument error of the SADCP measurements, which is 0.5 cm s^{-1} (Instruments, 2013), plus the Standard Error of the Mean (SEM, as computed in Savidge and Amft (2009)) accounting for all the profiles falling within a given grid cell and time-step of the averaging procedure in Figure 2.3. In the few cases where the SEM cannot be computed due to the solely existence of one velocity profile falling within a given grid cell and time-step, the associated errors account only for the instrument error.

2.2.2 Along/cross-slope rotation and volume transport

In order to assess properly the structure of the Bransfield Current according to its propagation parallel to the southern slope of SSI, we rotate counterclockwise the cartesian coordinate system along-slope (x') and cross-slope (y'). The rotation angle is 36.25º, which responds to the mean angle of all the cross-slope grid cells highlighted in black in Figure 2.2. In each cell grid, the east and north components of seasonal velocity profiles are rotated, obtaining along-slope (u') and cross-slope (v') seasonal velocity components.

The along-slope (U'; Equation 2.1) and cross-slope (V'; Equation 2.2) seasonal volume transport estimates are computed following:

$$U'^{(x',t)} = \int_0^{D_T} \int_h^{h_0} u' \, dzdy' \quad (2.1)$$

$$V'(y',t) = \int_0^{D_L} \int_h^{h_0} v' \, dzdx' \quad (2.2)$$

where x' is the along-slope coordinate; y' is the cross-slope coordinate; u' (m s^{-1}) and v' (m s^{-1}) are along-slope and cross-slope seasonal velocity components, respectively; D_T (m) and D_L (m) are the lengths of the cross-slope and along-slope transects, denoted as T_i (i=1, 21) and L_j (j=1,4) transects, respectively; h_0 (m) is the depth of the shallowest available velocity; and, h (m) is the depth of the deepest available velocity.

In all cases, h_0 and h are 30 m and 250 m, respectively. The value of h_0=250 m for the computation of volume transport estimates follows reasonably from previous works where the Bransfield Current was shown to propagate as a coastal flow with a layer thickness about 200-300 m (Morozov, 2007; Savidge and Amft, 2009; Sangrà *et al.*, 2011, 2017).

The cross-slope transects generally depart from the slope south off the SSI and span towards the middle of Bransfield Strait all along the SSI. Thus, D_T is generally 30 km, except when the grid cell most coastward/oceanward is absent; then, D_T becomes 10 km shorter. Upon data availability, the along-slope transects we use in this study are constrained to the domain spanning from Nelson Strait to midst of King George Island (T10-T14) and, thus, D_L is 40 km in all cases.

Prior to calculation of volume transport estimates following Equations (2.1) and (2.2), we apply a similar interpolation work to that accounted for in the previous section for the construction of the horizontal maps of the velocity field. Thus, we use the 2D interpolation tool developed by D'Errico (2022) through all T and L transects over data gaps equal/shorter than 20 km between grid cells. By data gap, we mean here either the absence of a vertical profile within a given grid cell or the presence of a vertical profile which is shorter than spanning from 30 to 250 m depth. Through this interpolation procedure, we achieve transects which have a common vertical spatial coverage. This enables a robust comparison among volume transport estimates, avoiding under/over estimations when data gaps existed prior to interpolation. Exceptions occur on a few cases where one of the four grid cells at the T transects is missing and still an associated volume transport estimate is provided. These cases will be noted in the text through our discussion of the results to prevent the reader about straightforward comparisons.

Anywhere in the text where a ± quantity is indicated next to volume transport estimates, that amount refers to the propagated error from sum of the instrument error and the SEM associated to each seasonal velocity profile composing the transect.

2.3 Results

Through this section we characterize the horizontal and vertical structure of the Bransfield Current using climatological fields constructed from direct velocity measurements (Section 2.3.1 and Section 2.3.2, respectively). We also estimate the volume transport driven by the upper 250 m of the Bransfield Current, varying seasonally and spatially along its pathway south of the South Shetland Islands (Section 2.3.3). Finally, in Section 2.3.4, we perform a mass balance analysis east off the Nelson Strait to elucidate the origin of the observed volume transport increase of the BC.

2.3.1 Seasonal variability of the Bransfield Current: horizontal structure

The seasonal climatology of the horizontal circulation driven by the BC is presented in Figures 2.4 and 2.5 following depth-averaged velocities within the 80-100 m and 130-150 m layers, respectively (velocity vectors smaller than associated errors are not shown). These two depth ranges are selected to account for the decrease in strength of the BC at depth, as previously found in summertime and springtime observations (Morozov, 2007; Savidge and Amft, 2009; Sangrà *et al.*, 2011, 2017).

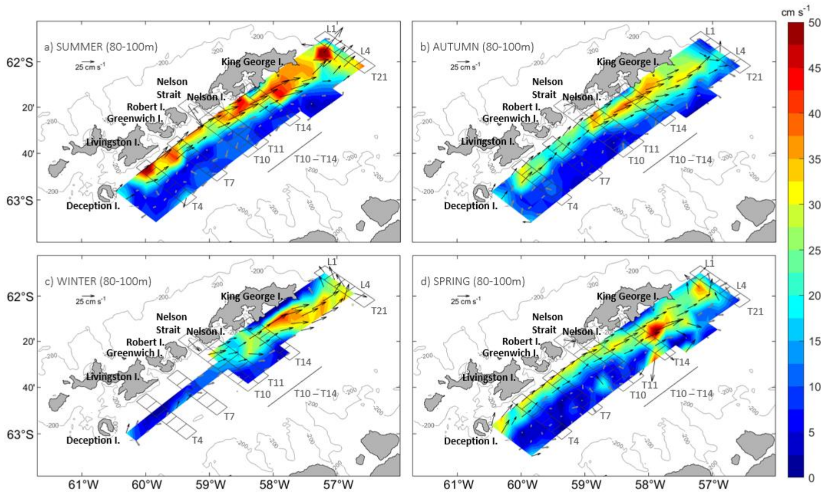

Figure 2.4. Seasonal maps of the horizontal velocity field at 80-100 m following: a) summer, b) autumn, c) winter, and d) spring. Shades of colours are speed in units of cm s^{-1}. Scaled arrows represent direction and strength (only arrows with speed values above their associated error are shown and used for interpolation). Scaled arrows in black (gray) indicate magnitudes equal/above (below) 15 cm s^{-1}. Cross-slope (T_i) and along-slope (L_j) transects of study are also indicated in each panel. The T10-T14 line shows the area limited by these transects.

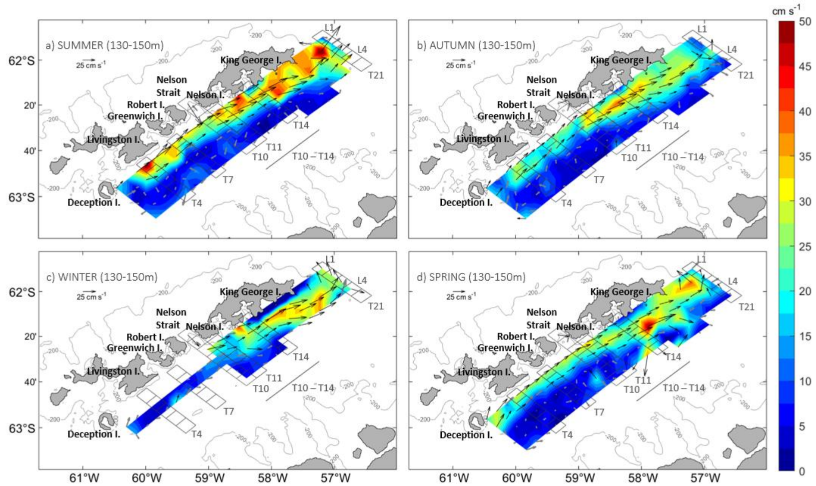

Figure 2.5. Same as in Figure 2.4 but for the depth range of 130-150 m.

The most outstanding feature is the recurrence of a northeastward-flowing coastal jet circulating parallel to the southern slope of the South Shetland Islands, from Livingston Island to King George Island along a path of 170 km in all seasons but in winter, when the current is also visible but over a shorter domain of available measurements spanning from Nelson Island to King George Island, a path of 90 km. Noting the similarity of this current to that one described in previous works for this region during summertime (e.g., Niller *et al.*, 1991; Zhou *et al.*, 2002, 2006; Sangrà *et al.*, 2011, 2017; Poulin *et al.*, 2014), we attribute the signal of this year-round coastal jet to the Bransfield Current.

Spatially, the BC appears as a well-organized, and relatively strong, coastal current flowing towards the northeast downstream of Livingston Island (T3-T4). Upstream of this location, near Deception Island (T1-T2), the flow appears through all seasons, but spring, less intense and not yet organized as a northeastward-flowing current. This spatial pattern agrees well with previous works based on summertime observations (Figure 2.1a), here extending its recurrence through other seasons. When approaching the northeasternmost tip of King George Island, the recirculation of the BC around the archipelago is suggested to occur also year-round, although more clearly during winter and spring (Figures 2.4 and 2.5). This recirculation had been previously demonstrated to occur at least during summertime (Sangrà *et al.*, 2017), thus extending here its recurrence also through winter and spring.

Seasonally, results support that the BC flows at higher velocities during summer, reaching climatological values up to 60 cm s^{-1} and 50 cm s^{-1} at depths between 80-100 m and 130-150 m, respectively. The weakening of the BC at depth, as will be shown further in the following section for all seasons, is consistent with prior works based on direct velocity measurements: the springtime vertical transect presented in Morozov (2007); the summertime climatological vertical transects presented in Savidge and Amft (2009); and, the summertime velocity profiles presented in Poulin *et al.* (2014). During autumn, winter, and spring the BC also flows as a relatively strong and continuous jet, peaking at about 40 cm s^{-1}.

Lastly, we note that a weaker flow exists seaward of the Bransfield Current in the peninsula cross-strait direction. This field near the middle of the Strait, highly variable and not aligned to any prevailing direction, is consistent with the street of inter-frontal anticyclonic eddies reported in Sangrà *et al.* (2011, 2017).

2.3.2 Seasonal variability of the Bransfield Current: vertical structure

Through this section, we characterize the seasonal and spatial variability of the Bransfield Current in the upper 250 m of the water column based on vertical transects sourced with multiyear sampled grid cells. Noting that the horizontal velocity distributions in Figures 2.4 and 2.5 show the circulation of the BC flows parallel to the southern slope of SSI, we investigate in the following the vertical structure of the BC after rotating its velocity components into u' and v', where these represent the along-slope and cross-slope components, respectively (see section 2.2.2).

To characterize the along-slope structure of the BC we selected the cross-slope transects which were most repeatedly sampled over time, i. e. transects T4, T7, T10, T11, T14 and T21. A detailed summary of the multiyear seasonal data behind these transects is shown in Figure 2.6. The distribution of available measurements covering different locations and seasons by years supports the coherence of the resulting climatological velocity fields presented in Figure 2.7. In this latter figure, vertical sections of the T transects show only the along-slope component, u', given that this captures the stream direction. The cross-slope component, v', through the T transects (not shown) is generally negligible, as supported by the circulation patterns shown in Figures 2.4 and 2.5.

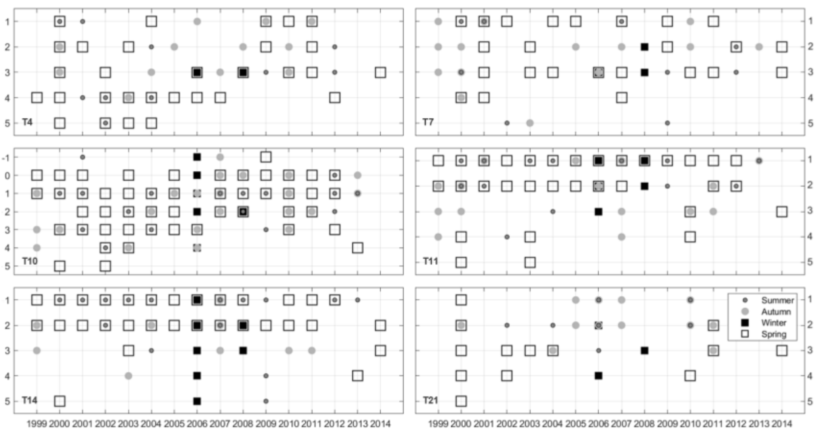

Figure 2.6. Summary of the multiyear seasonal data used to construct the climatology shown in Figure 2.7 for the along-slope transects T4, T7, T10, T11, T14 and T21 (see their location in Figures 2.4 and 2.5). The values on the vertical axis are the values of the transects L. L-1 and L0 in T10 are those located in the Nelson Strait. A mark for a given grid cell over a specific year indicates that at least one profile exists for that season, so its size or shape is not proportional nor related to its value.

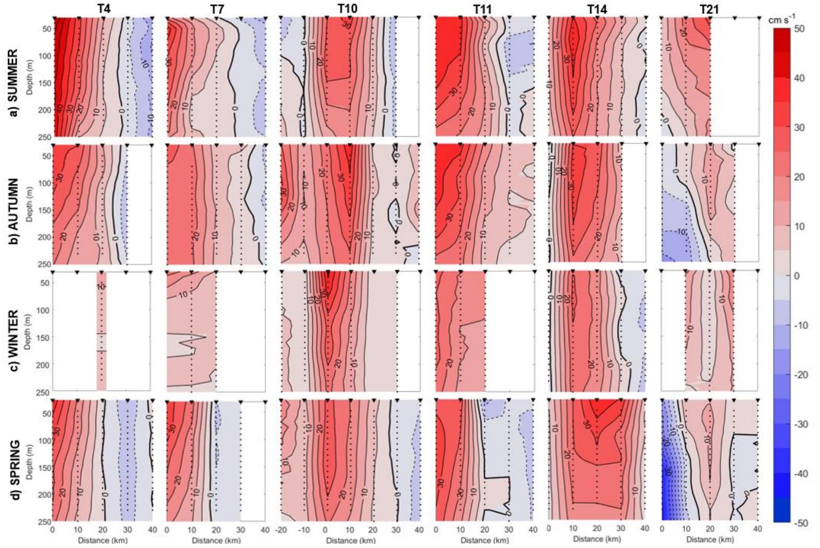

Figure 2.7. Seasonal climatology of along-slope velocities measured by SADCPs in the upper 250 m of the water column at transects T4, T7, T10, T11, T14 and T21 (from left to right-hand side panels). Seasons follow (from top to bottom panels): a) summer, b) autumn, c) winter and d) spring. Distance starts at the southern SSI slope being perpendicular to the islands' slope (distance 0 km), except at transect T10, which departs from Nelson Strait at -20 km. Velocity is positive (negative) towards the northeast (southwest) in the along-slope direction (see rotated coordinates x' and y' in Figure 2.1a). The black dots along the vertical refer to original data points.

A major finding is the confirmation of the BC as a strong and recurrent jet flowing northeastward along the slope of the SSI through all seasons ($u' > 0$ in red, Figure 2.7) down to at least 250 m depth. In all vertical sections, the structure of the BC agrees well with the view of a surface-intensified coastal jet whose velocities decrease at depth, particularly from 100-150 m towards deeper levels (Figure 2.7). This structure also agrees with the horizontal circulation pattern shown at different depths in Figures 2.4 and 2.5.

Importantly, across all transects but transect T21, data density allows us to capture counterflows ($u' < 0$ in blue, Figure 2.7) flowing towards the southwest, and likely attributable to the highly variable currents driven by the street of eddies sketched in Figure 2.1, and visible in the horizontal velocity fields presented in Figures 2.4 and 2.5. At T21, the vertical structure of the BC suggests the start of its recirculation around King George Island (Figure 2.7), as also supported by Figures 2.4 and 2.5.

Seasonally, the strengthening of the BC, as presented in the previous section, is also visible through its vertical structure (Figure 2.7), flowing at higher maximum velocities during summertime at nearly all the transects (velocities up to 45 cm s^{-1}). The only exception occurs south of Nelson Island (transect T10), where the BC flows at 25 cm s^{-1} in summer and spring as opposed to higher velocities up to 35 cm s^{-1} in autumn and winter. The BC flows at an average speed of 25-35 cm s^{-1} during the other seasons across all the transects, except in transect T21, where velocities are generally lower (~10-20 cm s^{-1}).

Spatially, we find the BC displays a coherent pattern depending on whether it finds to its left-hand side the islands' slope or a channel between islands (Figure 2.7). This is visible by comparison of transects T4, T7 and T11, which show the BC south off the slope of Livingston Island, Greenwich Island and Nelson Island, respectively, against transects T10 and T14, which show the BC flowing south off channels between SSI. Along the former case (T4, T7 and T11), the BC appears hugging the islands' slope; along the latter case (T10 and T14), the BC appears flowing as a seaward wedge-shaped current.

Combining the horizontal structure of the BC (Figures 2.4 and 2.5) along with its vertical structure (Figure 2.7), one can observe how the northeastward-flowing jet (the BC) broadens from about 20-30 km wide upstream of Nelson Strait (T3-T9) towards about 40 km wide downstream of Nelson Strait (T11-T20). Upon data availability, we find this spatial pattern seems to be present year-round.

2.3.3 Seasonal variability of the Bransfield Current: along-shore volume transport

In this section we analyse the spatial and seasonal variability of the volume transport driven by the Bransfield Current along its full pathway south of the SSI. At this point, we recall that volume transport estimates follow from the 4 vertical profiles of horizontal velocity closer to the coast (where the BC and the highest data density are found), as described in Section 2.2.2 (Equations 2.1 and 2.2).

Accordingly, Figure 2.8 presents the seasonal estimates of the along-slope volume transport, U' (Sv), driven by the Bransfield Current through each transect of the study area. These transects are perpendicular to the island coastlines and to the stream direction of the Bransfield Current (see the grid cells accounting for each transect in Figure 2.2). Importantly, we must note that only positive U' values (northeastward volume transport) have been taken into account when computing the volume transport driven by the Bransfield Current. This condition applies not to underestimate the transport of the BC when opposing flows are also acting across the transect. The errors obtained for each estimate of volume transport are indicated in Figure 2.8. We find these errors vary from 0.02 to 0.62 Sv with an average value of 0.17 Sv.

Following the distinctive widths the BC exhibits upstream and downstream of Nelson Strait (see section 2.3.2), we analyse our estimates of volume transport according to these two zones. Upstream of Nelson Strait (T3-T9), we find the BC transports on average 0.93 ± 0.15 Sv in summer, 0.88 ± 0.19 Sv in autumn and 0.65 ± 0.13 Sv in spring. During wintertime, there is scarcity of data and transports from T7 to T9 account for an average of 0.50 ± 0.04 Sv. Downstream of Nelson Strait (T11-T20), we find the BC transports on average 1.53 ± 0.17 Sv in summer, 1.29 ± 0.26 Sv in autumn, 1.20 ± 0.15 Sv in winter and 1.22 ± 0.20 Sv in spring. These results suggest that upstream of Nelson Strait the BC transports the largest volumes of water through summer and autumn as compared to spring and winter, though accounting for the associated errors only winter stands out with a significatively weaker transport. Downstream of Nelson Strait, estimates of volume transport are generally higher than upstream and present no significative difference among seasons when accounting for their associated errors.

	Summer, U' (Sv)	Autumn, U' (Sv)	Winter, U' (Sv)	Spring, U' (Sv)	Mean, U' (Sv)
T1	0.57 ± 0.19	0.86 ± 0.21	0.24 ± 0.02*	0.77 ± 0.14	0.61 ± 0.14
T2	0.42 ± 0.03	0.43 ± 0.07	0.21 ± 0.02*	0.71 ± 0.34	0.44 ± 0.12
T3	0.90 ± 0.11	1.17 ± 0.13	-	0.54 ± 0.16	0.87 ± 0.13
T4	1.14 ± 0.28	0.93 ± 0.16	-	0.66 ± 0.10	0.91 ± 0.18
T5	0.70 ± 0.13	0.89 ± 0.21	-	0.54 ± 0.07	0.71 ± 0.14
T6	1.22 ± 0.21	0.63 ± 0.16*	-	0.82 ± 0.26	0.89 ± 0.21
T7	0.64 ± 0.11	0.98 ± 0.31	0.22 ± 0.03*	0.63 ± 0.11	0.62 ± 0.14
T8	0.85 ± 0.15	0.83 ± 0.19	0.42 ± 0.07*	0.71 ± 0.13	0.70 ± 0.13
T9	1.05 ± 0.09	0.72 ± 0.16	0.86 ± 0.03	0.65 ± 0.06	0.82 ± 0.09
T10	0.82 ± 0.25	1.34 ± 0.28	0.93 ± 0.12	1.12 ± 0.23	1.05 ± 0.22
T11	1.32 ± 0.18	1.36 ± 0.26	0.83 ± 0.13*	0.86 ± 0.13	1.09 ± 0.17
T12	1.41 ± 0.21	1.43 ± 0.24	1.02 ± 0.06	1.39 ± 0.13	1.31 ± 0.16
T13	1.71 ± 0.13	1.56 ± 0.22	1.69 ± 0.06	1.22 ± 0.47	1.55 ± 0.22
T14	1.31 ± 0.12	1.28 ± 0.15	0.92 ± 0.18	1.45 ± 0.12	1.24 ± 0.14
T15	1.40 ± 0.08	1.16 ± 0.30	0.99 ± 0.11*	-	1.18 ± 0.16
T16	1.47 ± 0.03	1.34 ± 0.36	1.60 ± 0.39	1.17 ± 0.16	1.40 ± 0.24
T17	1.42 ± 0.10	1.35 ± 0.48	1.38 ± 0.24*	1.37 ± 0.15	1.38 ± 0.24
T18	1.85 ± 0.06	1.50 ± 0.22	1.23 ± 0.08*	1.09 ± 0.23	1.42 ± 0.15
T19	-	-	-	-	-
T20	1.90 ± 0.62	0.62 ± 0.15	1.14 ± 0.14	-	1.22 ± 0.30
T21	0.59 ± 0.27*	0.26 ± 0.03	-	0.22 ± 0.05	0.36 ± 0.12

Figure 2.8. Estimates of the northeastward along-slope volume transport (U' (Sv) > 0), and their associated error (Sv) for transects T1 to T21 based on SADCP measurements (the transects of study are shown in Figures 2.4 and 2.5). The volume transport was computed from 30 m to 250 m depth, departing south of the SSI slope to 30 km offshore (L4). The error for each estimate is also indicated. The size of the coloured bars indicates the transport normalized against the largest value obtained for each season: summer (red), autumn (yellow), winter (blue) and spring (green). Estimates with an asterisk indicate transports computed across transects where D_T equals to 20 km instead of 30 km. See Section 2.2.2 and Equations (2.1) and (2.2) for further details.

In the following section we explore further the origin of the observed downstream increase in volume transport, which we attribute to the inflow of source waters feeding the BC through Nelson Strait, i. e. from the northern domain of the SSI to its southern domain.

From the transect T20 to T21, the BC volume transport decreases notably towards its nearly lowest values on record, suggestive of the current approaching its turning point for the recirculation around the SSI (the average transport estimate decreases from 1.22 ± 0.30 Sv to 0.36 ± 0.12 Sv).

2.3.4 Volume transport increase east of Nelson Strait

Through this section we perform a mass balance analysis following the box defined along-slope by the transects T10 and T14 and cross-slope by the transects L1 to L4 (see the location of the transects in Figures 2.4 and 2.5). The aim is to elucidate whether the observed downstream increase in volume transport of the BC may be driven by an inflow through the Nelson Strait, i. e. in the direction through the transects L1 to L4. This inflow has been previously suggested to feed the BC with source waters coming from the northern shelf of the SSI based on hydrographic measurements (Gordo Rojas, 2013).

The mass balance analysis is presented in Figure 2.9, where seasonal net transport estimates are indicated for each boundary of the box of study. Note that outgoing (incoming) transports are denoted as positive (negative) transports in red (blue) colours. For a better visualization of the transport signs, a scheme is added for the autumn study case.

In the following, we describe the results for summer as illustrative of the general pattern occurring through all seasons. Thus, in summer, we find the following inflows: an entry of 0.82 ± 0.25 Sv that flows through T10, driven by the BC, and an entry of 0.60 ± 0.18 Sv that flows through L1, driven by the currents through the Nelson Strait. Then, a small part of the latter contribution appears to recirculate towards the northeast (from L1 to L2-L4), while most of it joins the BC, exiting the box through the transect T14. As a result, we find an outflow of 1.31 ± 0.12 Sv exits the box, which accounting for the associated errors appear to be in approximate balance with the inflows. This structure is consistent with the horizontal velocity circulations observed in Figures 2.4 and 2.5.

It is worthwhile noting that, generally, estimates for V' are lower than for U' since the former represents the cross-stream direction of the BC. However, seasonal estimates of V' confirm the recurrence over time of a southward current flowing through transects L1, L2 and L3, especially during summer and winter, when the flux coming from the Nelson Strait appears to be feeding the BC more prominently. When the flow reaches L4, the transport to the south appears lower as the influence of the Nelson Strait inflow diminishes.

		BOX		
		U' (Sv) T10	V' (Sv) L	U' (Sv) T14
Summer	L1	-0.82 ± 0.25	-0.60 ± 0.18	1.31 ± 0.12
	L2		-0.48 ± 0.17	
	L3		-0.08 ± 0.15	
	L4		-0.03 ± 0.08	
Autumn	L1	-1.34 ± 0.28	-0.37 ± 0.13	1.28 ± 0.15
	L2		-0.59 ± 0.22	
	L3		-0.35 ± 0.20	
	L4		0.07 ± 0.14	
Winter	L1	-0.93 ± 0.12	-0.60 ± 0.11	0.92 ± 0.18
	L2		-0.32 ± 0.14	
	L3		-0.51 ± 0.07	
	L4		-0.17 ± 0.05	
Spring	L1	-1.12 ± 0.23	-0.39 ± 0.17	1.45 ± 0.12
	L2		-0.38 ± 0.15	
	L3		-0.06 ± 0.24	
	L4		0.25 ± 0.29	

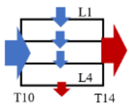

Figure 2.9. Mass balance analysis showing the estimates of along-slope volume transports, U' (Sv), through the transects T10 and T14 (D_L = 40 km), and cross-slope volume transports, V' (Sv) through the transects L1 to L4. A positive (negative) value indicates outgoing (incoming) transports in red (blue) as shown in the scheme for the autumn study case. The error for each estimate is also indicated.

2.4 Discussion

In this section, we focus on discussing the seasonal circulation and volume transport of the Bransfield Current as observed in our climatology, noting that uncovering the year-round driving forces of the current are beyond the scope of the present work.

2.4.1 Horizontal structure

Along its pathway south off the SSI, the Bransfield Current appears to follow the bathymetry orientation, as constrained to the coast by the Coriolis force through all the seasons (Figures 2.4 and 2.5). When approaching the easternmost tip of King George Island, our climatologies suggest the BC starts its recirculation around the archipelago, as reported in previous works based on summertime observations (Sangrà *et al.*, 2011, 2017). The start of the recirculation is mostly evident in Figures 2.4 and 2.5 during winter and spring, thus our results suggest its recurrence also through other seasons. In this line, several studies have hypothesized that the transport of TBW around the SSI contributes to the fertilization of the waters along the northern shelf (Teira *et al.*, 2012, García-Muñoz *et al.*, 2014), which highlights the importance of further understanding the circulation around the islands. Furthermore, as a relatively warm water, the routes followed by TBW are key in a context of ocean forcing to glacier retreat around the SSI (Kacper *et al.*, 2021), thus demanding a more comprehensive knowledge of the year-round hydrography contouring the SSI bathymetry.

With regards to the speed magnitude, summertime averaged values of about 40 cm s^{-1} shown here for the velocity fields at 80-100 m and 130-150 m (Figures 2.4 and 2.5, respectively) agree well the speed range of surface drifters deployed within the BC during the same season, and reporting average speeds also about 30-40 cm s^{-1} (Zhou *et* *al.*, 2002; Sangrà *et al.*, 2017). Although for a slightly different depth range of averages, these summertime jet velocities are also in good agreement with those reported across lines B and C in Savidge and Amft (2009), reaching 35 cm s^{-1} in the averaged layer between 40-200 m depth (line B, located south off Livingston; and, line C, located King George Islands). Available wintertime measurements in Figures 2.4 and 2.5 not only confirm the BC flows at relatively strong speeds about 25 cm s^{-1} downstream of Nelson Island, but also that peak speeds can be found about 40 cm s^{-1} south off King George Island.

2.4.2 Vertical structure

The along-slope velocity field of the BC shows a coherent structure where the current flows persistently northeastward constrained to the islands' slope through all seasons (Figure 2.7). However, we find some spatial variability regarding its dynamical core when comparing the structure displayed at cross-slope sections departing from the island's slope and when departing from the channel between islands (see the locations of cross-slope transects in Figure 2.4). Thus, when south of the SSI, the core of the BC forms half of a wedge shape leaning on the island slope (transects T4, T7 and T11) while, between channels, a full wedge shape is visible due to the local detachment of the current from the island slope (transects T10, T14 and T21).

Seasonally, the vertical sections confirm that highest velocities through nearly its full pathway are found during summertime with near-surface core velocities up to 45-50 cm s^{-1} (Figure 2.7). However, during the other seasons, the BC also flows as a relatively strong and continuous jet with core velocities up to 30-35 cm s^{-1} (Figure 2.7).

Generally, the spatial variability of the BC displays two distinct regions: upstream and downstream of Nelson Strait

(Figures 2.4, 2.5 and 2.7). Through the first region (transects T3-T9), the BC exhibits from spring to autumn a horizontal width between 20-30 km. Downstream of Nelson Strait (transects T11-T20), the BC widens in all seasons another 10 km offshore, likely promoted by the widening of the King George Island shelf (see the isobath of 200 m in Figures 2.4 and 2.5), which forces the current to lean over the slope further offshore.

Interestingly, the above pattern along the islands' southern shelf, distinguishing between a narrower region and a wider region, upstream and downstream of Nelson Strait, respectively, is also in agreement with previous studies describing the dynamical properties of density-driven coastal currents. Münchow and Garvine (1993) investigated this type of currents when analysing the Delaware Coastal Current. In this study case, the outflow of buoyant waters from the Delaware Estuary drives lateral density gradients sustaining an alongshore current which remains trapped near the coast by the Coriolis force. The authors also described two dynamically distinct regions, which they termed as the source and plume regions. Through the source region, they find a current whose width scales well with the internal deformation radius. Farther downstream, in the plume region, the authors find much reduced lateral density gradients and a current much wider than the deformation radius. This is also the case for the BC when accounting for the internal deformation radius. An analogous pattern is also observed in laboratory experiments when reproducing the scales of the BC in a rotating tank (Sangrà *et al.*, 2017). The authors show that the lab-simulated BC also widens downstream, before starting its recirculation around a wall mimicking the SSI archipelago (see Figure 11 in Sangrà *et al.* (2017)). Notably, the downstream widening of the jet in these two latter works appears without invoking the widening of the shelf. This suggests that both the internal dynamics of the density-driven coastal current and the shelf widening of King George Island may add to the downstream widening of the BC.

2.4.3 Volume transport

The volume transports (30-250 m) presented in Figure 2.8 reveal several major features regarding spatial and temporal variability of the BC along its pathway and through seasons.

Upstream of the Nelson Strait, we find the BC presents similar volume transports in summer, autumn and springtime (0.93 $\pm$ 0.15 Sv, 0.88 $\pm$ 0.19 Sv and 0.65 $\pm$ 0.13 Sv, respectively). However, the transport appears to decrease notably during winter, as compared to other seasons, at least south off Greenwich Island to Nelson Strait (0.50 $\pm$ 0.04 Sv in transects T7-T9). We hypothesize that this seasonal variation may be driven by the different nature of the inflow feeding the BC during winter, when source waters of the BC might be potentially fed from sea-ice formation areas in the Bellingshausen Sea and Gerlache Strait. This different source waters would approach the water mass properties of TBW to those of the cooler and saltier TWW. The latter phenomenon would then account for a relaxation of the buoyancy-induced pressure gradient that has been shown to sustain the BC at least during summer in previous works (Sangrà *et al.*, 2011, 2017).

Downstream of Nelson Strait, the seasonally-averaged estimates of volume transport suggest that no significant variability exists among seasons, presenting on the main significantly higher transports than estimates obtained farther upstream. This increase in volume transport occurring after passing the Nelson Strait is consistent with prior summertime data presented in Savidge and Amft (2009) and Sangrà *et al.* (2011), based on direct velocity measurements and geostrophic velocity estimates, respectively. The novelty is that our observations show this spatial pattern is also present through autumn, winter and spring based on direct velocity measurements. We hypothesize the downstream increase in volume transport may be driven by a recurrent inflow passing through Nelson Strait (Figures 2.4 and 2.5) and feeding the BC with source waters coming from the northern slope of the SSI. The existence of this inflow feeding BC has been previously suggested by at least one previous work (Gordo Rojas, 2013). Accordingly, we test this hypothesis further computing the mass balance analysis presented in Figure 2.9 and performed south of Nelson Strait. Results suggest that the BC, flowing along the northern shelf of the SSI, may find Nelson Strait as a gateway for recirculation, thus supplying recurrently with source waters the BC flowing along the southern shelf of the SSI. We find this phenomenon is particularly noticeable during summer and winter, when the flux coming from the Nelson Strait appears to be feeding the BC more prominently (Figure 2.9).

The decrease of the northeastward volume transport occurring east of King George Island, near transect T21, is attributed here to the start of the recirculation of the BC around the archipelago. We observe this pattern from spring to autumn, which agrees well with summertime geostrophic volume transport estimates presented in Sangrà *et al.* (2011), thus supporting the likely recurrence of this spatial feature through all seasons.

The year-round nature of the BC, as uncovered in this work, is especially relevant in that it shows the BC flows permanently at relatively the same strength, at least downstream of Nelson Strait, over a pathway of about 100 km. This opens a challenging question about the driving forces behind this recurrence through all seasons. The question here is whether the density gradient set by the water mass contrast between TBW and TWW also exists as a major driving force from autumn to spring. In this regard we highlight that future observational efforts must focus on assessing the seasonal hydrography of the BC with year-round mesoscale-solving measurements so that the year-round driving forces of the current might be better elucidated.

In Table 2.1 we summarize the present knowledge about velocity and volume transport estimates reported in the literature about the Bransfield Current. As previously introduced, most of these studies are based on summertime measurements and so the year-round description through seasons is presently lacking. These velocity values and volume transports are derived either from direct velocity measurements or from hydrographic data (geostrophic velocities), then generally relative to 500 db. For each case in Table 2.1, we detail the origin of the values being provided.

Overall, volume transport estimates from previous works fall on the main within the same order of magnitude as results presented in this study, noting that existing discrepancies may be caused due to a comparison where different methodologies apply, and where synoptic measurements are compared against climatological values. To the best of our knowledge, this work delivers an unprecedented view of the spatiotemporal variability of the Bransfield Current transport along its full pathway south off the South Shetland Islands. Existing data gaps, especially in the upstream region of the current near Livingston Island during winter, and the data limitations that an irregular sampling implies, suggest that future observational and modeling efforts would benefit a further understanding of the ocean dynamics in this region, thus assisting the study of the forcing mechanism behind the BC.

Reference	Velocity (cm s^{-1}) or Transport (Sv)	Instrument	Methodology for vel. or transp. estimate	Region	Date (month/year)
Grelowski *et al.*, 1986	0.96 Sv 1.09 Sv 0.74 Sv	CTD	Geostrophic vel. relative to 500 db	South off Livingston I. South off Robert I. South off King George I.	12/1983 – 01/1984 (Spring – Summer)
Niller *et al.*, 1991	0.3 Sv / 0.8 cm s^{-1}	CTD	Geostrophic vel. relative to 200 db	Western Deception I.	11/1986 – 03/1987 (Spring – Summer)
López *et al.*, 1999	1 Sv	CTD	Geostrophic vel. relative to 500 db	South off King George I.	01 – 02/1994 (Summer)
Gomis *et al.*, 2002	0.5 Sv	CTD	Geostrophic vel. relative to 500 db	South off Livingston I.	12/1995 – 01/1996 (Spring – Summer)
Zhou *et al.*, 2002	40 cm s^{-1}	Drifters at 15 and 40 m	Direct vel. observations	Along the southern SSI slope	11/1988 – 01/1990 (All seasons)
Zhou *et al.*, 2006	40 – 50 cm s^{-1}	ADCP	Direct vel. observations	South off King George I.	03/2004 (Summer)
Morozov, 2007	0.8 Sv	LADCP	Direct vel. observations	South off Greenwich I.	11/2005(Spring)
Savidge and Amft, 2009	30 cm s^{-1} 40 cm s^{-1}	SADCP	Geostrophic vel. relative to 500 db	South off Livingston I. South off King George I.	1997 – 2003 (Summer)
Sangrà *et al.*, 2011	0.50 Sv 0.73 Sv 0.88 Sv	CTD	Geostrophic vel. relative to 500 db	South off Livingston I. South off Robert I. South off King George I.	12/1999 (Spring) + 12/2002 – 01/2003 (Spring – Summer)
Poulin et al., 2014	30 – 40 cm s^{-1}	ADCP	Direct vel. observations	South off the Nelson Strait	01/2010 (Summer)
Sangrà *et al.*, 2017	0.31 – 0.49 Sv	CTD	Geostrophic vel. relative to 500 db	South off the Nelson Strait	01/2010 (Summer)
This study	0.93 Sv 0.88 Sv 0.50 Sv 0.65 Sv 1.53 Sv 1.29 Sv 1.20 Sv 1.22 Sv	SADCP	Direct vel. observations	Upstream of Nelson Strait (south off Livingston I. – Robert I.) Downstream of Nelson Strait (south off Nelson I. – King George I.)	1999 – 2014 (Clim. summer Clim. autumn Clim. winter Clim. spring Clim. summer Clim. autumn Clim. winter Clim. spring)

Table 2.1. Summary of velocity observations and volume transport estimates of the Bransfield Current. The acronyms are: ADCP, Acoustic Doppler Current Profiler; CTD, Conductivity, Temperature and Depth; LADCP, Lowered Acoustic Doppler Current Profiler; SADCP: Shipboard Acoustic Doppler Current Profiler.

2.5 Conclusions

The Bransfield Current has been traditionally described as a summertime coastal jet flowing northeastward and hugging the South Shetland Islands slope while contouring the bathymetry of the archipelago and constrained by the Coriolis force (Niller *et al.*, 1991; Zhou *et al.*, 2002, 2006; García *et al.*, 1994; Sangrà *et al.,* 2011, 2017). Based on *in situ* hydrographic observations and laboratory experiments, previous authors have shown that the summertime circulation of the Bransfield Current agrees well with that of a buoyancy-driven coastal current (Sangrà *et al.,* 2011, 2017; Poulin *et al.,* 2014). The buoyancy-induced pressure gradient occurs between the relatively warmer and fresher TBW, leaning over the islands' slope, and the colder and saltier TWW, originated in the Weddell Sea and flooding into Bransfield Strait.

In this work we present an updated view of the seasonal circulation and volume transport driven by the Bransfield Current, following the pioneering work by in Savidge and Amft (2009), where a summer-winter view follows from direct velocity measurements (SADCP data) collected between 1997-2003. To do this, we use a longer period of direct velocity observations (1999-2014), which also improve the spatial coverage in time. This novel approach and data extension allow us to characterize the velocity field and volume transport driven by the BC through all seasons and over nearly its entire pathway of circulation south of the SSI in an unprecedented manner.

This study confirms the BC is a year-round feature of the circulation in Bransfield Strait, flowing persistently towards the northeast along the southern slope of the SSI, a path of 170 km. We also find the recirculation around the archipelago, as described in previous summertime studies (Sangrà *et al.,* 2011, 2017), is likely to occur also through other seasons, at least during winter and spring. These features are observed in the horizontal and vertical distributions of the velocity field in Figures 2.4, 2.5 and 2.7.

Through the water column, the structure of the BC agrees well with the summertime and springtime views reported in previous works (Morozov, 2007; Savidge and Amft, 2009; Poulin *et al.*, 2014), and describes the BC as a surface-intensified coastal jet whose velocities decrease at depth, particularly from 100-150 m towards deeper levels (Figure 2.7). Also, we find the BC displays a coherent pattern depending on whether it finds to its left-hand side the islands' slope or a channel between islands (Figure 2.7). Along the former case, the core of the BC leans on the island slope, while in the latter case, the core flows as a wedge-shaped current, missing an immediate boundary to its left-hand side.

Generally, the spatial variability of the BC displays two distinct regions: upstream and downstream of Nelson Strait. Upstream of Nelson Strait, the BC flows with an approximate core width of 20-30 km, which is slightly larger than the internal Rossby deformation radius for this region, R_d = 10 km (Grelowski *et al.*, 1986; Chelton *et al.*, 1998). This occurs from Livingston Island to Robert Island (transects T3-T9; Figures 2.4 and 2.5), at least from spring to autumn. Winter data scarcity prevents us from an analogous statement during this season. Downstream of Nelson Strait, and towards King George Island (T11-T20), we find the BC widens through all seasons up to a width of about 40 km, much wider than the deformation radius (Figures 2.4, 2.5 and 2.7). This widening is consistent with laboratory experiments reproducing the dynamics of the BC as a density-driven coastal current, hugging the simulated islands (a wall) to its left-hand side in a rotating tank (Sangrà *et al.*, 2017). We argue that in the real ocean, the widening of the King George Island shelf might promote further the widening of the BC since, flowing from the surface down to at least 300 m depth, the jet will have to accommodate its width to contour the island slope further offshore.

The above description, in terms of the observed seasonal and spatial variability, suggests that Nelson Strait marks the transition between two different regions: upstream (T3-T9) and downstream (T11-T20) of Nelson Strait. Upstream of the Nelson Strait, the BC presents similar volume transports in summer, autumn and springtime (0.94 ± 0.15 Sv, 0.88 ± 0.19 Sv and 0.65 ± 0.13 Sv, respectively). During winter, the transport appears to decrease notably, as compared to other seasons, at least south off Greenwich Island (0.50 ± 0.04 Sv in transects T7-T9). Downstream of Nelson Strait, the seasonally-averaged estimates of volume transport suggest that no significant variability exists among seasons: 1.53 ± 0.17 Sv in summer, 1.29 ± 0.26 Sv in autumn, 1.20 ± 0.15 Sv in winter and 1.22 ± 0.20 Sv in spring.

The observed increase in volume transport after passing the Nelson Strait is consistent with prior summertime data presented in Savidge and Amft (2009) and Sangrà *et al.* (2011), based on direct velocity measurements and geostrophic velocity estimates, respectively. Our observations show this spatial pattern is also present through autumn, winter and spring based on direct velocity measurements. According to this finding, we also performed a mass balance analysis which suggests the downstream increase of the BC volume transport is likely due to a recurrent inflow of source waters coming seasonally from the northern slope of the SSI and passing through the Nelson Strait (Figure 2.9).

Overall, results from this work highlight that future modeling and observational efforts must be addressed to cover existing gaps about the dynamics of the BC, especially in the upstream region of the current near Livingston Island during winter. In this line, the seasonal hydrography of the Bransfield Current must also be investigated further based on mesoscale-solving measurements close to the islands' coastlines, especially when noting that the Bransfield Current has been shown in the past to propagate as a summertime buoyancy-driven coastal jet transporting relatively warm and fresh Transitional Zonal Water with Bellingshausen influence (Sangrà *et al.*, 2011, 2017), whose presence in Bransfield Strait might be limited during seasons different from summer.

We conclude this work delivers an unprecedented view of the spatiotemporal variability of the Bransfield Current seasonal circulation and volume transport along its full pathway south off the South Shetland Islands, where our results agree well with independent estimates and descriptions from previous works (Table 2.1).

Chapter 3

Interbasin exchange between the Bellingshausen and Weddell seas

This chapter has been accepted for publication in *Frontiers in Marine Science*:

Veny, M., Aguiar-González, B., Ruiz-Urbaneja, A., Pereira-Vázquez, T., Puyal-Astals, L., & Marrero-Díaz, Á., & (2025). Boundary currents in the Bransfield Strait: near-surface interbasin water volume and heat exchange. *Frontiers in Marine Science*, *12*, 1555552. https://doi.org/10.3389/fmars.2025.1555552

3.1 Introduction

The west Antarctic Peninsula (wAP) is particularly sensitive to climate change due to the profound implications that varying warm/cold water pathways have for glacier dynamics and sea ice cover in this region (Cook *et al.*, 2016). In this setting, the Bransfield Strait (BS), located between the Antarctic Peninsula (AP) and the South Shetland Islands (SSI), acts as a gateway and a key region for water masses exchange between the Bellingshausen and Weddell seas; two sea basins which differ markedly in their thermohaline properties. In addition, the BS can be divided into three distinct basins: the western, central, and eastern basins (WB, CB, and EB, respectively, in Figure 3.1; Gordon and Nowlin, 1978; López *et al.*, 1999), which are separated by sills with depths of 630 m (WB-CB) and 1000 m (CB-EB).

At surface, the BS is characterized by the convergence of two distinct water masses: the relatively warm, less saline waters of the Bellingshausen Sea typically found within the first 300 m (Transitional Bellingshausen Water, TBW: $\theta > -0.4$ºC, salinity < 34.35, and density $\sigma_\theta < 27.64$ kg m^{-3}; Sangrà *et al.*, 2017) and the colder, more saline waters of the Weddell Sea distributed throughout the water column (Transitional Weddell Water, TWW: $\theta < -0.4$ºC, salinity > 34.35, and density $\sigma_\theta > 27.64$ kg m^{-3}; Sangrà *et al.*, 2017). These water masses are transported, respectively, by the following primary currents: the Bransfield Current (BC), which flows northeastward as a baroclinic narrow jet along the SSI, and recirculates counterclockwise to the north of the islands (Sangrà *et al.*, 2017), and the Antarctic Coastal Current (CC), a wide, slow-moving current that extends to deeper waters and flows southwestward along the AP slope (Figure 3.1). Following this scenario, the BS serves as a natural laboratory for studying the complex interactions between oceanic boundary currents transporting relatively warm and cold water masses.

The BC and CC jointly form a cyclonic-like circulation within the strait, with a street of mesoscale anticyclonic eddies of TBW characteristics in between (Sangrà *et al.*, 2011, 2017), where the Peninsula Front (PF) serves as a seasonal hydrographic boundary. The PF is formed by a sharp gradient between TBW and TWW and responds to the variability of boundary currents and the water mass exchange they drive. During the austral summer, the PF is well defined due to the heightened contrast between the warmer and fresher TBW and the colder and saltier TWW (García *et al.*, 1994; López *et al.*, 1999; Sangrà *et al.*, 2017), while in winter, the front dissipates as the thermal gradient weakens due to the cooling and deepening of surface waters, which homogenizes the water column (Veny *et al.*, 2024). The variations of the PF location and strength are thus essential for understanding the horizontal and vertical distribution of water masses (García-Muñoz *et al.*, 2013; Sangrà *et al.*, 2017; Gordey *et al.*, 2024).

Year-to-year variability in the BC and CC further influences oceanic forcing on glacier and sea-ice dynamics in the BS and farther south (Cook *et al.*, 2016; Vorrath *et al.*, 2020, 2023), with changes in sea-ice extent and duration having cascading effects on local climate, ocean circulation, and ecosystem productivity (Schofield *et al.*, 2010; Ducklow *et al.*, 2013; Eayrs *et al.*, 2019).

Lastly, the PF and boundary currents in the BS also play a critical role in shaping phytoplankton niches and, consequently, the entire marine food web and governing biogeochemical processes (Loeb *et al.*, 1997; Montes-Hugo *et al.*, 2009; García-Muñoz *et al.*, 2013; Veny *et al.*, 2024). During the austral summer, surface chlorophyll-a concentrations are elevated near the SSI, while near the AP the phytoplankton blooms seem to develop less abruptly and at deeper levels (Veny *et al.*, 2024). This biophysical interaction between ocean circulation, fronts and primary productivity sustains local and remote Antarctic marine ecosystems (Loeb *et al.*, 1997, 2009; Atkinson *et al.*, 2004; Johnston *et al.*, 2022; Annasawmy *et al.*, 2023), including Antarctic krill (*Euphausia superba*), a key species in this ecosystem (Murzina *et al.*, 2023).

Building on previous studies, we aim to provide new insights into the seasonal interplay between boundary currents, atmospheric forcing, oceanic forcing, and sea ice dynamics governing the circulation in the BS. We expect our results will serve as a baseline for future research on long-term trends in the wAP ocean circulation and sea ice dynamics. Additionally, they will help to understand how Antarctic marine ecosystems respond to climate variability, given that local boundary currents and hydrography shape the phytoplankton bloom phenology and structure (Veny *et al.*, 2024).

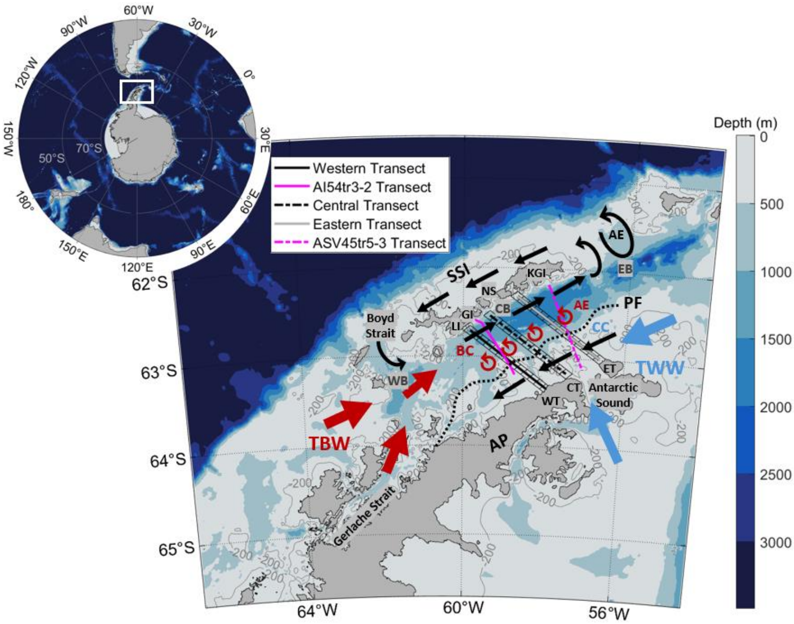

Figure 3.1. Sketch of the circulation in the Bransfield Strait with indication to key geographical locations and oceanographic features. Acronyms for the South Shetland Islands (SSI) include LI (Livingston Island), GI (Greenwich Island), and KGI (King George Island). Acronyms for the western, central, and eastern basins (WB, CB, and EB, respectively) as well as for Nelson Strait (NS) and Antarctic Peninsula (AP) are also shown. Acronyms for major oceanographic features are as follows: AE

(anticyclonic eddy), BC (Bransfield Current), CC (Antarctic Coastal Current), PF (Peninsula Front), TBW (Transitional Bellingshausen Water) and TWW (Transitional Weddell Water). Additionally, five transects are shown (see the legend for line styles and colour coding). Three of these—Western Transect (WT), Central Transect (CT), and Eastern Transect (ET)—are defined according to Veny *et al.* (2022) and are used in this study to capture spatiotemporal variability of atmospheric and oceanic properties. The other two are cruise transects from Frey *et al.* (2023): one conducted on 24 November 2017 from the Antarctic Peninsula to Livingston Island by the R/V *Akademik Ioffe* (AI), labeled as code 54tr3_2, and another on 18–19 December 2017 from the Antarctic Sound to King George Island by the R/V *Akademik Sergey Vavilov* (ASV), labeled as code 45tr5_3.

The manuscript is organized as follows. In Section 3.2, we describe the data and methods used in our study. In Section 3.3, we present and discuss the results. First, in Section 3.3.1, we analyse the surface geostrophic velocities of the boundary currents: BC and CC. Second, in Section 3.3.2, we examine their oceanic and atmospheric forces, including Sea Surface Temperature (SST), air temperature, and Sea Ice Coverage (SIC). In addition, in Section 3.3.3, we evaluate the wind stress and its correlation with the surface geostrophic velocities to assess this atmospheric forcing on the boundary currents. In Section 3.3.4, we characterize the monthly climatology of near-surface volume and heat transport of the boundary currents and their balances using altimeter-derived surface geostrophic seawater velocity, temperatures from Dotto *et al.* (2021), and remotely sensed SST. Section 3.4 concludes with a summary of main findings. Finally, in Appendix A, we discuss the limitations of surface drifter data and two open-access global ocean reanalysis products, and emphasize the need for improved models and high-resolution data integration.

3.2 Data and methods

This section outlines the data sources and methodologies. The satellite datasets described below cover the period from

1993 to 2022 (30 years), providing a comprehensive foundation for evaluating the boundary currents in the BS. The climatological Shipboard Acoustic Doppler Current Profiler (SADCP) data from Veny *et al.* (2022) cover the years 1999 to 2014. We also use synoptic data collected in 2017, firstly analysed, and made available, by Frey *et al.* (2023). The seasonal climatological temperature fields, derived from Conductivity, Temperature and Depth (CTD), Marine Mammals Exploring the Oceans Pole to Pole (MEOP), and Argo float measurements as described by Dotto *et al.* (2021), cover the period from 1990 to 2019. The *in situ* drifter data and reanalysis products, addressed in the Appendix A, span the periods 1979 to the present and 1994–2015, respectively.

3.2.1 Satellite data: altimeter-derived surface currents, SST, SIC, air temperature, wind stress

We use altimeter-derived surface geostrophic eastward and northward sea water velocity processed by the Data Unification Altimeter Combination System (DUACS) multimission altimeter data processing system. For detailed spatial and temporal analyses, the dataset employed corresponds to a processing Level 4 (L4), encompassing a global ocean coverage with a spatial resolution of $0.25^{\circ}\times0.25^{\circ}$. The data availability spans from January 1993 to September 2023 (https://doi.org/10.48670/moi-00148). To analyse the structure of the boundary currents as they flow parallel to the main axis of the BS, aligned with the southern slope of the SSI and the western slope of the AP, the cartesian coordinate system is rotated counterclockwise. We refer, hereafter, to the rotated reference system as: along the strait (x') and across the strait (y'). This rotation angle, 36.25º, corresponds to the average orientation of the across-strait grid cells shown in Veny *et al.* (2022). In each transect, the eastward and northward altimeter-derived surface velocity components are transformed to derive the along-strait (u') and across-strait (v') velocities.

SST and SIC data originate from the Operational Sea Surface Temperature and Ice Analysis (OSTIA; Good *et al.*, 2020), developed by the United Kingdom Met Office. These datasets were also obtained from the Copernicus Marine Environment Monitoring Service (CMEMS; https://marine.copernicus.eu/). OSTIA provides SST data corrected for diurnal variability and includes information on sea ice coverage. This dataset is the result of reprocessing, combining both *in situ* and satellite data, and provides a grid resolution of 0.05°x0.05° (https://doi.org/10.48670/moi-00168). It is categorized as a L4 processing product and covers a temporal range from October 1981 to May 2022. The choice of this product is based on its alignment with *in situ* measurements, as reported in Veny *et al.* (2024). The time-series of daily SST and SIC up to May 2022 is extended from June 2022 to December 2022 using the near-real time product from OSTIA (https://doi.org/10.48670/moi-00165). Besides providing climatological fields of SST and SIC, the OSTIA product is also used to compute heat transport (see Section 3.2.4).

The atmospheric forcing is addressed using monthly averaged reanalysis data of wind components at 10 m and air temperature at 2 m from ERA5 (Hersbach *et al.*, 2020), which features a horizontal resolution of 0.25°x0.25°. Subsequently, the along- ($\tau_{x'}$) and across-strait ($\tau_{y'}$) wind stress components (Equation 3.1) are computed as follows:

$$\tau_{x'} = u' \cdot \rho \cdot U'_{10} \cdot C_D \,; \;\; \tau_{y'} = v' \cdot \rho \cdot U'_{10} \cdot C_D \qquad (3.1)$$

where u' and v' are the eastward and northward velocity components after being rotated 36.25° counterclockwise according to the strait orientation; ρ is the air density (1.2 kg m^{-3}); $U'_{10} = \sqrt{u'^2 + v'^2}$ is the wind speed at 10 m above the surface; and, C_D is the drag coefficient, which is a function of wind speed, U'_{10} , taking into account sea ice cover, as described by Lüpkes *et al*. (2005).

3.2.2 *In situ* data: SADCP, temperature at depth and surface drifters

We use publicly available *in situ* velocity data, collected from SADCPs, for intercomparison with the satellite-based seasonal climatologies presented in this work. Velocity measurements were rotated following the same procedure as for altimeter-derived surface velocities.

The analysis relies on two extensive datasets of direct velocity measurements collected from 1999 to 2014 with 150 kHz 'narrow band' SADCPs along ship tracks from R/V *Nathaniel B. Palmer* and R/V *Laurence M. Gould*, which navigated routinely from South America to Antarctica for logistical operations during all the seasons. Data acquisition and initial processing were accomplished by Dr. Eric Firing (University of Hawaii) and Dr. Teresa Chereskin (Scripps Institution of Oceanography). Velocity profiles were acquired and processed with UHDAS (University of Hawaii Data Acquisition System) and CODAS (Common Ocean Data Access System), respectively. The processed 5 min averaged transect data we use in this work can be found at the Joint Archive for SADCP (JASADCP) webpage, https://uhslc.soest.hawaii.edu/sadcp/. For processing details the reader is referred to Lenn *et al*. (2007) and Firing *et al*. (2012). Profiles collected from *R/V Nathaniel B. Palmer* have a vertical resolution of 8 m from 31 to 503 m depth, while profiles collected from *R/V Laurence M. Gould* have a vertical resolution of 10 m from 30 to 1040 m depth. We address vertical interpolation on standard depth levels through both datasets towards a common 10 m vertical resolution starting at 30 m depth. Before gridding the data, the barotropic tidal signal was removed using the Circum-Antarctic Tidal Simulation (CATS2008), an update to the model described by Padman et al. (2002). Then, seasonal climatologies of the BC were constructed (Veny *et al.*, 2022). We inspect the SADCP-based seasonal climatologies further in this work for intercomparison with satellite-based climatologies. Lacking enough *in situ* measurements over the domain of the CC, we address this knowledge gap by using synoptic SADCP data (https://data.mendeley.com/datasets/g58z4mczs7/1) collected by the R/V *Akademik Ioffe* (AI) and R/V *Akademik Sergey Vavilov* (ASV) in 2017 (Frey *et al.*, 2021a, 2023). These measurements were taken on 24th November 2017 (transect 54tr3_2) and 18-19 December 2017 (transect 45tr5_3), respectively. The transect 54tr3_2 surveyed a section from AP to Livingston Island, while the transect 45tr5_3 surveyed a section from the Antarctic Sound to King George Island.

Seasonal temperature fields derived from the climatology presented in Dotto *et al.* (2021; https://zenodo.org/records/4420006) are used to compute heat transport (see Section 3.2.4). This climatology is constructed using CTD, MEOP and Argo float measurements in the northern AP and adjacent regions from 1990 to 2019. For consistency, we define seasons hereafter following Dotto *et al.* (2021): summer (January-March), autumn (April-June), winter (July-September) and spring (October-December). The spatial grid resolution is approximately 10 km with profiles linearly interpolated onto 90 depth levels.

Lastly, data from the NOAA Global Drifter Program (GDP) buoys ('drifters'), available from 1979 to the present, are also analysed. The data have been processed by the Drifter Data Assembly Center (DAC) at Atlantic Oceanographic and Meteorological Laboratory (AOML), applying optimal interpolation to generate records at 6-hour intervals (Lumpkin and Centurioni, 2010). The data include time, positions (latitude and longitude), SST, and surface velocities (eastward and northward components). The surface drifter data are analysed in the Appendix A to assess the feasibility of producing seasonal climatological fields that provide an overview of the ocean circulation in the BS, incorporating both boundary currents and direct measurement-based data, given the lack of SADCP measurements covering the entire strait, which prevents a complete depiction of strait-wide circulation. Before starting to process the drifter data, the barotropic tidal signal was removed using the CATS2008, as done for the SADCP data. The data was then gridded into cells with a resolution of 25 km, matching the resolution of the altimetry data shown in Figure 3.2. To address the irregular spatial and temporal distribution of the data, we applied a step-by-step time-averaging scheme following Veny *et al*. (2022).

3.2.3 Reanalysis products: sea surface currents

We analyse ocean circulation velocity data from the GLobal Ocean ReanalYsis and Simulation (GLORYS12V1; https://doi.org/10.48670/moi-00021), a global ocean reanalysis product provided by the European Union's CMEMS. This dataset is generated from coupling ocean-ice models: the version 3.1 of the Nucleus for European Modelling of the Ocean (NEMO) and the version 2 of the Louvain-la-Neuve-Ice Model (LIM2). The common source of atmospheric forcing data is from ERA-Interim. This database covers the period from January 1993 to June 2021 with a horizontal resolution of 1/12° and a vertical resolution of 50 z-levels from surface to 5727.9 m depth. However, our dataset is limited to the period from January 1993 to December 2020 to ensure a consistent number of months for each year.

In addition, we also assess Global Ocean Forecasting System (GOFS) 3.1 output on the GLBv0.08 grid, a version of the global HYCOM-based product (HYbrid Coordinate Ocean Model; https://www.hycom.org/dataserver/gofs-3pt1/reanalysis), from the institution Naval Research Laboratory: Ocean Dynamics and Prediction Branch. The product provides data with 40 vertical levels, a horizontal resolution of 0.08° between 40°S and 40°N, increasing to 0.04° beyond these latitudes, and a temporal resolution of 3 hours, covering the period from 1994 to 2015. The system uses the Navy Coupled Ocean Data Assimilation (NCODA) system, assimilating satellite and *in situ* sea surface observations, as well as vertical temperature and salinity profiles from Expendable Bathythermographs (XBTs), Argo floats, and moored buoys.

Analogous to the objective pursued with the drifter data, in the Appendix A, we aim to complement the analysis of remotely sensed observations with an analysis of the aforementioned reanalysis products to assess the feasibility of producing seasonal climatological fields that provide an overview of ocean circulation in the BS.

3.2.4 Estimation of near-surface volume and heat transport

Based on Figure 9 in Frey *et al.* (2023), we note that assuming barotropicity beyond 100 m would not be a realistic assumption relying solely on satellite data. For this reason, we use the same bottom boundary and focus our analysis in the upper 100 m, where the wind stress forcing and sea-ice formation processes play major roles in the ocean dynamics. The along-strait near-surface volume transport, U', driven by the boundary currents in the BS from the surface down to 100 m depth (Equation 3.2) is calculated as follows:

$$U'(x',t) = \int_0^{D_T} \int_h^{h_0} u' dz dy' \qquad (3.2)$$

where x' is the along-strait coordinate; D_T corresponds to the length of the across-strait transects (in m); the terms h_0 and h refer to the shallowest and deepest depths considered, set at 0 m and 100 m, respectively; and u' is the along-strait velocity component (in m s^{-1}) after counterclockwise rotation of 36.25°. To distinguish between the BC and CC domains, we use the 0 cm s^{-1} isoline as the boundary of integration along x'. At depth, we use the vertical gradient of the BC velocity profile from Figure 9 in Frey *et al.* (2023), to accommodate its baroclinic nature for each altimeter-derived surface geostrophic velocity profile. In contrast, for the CC, which has been reported as predominantly a barotropic current, at least during spring and summer (Morozov, 2007; Savidge and Amft, 2009; Poulin *et al.*, 2014; Veny *et al.*, 2022; Frey *et al.*, 2023), the same altimeter-derived surface geostrophic velocity is applied throughout the entire water column (i.e. the integral through depth is omitted and replaced by times the extent of the water column under consideration, which is here 100 m).

The near-surface heat transport, Q_h (Equation 3.3) is computed as follows:

$$Q_h(x', t) = \rho\, c_p \int_0^{D_T} \int_h^{h_0} u'\left(T_i - T_{ref}\right) dz dy' \qquad (3.3)$$

where x' is the along-strait coordinate; ρ is the seawater density (1025 kg m^{-3}); c_p is the specific heat capacity of seawater (in J kg^{-1} °C^{-1}); D_T corresponds to the length of the across-strait transects (in m); the terms h_0 and h refer to the shallowest and deepest depths considered (in m); u' is the along-strait velocity component (in m s^{-1}); and $T_i - T_{ref}$ represents the temperature anomaly at position i with respect to the reference, which is -1.8 (the freezing temperature, in °C). We use two different databases and assumptions regarding the temperature field. First, we allow a vertical variation of the temperature field following the seasonal climatology developed by Dotto *et al.* (2021), hence using 0 m and 100 m as vertical boundaries. Second, we assume SST is constant within the first 10 m of the water column (i.e. the integral through depth is, in this latter case, omitted and replaced by times the extent of the water column under consideration, which is here 10 m).

3.3 Results and discussion

3.3.1 Surface dynamics of the boundary currents

Previous studies have extensively explored the relationship between geostrophic circulation derived from satellite altimetry and direct velocity measurements across various oceanic regions finding a high correlation (Barré *et al.*, 2011; Ferrari *et al.*, 2017; Frey *et al.*, 2021b; Lago *et al.*, 2021). Recently, it has been shown that the mean geostrophic circulation revealed by altimeter-based maps agreed well with the spatial structure of the BC as compared to direct velocity measurements, although the CC was declared not to be clearly represented and, hence, a further description was prevented (Frey *et al.*, 2023). Generally, the comparison between the altimeter-derived surface geostrophic velocity and SADCP measurements showed qualitative coherence, though interpolated altimetry data over the surveys dates always indicated weaker boundary current velocities than *in situ* observations. Frey *et al.* (2023) attributed this discrepancy to the unique environmental factors of the region, including small spatial-scale features and the pronounced influence of ocean tides. These tides can drive regional sea level changes of several tens of centimeters (Zhou *et al.*, 2020), while satellite altimetry data rely on tide models to correct such variations. Unfortunately, these tide models exhibit significant inaccuracies in the region (King and Padman, 2005), hence contributing to the observed discrepancies. These limitations compromise the reliability of altimetry-derived geostrophic currents for capturing short-term variability or episodic events in the strait.

Overall, Frey *et al.* (2023) found that BC velocity values in the 0.25º resolution altimetry product were 2.2 times lower than SADCP values when synoptic measurements were compared (i.e. concomitant altimeter-derived velocities and direct velocities measured from SADCPs). Notably, Veny *et al.* (2022), using climatological velocity fields from SADCP data, reported seasonal variations in the BC, with maximum current speeds during the austral summer. In contrast, Frey *et al.* (2023), using satellite altimetry data, reported maximum current speeds during austral autumn and minimum speeds (15% lower) in spring. As previously discussed, this mismatch between SADCP and altimetry-derived velocities can likely be attributed to the fact that these datasets represent different ocean layers, which inherently capture distinct dynamics (i.e. SADCP depth-averaged values in Veny *et al.* (2022) data refer to the 80-100 m depth layer). Additionally, the irregularity of SADCP transects may influence the resulting climatology, and they must be considered as a first-order climatological approximation.

Given that variations in the BC on time scales of several days can be as significant as seasonal variations, a substantially larger SADCP dataset is required to improve the robustness of seasonal variability estimates. For this reason, in this work we focus on the use of satellite altimetry data to assess climatological long-term variations (seasonal scale) in the dominant flows of this dynamic area. We do so by comparison of climatological fields built upon satellite-derived and climatological direct velocities of the BC, where quantitative offsets due to small spatial-scale features and ocean tides are expected to smooth out.

The altimeter-derived seasonal circulation west of the AP is presented in Figure 3.2. The colour shading represents the magnitude of the geostrophic velocities, while the direction of the currents is shown using unit vectors, which indicate flow direction. The boundary currents in the BS, namely, the

BC and the CC, are clearly visible forming a cyclonic-like circulation within the strait (Sangrà *et al.*, 2011, 2017; Gordey *et al.*, 2024). Although both boundary currents are noticeable in all seasons, their intensity and structure are shown to vary in space and time.

From summer to winter (Figure 3.2a-c), the BC flows northeastward as a narrow jet leaving the SSI to its left-hand side, being stronger and wider downstream of Greenwich Island, and up to King George Island with maximum velocities up to 20 cm s^{-1}. In spring, the BC retains its general structure but weakens slightly compared to former seasons toward maximum velocities up to 17 cm s^{-1}, as also seen in Figure 14 from Frey *et al.* (2023). Following this, the BC decelerates to 5-8 cm s^{-1} as it approaches the recirculation around the SSI, as shown in previous studies based on direct velocity measurements and subsurface drifters (Sangrà *et al.*, 2011, 2017; Veny *et al.*, 2022).

Differently, the CC appears as a wider and slower current that flows southwestward leaving the AP to its left-hand side (Figure 3.2). Here, the CC does not exhibit a clear seasonality in terms of spatial structure. However, there is a notable contrast in velocity patterns: from summer to autumn (Figure 3.2a-b), velocities over the CC domain are predominantly higher and about 4–6 cm s^{-1}, whereas during winter and spring (Figure 3.2c-d), velocities decrease to approximately 1–2 cm s^{-1}. These results are consistent with depth-averaged velocities of approximately 6 cm s^{-1} estimated for the CC based on SADCP data (Figure 9 in Frey *et al.* (2023)).

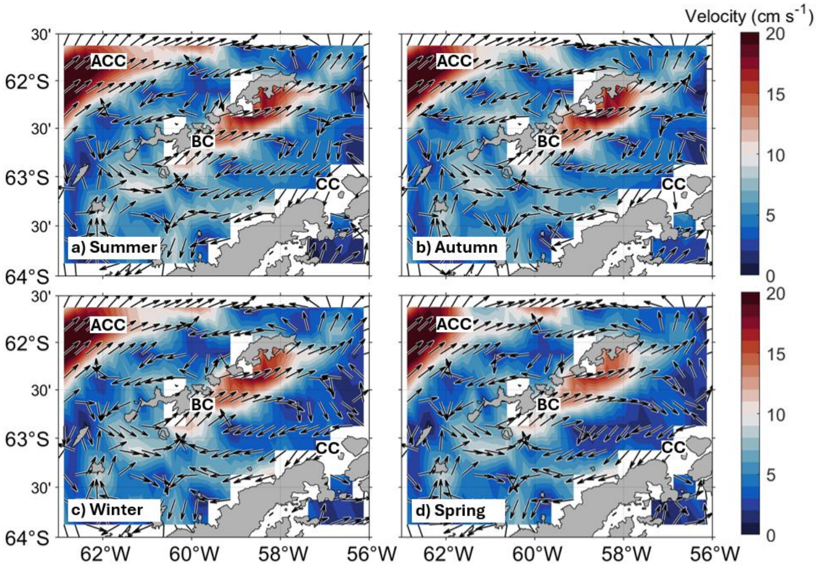

Figure 3.2. Seasonal surface circulation (shades of colours) from altimeter-derived geostrophic velocities using data from DUACS multimission altimeter data processing system: a) summer (Jan-Mar), b) autumn (Apr-Jun), c) winter (Jul-Sep), and, d) spring (Oct-Dec). The climatologies are seasonally-averaged from January 1993 to December 2022. The vector velocity field is shown as unit vectors, while the magnitude is shown as shades of colors (see colorbar in cm s^{-1}). The main currents are also indicated: Bransfield Current (BC) and Antarctic Coastal Current (CC), flowing as boundary currents in the Bransfield Strait; and, the Antarctic Circumpolar Current (ACC), north of the South Shetland Islands in the Drake Passage.

Figure 3.3 presents a key highlight in the characterization of the western boundary currents in the BS, presenting a monthly climatology of ocean circulation over three across-strait transects. These climatologies are derived from 30 years (1993-2022) of along-strait altimeter-based surface geostrophic velocities (u', in cm s^{-1}) and displayed as Hovmöller diagrams. From left to right, the panels illustrate observations for the Western Transect (WT), Central Transect (CT), and Eastern Transect (ET), respectively, with their locations detailed in Figure 3.1. These three transects are situated within the central basin of the BS and extend from the SSI (0 km) to the AP (approximately 120 km). Positive velocity values (red) indicate northeastward flows, while negative values (blue) represent southwestward flows. The solid black contour line (0 cm s^{-1}) in Figure 3.3, highlights the transition zone between the BC and the CC. This figure provides a comprehensive view of the temporal and spatial variability of the boundary current, contributing to our understanding of the BS circulation.

Across all three transects, the geostrophic velocities show persistent northeastward flow near the SSI and southwestward flow near the AP throughout the climatological year. This pattern reflects the presence of the BC and CC, which are relatively stable and persist year-round. For the BC, these findings align with climatological fields derived from direct velocity measurements reported by Veny *et al.* (2022). Regarding the CC, the continuous presence of this current along the AP throughout the year is reported here for the first time.

From west to east (Figure 3.3a to Figure 3.3c), the BC experiences a widening whereas the CC experiences a narrowing. This downstream pattern of the BC is similar to that reported by previous works (Veny *et al.*, 2022; Frey *et al.*, 2023). In terms of spatiotemporal variability, the spatial extent of the BC and the CC remains nearly invariant along the WT, increases toward the CT, and reaches its maximum variability in the ET, where strong seasonal variability is observed. In this context, the BC and CC exhibit widths of approximately 40 km and *ca.* 65 km, respectively, along the WT. Along the CT, the BC varies in width from 45 km during late summer and early autumn to 55 km in early spring whereas the CC varies from 65 km during late summer and early autumn to 55 km in early spring. Lastly, along the ET, the BC and CC exhibit prominent across-strait excursions. The BC reaches its maximum extension of 85 km in spring, while the CC contracts to a minimum of 30 km. Conversely, from summer to early autumn, the BC reduces its extent to 55 km, whereas the CC expands to a maximum of 60 km.

In terms of current speed, the BC also experiences a strengthening up to King Goerge Island, with maximum velocities of 10 cm s^{-1} throughout all the year when closest to the Bellingshausen Sea (WT), and maximum velocities of 18 cm s^{-1} from mid-summer to mid-winter when closest to the Weddell Sea (ET). From east to west (downstream of the CC in Figure 3.3c to Figure 3.3a), the flow experiences a slight increase in maximum velocities from 4 cm s^{-1} in late spring to mid-winter to 8 cm s^{-1} in mid-winter to early spring. The CC weakens slightly toward the other seasons while maintaining a consistent southward flow.

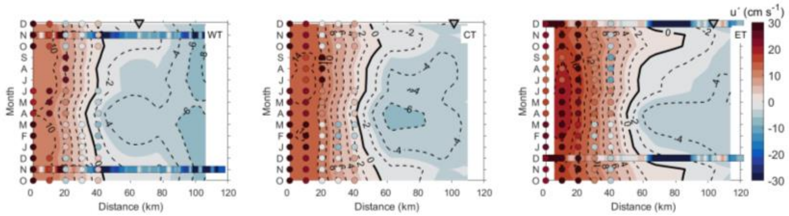

Figure 3.3. Hovmöller diagram of monthly climatology of altimeter-derived surface geostrophic velocity (cm s^{-1}) across the three transects of study (WT, CT and ET; see their locations in Figure 3.1) using data from DUACS multimission altimeter data processing system. The climatologies are monthly-averaged from January 1993 to December 2022. The x-axis shows the distance along the transect (in km), and the y-axis represents the months of the climatological year, starting in October and continuing through to the following December to highlight the annual pattern. The widths of the transects are 105 km, 110 km, and 115 km, respectively. Positive values (shades in red) mean northeastward flows, while negative values (shades in blue) mean southwestward flows. The contour line for 0 cm s^{-1} is highlighted in solid black contour. The Bransfield Current flows year-round next to the South Shetland Islands (0 km in the y-axis), while the Antarctic Coastal Current flows next to the Antarctic Peninsula (120 km in the y-axis). Inverted grey triangles represent the position of the 200 m isobath in each transect. Coloured circles above each monthly section represent seasonal mean surface velocity values derived from SADCP climatologies by Veny *et al.* (2022). Seasonal climatological values are placed above the months they precede: summer (Jan–Mar), autumn (Apr–Jun), winter (Jul–Sep), and spring (Oct–Dec). The coloured squares above each monthly section represent synoptic measurements collected along transects presented in Frey *et al.* (2023), after applying the same rotation to the reference system as used in our analysis. These transects were surveyed on 24 November 2017, from the Antarctic Peninsula to Livingston Island (AI54tr3_2), and on 18–19 December 2017, from Antarctic Sound to the King George Island (ASV45tr5_3; see Figure 3.1).

Lastly, we compare the altimeter-derived surface geostrophic velocity with surface SADCP measurements, incorporating both seasonal climatologies (represented by circles) from Veny *et al.* (2022) and synoptic transects (represented by squares) from Frey *et al.* (2023). While the comparison reveals qualitative consistency, the SADCP velocities are quantitatively higher than the altimetry-derived fields as previously accounted for. Nevertheless, the altimetry successfully captures the BC widening and strengthening from the WT to the ET, aligning with SADCP observations. This consistency indicates that the climatological dataset is robust, benefiting from the averaging of 30 years of monthly data. Additionally, tidal error effects in the BS evident in the altimetry data become negligible through this long-term averaging (Frey *et al.*, 2023). These findings highlight the importance of long-term satellite monitoring for analysing spatiotemporal interactions among boundary currents in the BS, providing the baseline knowledge to assess the role of ocean-atmosphere players driving the long-term variability of the ocean circulation in the BS.

3.3.2 Ocean-atmosphere-ice interactions within the boundary current domain

This section examines the interaction between ocean and atmosphere through the variability of SST, air temperature and sea ice cover across the three transects. This integrated analysis aims to elucidate the ocean-atmosphere drivers that influence the interplay of forcing mechanisms governing the boundary currents.

Figure 3.4 presents the monthly climatology of SST across the three transects. Highest temperatures (in red shades) appear from January to March (summertime) while lowest temperatures (in blue shades) prevail from June to

November (winter to early spring) across all transects. The overall pattern indicates a greater seasonal amplitude of SST within the BC domain (ranging from 1.4ºC to -1.4ºC) compared to the CC domain (ranging from 0.6ºC to -1.7ºC).

The warming period exhibits the same duration across the transects but features a broader and warmer pool of water downstream of the BC, particularly in the central and eastern transects. This occurs in accordance with the downstream widening of the BC (Figure 3.3 and 3.4). During this period, the isotherm of 0.6ºC works out as a proxy of the PF as indicated in Veny *et al.* (2024). The PF appears more prominently from mid-December to mid-March, extending up to 60 km from the SSI along the WT, and up to 70-80 km along the CT and ET. Here, the ET shows the most extensive warming, with temperatures reaching 1.4°C within 0 to 50 km from the SSI, while in the WT and CT, this area extends toward 30–40 km from the SSI.

The cooling period also exhibits the same duration across the transects, from April to September (autumn to winter). However, the extent of the minimum temperature coverage is greater in the WT, as indicated by the -1.6ºC and -1.7ºC isotherms approaching the SSI. During the sea ice season, the -1.7ºC isotherm (close to the freezing-point temperature of -1.88ºC for waters with a salinity of 34.35, the threshold between TBW and TWW (Sangrà *et al.* (2017)) covers distances from 40 to 120 km near the AP; encompassing the domain of the CC.

To further frame our findings, the monthly SST climatologies are compared with seasonal climatologies of *in situ* temperatures (represented by horizontal coloured lines in Figure 3.4) from Dotto *et al.* (2021). It is important to highlight that the seasonal dataset is compared against monthly values in this analysis, requiring the repetition of seasonal values across three consecutive months. This comparison highlights potential differences arising from the distinct temporal resolutions of the datasets. The results reveal a spatial coherence, with each dataset exhibiting strong qualitative and quantitative similarity.

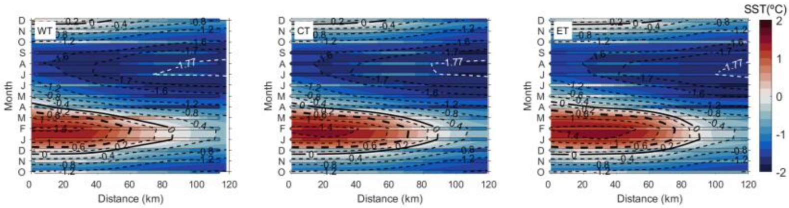

Figure 3.4. Hovmöller diagram of monthly climatology of Sea Surface Temperature (SST; °C) across the three transects of study (WT, CT and ET; see their locations in Figure 3.1) using data from OSTIA. The climatologies are monthly-averaged from January 1993 to December 2022. Positive SSTs are shown in red, while negative SSTs are shown in blue. The thick dashed black contour indicates the position of the isotherm of 0.6ºC (proxy of the Peninsula Front as suggested in Veny *et al.*, 2024). The isotherm of 0ºC is highlighted in thick solid black contour. The isotherm of -1.77ºC is indicated in white as a reference contour for near-freezing waters (closest to the freezing-point temperature of -1.88ºC for waters with a salinity of 34.35, the threshold between TBW and TWW (Sangrà *et al.* (2017)), where sea ice coverage is expected. Horizontal coloured lines above each monthly section represent seasonal mean surface temperature values derived from Dotto *et al.* (2021) seasonal climatologies. Seasonal climatological values are placed above the months they precede: summer (Jan–Mar), autumn (Apr–Jun), winter (Jul–Sep), and spring (Oct–Dec).

The spatial and temporal variability of the air temperature fields in BS are presented in Figure 3.5. The atmosphere warming period exhibits an analogous pattern as observed in the ocean: the duration across the transects is the same, featuring a broader extent and warmer air temperatures downstream of the BC, particularly in the CT and ET (the 0ºC isotherm extends up to 110–120 km in the CT and ET, compared to 100 km in the WT). Conversely, air temperatures decrease over the CC domain more sharply and persist for a longer cooling period near the Bellingshausen Sea, reaching values as low as -10ºC, compared to the Weddell Sea, where minimum air temperatures are around -8ºC.

By comparing Figures 3.4 and 3.5, the coupling between SST and air temperature becomes evident. Air temperature values (Figure 3.5) are generally higher along the SSI than near the AP, closely mirroring the spatial distribution of SST patterns (Figure 3.4). Notably, the -1.7ºC SST isotherm, which is close to near-freezing waters (-1.77ºC in Figure 3.4) and potential sea ice presence, consistently corresponds to air temperatures of approximately -6.5ºC.

During summertime, SST peaks (Figure 3.4) over the BC show a 15-day lag relative to periods of highest air temperature (Figure 3.5). Specifically, atmospheric temperatures peak at approximately 1ºC in mid-January, whereas ocean temperatures reach their maximum of 1.4ºC in early February. During winter, the coldest temperature conditions over the CC are reached in July, with air temperatures ranging from -10ºC in the WT to -8ºC in the ET, while ocean temperatures remain above -1.7ºC. Notably, one month later, the ocean extends the area embedded by the -1.6ºC isotherm, reflecting a delayed oceanic response to atmospheric cooling.

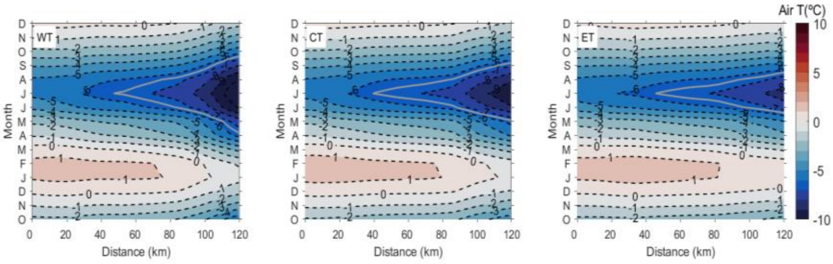

Figure 3.5. Hovmöller diagram of monthly climatology of air temperature (ºC) across the three transects of study (WT, CT and ET; see their locations in Figure 3.1) using data from ERA5. The climatologies are monthly-averaged from January 1993 to December 2022. Positive temperatures are shown in red, while negative temperatures are shown in blue. The isotherm of -6.5ºC is highlighted in thick solid gray contour.

The spatial and temporal variability of SIC across the transects is presented in Figure 3.6. A SIC percentage of 15% is the threshold for considering significant sea ice presence, which starts in May through all the three transects and remains until October (Figure 3.6). The timing and extent of SIC show a strong relationship with air temperature fields (Figure 3.5), particularly over the CC domain during late autumn through early spring. Sea ice begins forming in May across all transects when air temperatures drop below 0ºC, and its presence persists until October. This coincides with the cooling phase of the air temperature fields.

Notably, SIC reaches maximum values of 50% in July, aligning with the coldest ocean and air temperatures (Figures 3.4 and 3.5). However, the area with SIC exceeding 50% is larger along the AP and near the Weddell Sea (ET), where air temperatures are slightly higher than those near the Bellingshausen Sea (WT; Figure 3.5). This seemingly counterintuitive pattern reflects the influence of oceanic forcing on sea ice formation, as waters near the Weddell Sea are colder than those near the Bellingshausen Sea (Figure 3.4), promoting more extensive sea ice development despite the relatively higher atmospheric temperatures.

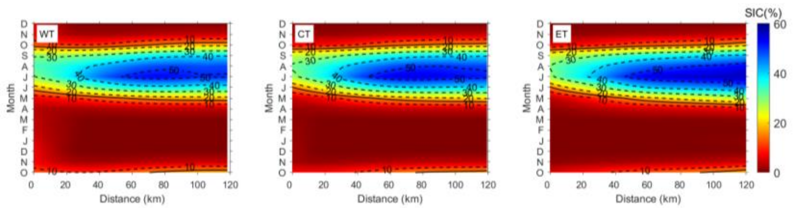

Figure 3.6. Hovmöller diagram of monthly climatology of Sea Ice Coverage (SIC; %) across the three transects of study (WT, CT and ET; see their locations in Figure 3.1) using data from OSTIA. The climatologies are monthly-averaged from January 1993 to December 2022. Regions with the lowest SIC are represented in red, while those with the highest SIC are depicted in blue. The solid black line represents the 15% SIC threshold, indicating the minimum value for significant sea ice presence.

The lagged oceanic response, as described previously, and evident in the expansion of the -1.6ºC SST isotherm one month after the coldest air temperatures are recorded, is also reflected in the broader extent of sea ice coverage in the WT. Here, SIC exceeds 30%, spreading extensively over the larger area covered by the -1.6ºC isotherm near the SSI, highlighting the close interplay between oceanic cooling and sea ice formation dynamics. The SIC retreats completely during spring across all transects, mirroring the warming period observed in both air and ocean temperature fields. This pattern underscores the combined influence of atmospheric and oceanic forcing in governing sea ice dynamics within the region (Vorrath *et al.*, 2020).

3.3.3 Wind stress forcing and surface geostrophic velocities: correlation analysis

This section aims to examine the relationship between wind stress forcing and surface geostrophic velocities in the BC and CC, focusing on seasonal and spatial variations across the three transects of study. The Hovmöller diagram of monthly climatology of wind stress (Figure 3.7) rotated 36.25º counterclockwise to align with the strait axis provides a detailed representation of the wind stress forcing on the BC and the CC across the three transects of study. This orientation highlights the along-strait wind stress variability, revealing seasonal patterns that drive significant changes in the dynamics and spatial extent of the BC and CC.

Elevated wind stress values (τ_x, >0.015 N m^{-2}; Figure 3.7) occur predominantly during winter and spring (July-December), peaking at τ_x,≈0.03 N m^{-2} in October, increasing the BC strength from the WT to the ET (Figure 3.3), and coinciding with low SST and air temperatures (Figures 3.4 and 3.5). During this period, the BC exhibits broader spatial extents (~40 km along the WT, ~55 km along the CT, and ~80 km along the ET; Figure 3.3, where u' > 0 cm s^{-1}), while the CC weakens and narrows significantly (~65 km along the WT, ~55 km along the CT, and ~35 km along the ET; Figure 3.3, where u' < 0 cm s^{-1}). This agrees with the notion that westerlies (i.e. regional wind stress forcing) favour the BC while opposing the CC (Vorrath *et al.*, 2020; Wang *et al.*, 2022).

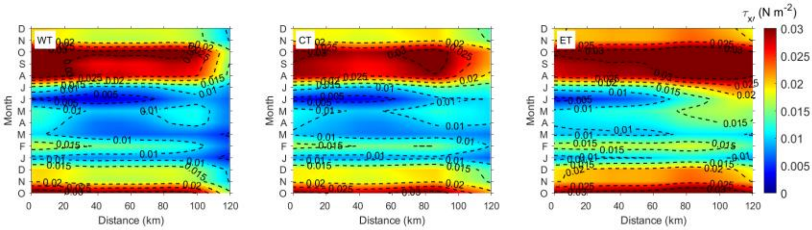

Figure 3.7. Hovmöller diagram showing the monthly climatology of wind stress (N m^{-2}) rotated 36.25° counterclockwise to align with the strait axis, illustrating the wind stress forcing on the Bransfield Current (BC) and Antarctic Coastal Current (CC) across the three transects of study (WT, CT and ET; see their locations in Figure 3.1) using data from ERA5. The climatologies are monthly-averaged from January 1993 to December 2022.

To quantify this relationship, we compute the correlation between rotated velocities from altimeter-derived currents (Figure 3.3) and wind stress using monthly climatological data (Figure 3.7). The results reveal that wind stress forcing exhibits varying influence across the transects, with differences in magnitude and spatial extent (Figure 3.8).

A high positive correlation, greater than 0.6 (p-value < 0.5), is observed between the BC velocity field and wind stress across much of the BS. This relationship indicates that increases in wind stress correspond to a strengthening of the northeastward-flowing BC. This behaviour aligns with the previously identified widening of the BC under elevated wind stress conditions, as illustrated in Figures 3.3 and 3.7. The positive correlation extends over a broader domain upstream of the CC, reflecting the BC's widening, particularly in the ET transect (Figure 3.8). The correlation coefficient gradually diminishes to zero at increasing distances from the SSI, marking the transition zone between the BC and CC along the three transects of study, consistent with Figure 3.3.

Beyond this transition zone, the correlation turns negative, ranging between -0.7 and -0.6 (p-value < 0.5), indicating that as wind stress increases, the southwestward-flowing CC tends to weaken. This inverse relationship is strongest upstream of the CC (ET in Figure 3.8), with negative correlation values greater than -0.7 (p-value < 0.5). This pattern reflects the opposing directions of wind stress and CC flow, where increased wind stress hinders the CC's strength.

These results align with previous modelling studies (e.g., Vorrath *et al.*, 2020; Wang *et al.*, 2022), and assess quantitatively for the first time the influence of wind-driven dynamics on the western boundary currents in the BS based on climatological satellite observations. An open question relates to the climatological forcings at deeper layers, which are governed by other mechanisms such as baroclinic instabilities or density gradients (Sangrà *et al.*, 2011, 2017).

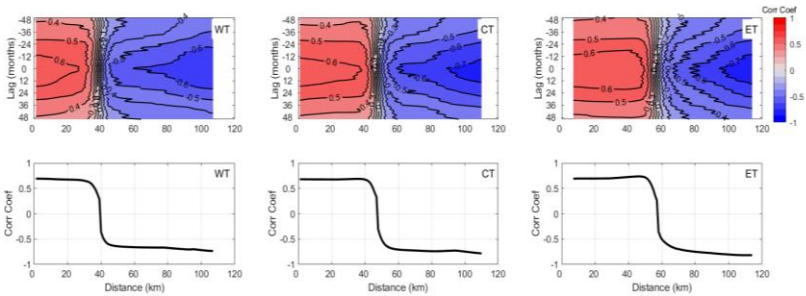

Figure 3.8. Correlations between monthly rotated altimeter-derived surface geostrophic velocity and wind stress across the three transects of study (WT, CT and ET; see their locations in Figure 3.1). Data used covers the period from January 1993 to December 2022. From top to bottom, each panel shows a Hovmöller diagram of correlation coefficients with varying monthly lag along each transect and the maximum correlation at each distance along the transect.

3.3.4 Monthly climatology of near-surface volume and heat transport and interbasin balances

The near-surface interbasin volume and heat exchange is analysed through the monthly climatological volume and heat transports, and associated balances across the three transects of study. The estimates, represented by red lines for the BC and blue lines for the CC, illustrate the variability over the year. The volume transport was derived from altimeter-derived geostrophic velocities (Figure 3.9a-d), whereas heat transport was computed using surface geostrophic velocities combined with seasonal climatological temperature profiles (Figure 3.9e-h) from Dotto *et al.* (2021), and satellite-derived sea surface temperatures (Figure 3.9i-l), as described in Section 3.2.4. The volume transport estimates of the CC were converted to positive to avoid overly broad axis limits in the graphical representation. However, we must note that these values are inherently negative, as they correspond to the southwestward flow of the CC. Lastly, the transport estimates are constrained to the surface layer, down to a depth of 100 meters. This approach adopts a conservative assumption to ensure the robustness of the results, as the analysis focuses on the upper 100 meters, where wind stress forcing and sea-ice formation processes play a major role in ocean dynamics. In contrast, SST calculations are confined to the uppermost 10 meters. Regarding the heat transport estimates, we note that both boundary currents transport water masses above the freezing point, which is used here as the reference temperature (see Section 3.2.4). Thus, in Figure 3.9, positive heat transport values for the BC (red lines) indicate northeastward transport of relatively warm waters originating from the Bellingshausen Sea and Gerlache Strait, while positive heat transport values for the CC (blue lines) indicate southwestward transport of relatively cold waters originating from the Weddell Sea.

3.3.4.1 Volume transport

Across all three transects (Figure 3.9a-c), the volume transport of the CC displays a consistent annual cycle and exhibits greater variability than the BC. The highest seasonal amplitude is observed in the ET, with an overall decline in volume transport as it progresses eastward (downstream of the CC). The seasonal amplitude oscillates between minimum values in spring and maximum values in summer, as follows: 0.05–0.33 Sv in the ET; 0.12–0.35 Sv in the CT; and, 0.19–0.38 Sv in the WT. Differently, the BC volume transport remains relatively stable across all transects, with a seasonal amplitude of 0.1 Sv and a slight gradual transport increase from west to east transects. The seasonal amplitude of the BC volume transport oscillates between a minimum in late summer and a maximum in early spring for the CT and ET, as follows: 0.24–0.33 Sv in the WT, 0.41–0.50 Sv in the CT, and 0.52–0.64 Sv in the ET.

The pattern suggests opposing dynamics between the systems, particularly across the WT and CT, which become more pronounced through mid-summer, mid-autumn, and spring. During these seasons, BC volume transport increases as CC volume transport decreases, and vice versa, highlighting their contrasting seasonal behaviour.

The observed spatiotemporal variability in the volume transport of the BC and the CC provides a broader seasonal perspective compared to findings reported in the literature, and based on observations. Only two previous studies (Savidge and Amft, 2009; Veny *et al.*, 2022) present climatological estimates for the BC volume transport derived from direct velocity measurements over extended observation periods. In both cases, the description of the CC was prevented due to a lack of observations. The first study, Savidge and Amft (2009), could only report climatological transport values for the BC during summer. Their results showed that the transport (40–375 m depth) increases, particularly doubling from approximately 1 Sv near Boyd Strait to around 2 Sv east of Livingston Island, and remaining high further east, aligning with our observations. The second study, Veny *et al*. (2022), reported volume transport values (30–250 m depth; their Figure 8) for the BC across all seasons. Their findings also demonstrated a consistent increase in BC volume transport along the southern shelf of the SSI, almost doubling from Livingston Island (0.71 ± 0.14 Sv) to King George Island (1.55 ± 0.22 Sv), which is consistent with the results presented in this study. Lastly, Veny *et al*. (2022) reported that downstream of Nelson Strait, volume transport estimates showed no significant seasonal differences, averaging 1.31 ± 0.20 Sv. Similarly, our study observes no significant differences across seasons but extends this observation to the entire shelf of the SSI.

More recently, Gordey *et al*. (2024) also reported reduced spatial variability in the along-strait transport of the BC and CC down to 600 m depth with average values of 1.5–1.8 Sv and 0.7–0.8 Sv, respectively. This description was achieved following direct velocity measurements collected from 108 transects conducted during eight cruises in the austral summers (November–March) between 2015 and 2022. This highlights the complementary nature of studies based on long-term synoptic transects and climatological approaches in characterizing transport dynamics across the strait.

Regarding the volume transport driven by the CC, to the best of our knowledge no previous studies in the literature have addressed its seasonal variability from an observational perspective. For a detailed review of volume transport estimates for the BC, the reader is referred to Table 1 in Veny *et al*. (2022).

Compared to previous studies, it must be noted that their transport values were calculated using integration depths different from those in this work, where the focus remains on the near-surface layer. However, when comparing spatial and temporal differences, the results remain consistent. Volume transport estimates align with an increase in BC transport toward King George Island (Sangrà *et al*, 2017; Veny *et al.*, 2022; Frey *et al.*, 2023), while providing a more comprehensive seasonal perspective and broader spatial coverage across the entire SSI shelf. The findings also align with Veny *et al.* (2022), further revealing more stable seasonal dynamics over a broader area. Additionally, the downstream increase of CC transport reported by Gordey *et al.* (2024) within BS (their Figure 8) is also consistent with our results, where we expand the report of this feature throughout the year noting a marked seasonal cycle (Figure 9). These results enhance the current understanding of BC and CC volume transport by providing a more detailed and seasonally resolved view of their variability.

3.3.4.2 Volume transport balance

When evaluating the volume transport balance to quantify the water exchange between the inflow and outflow from the Bellingshausen and Weddell seas through the BS (Figure 3.9d), we recover the negative sign of the CC's volume transport to preserve the opposite direction of its flow. The following patterns are observed.

On the one hand, the volume transport balance shows a negative slope, across all transects, from spring to summer (October to March), with values transitioning from negative to positive eastward. Minimum values are observed in all cases through the summer-to-autumn transition (March and April): -0.12 Sv in the WT, 0.06 Sv in the CT, and 0.22 Sv in the ET. Through the spring-to-summer transition (December to January), the balance crosses 0 Sv in the WT and approaches 0 Sv in the CT between March and April (0.06 Sv), when the BC and CC transport similar water volumes in opposite directions. On the other hand, the volume transport balance shows a positive slope, across all transects, from autumn to winter (April to September), with higher values eastward. Maximum values are observed in all cases through the winter-to-spring transition (September to October): 0.13 Sv in the WT, 0.37 Sv in the CT, and 0.58 Sv in the ET. Through the autumn-to-winter transition (May to July), the balance crosses 0 Sv in the WT and stays near zero throughout this period. Lastly, it is important to note that the seasonal amplitude of the volume transport balance increases from west to east, as evidenced by the differences between minimum and maximum estimates: 0.25 Sv in the WT, 0.31 Sv in the CT, and 0.36 Sv in the ET.

The above results suggest that within the first 100 m, the BS experiences a greater water mass imbalance closer to the Weddell Sea, while approaching equilibrium nearer to the Bellingshausen Sea. No previous studies have addressed the volume transport balance in the BS, which prevents further discussion in comparison with the existing literature.

3.3.4.3 Heat transport

Following the examination of volume transport, we address the heat fluxes across the BS, which are influenced by the interactions of velocity fields and temperature distributions. Thus, heat transport also exhibits distinct patterns across currents and transects (Figure 3.9e-g, i-k). Unlike volume transport, the heat transport of the BC shows a larger annual cycle and greater variability than the CC, with the seasonal amplitude increasing eastward. In contrast, the CC exhibits a smaller seasonal amplitude that decreases eastward upstream.

When heat transport computed from the Dotto *et al.* (2021) datasets down to 100 m (Figure 3.9e-g) is compared to the OSTIA datasets, which are confined to the upper 10 m (Figure

3.9i-k), similar seasonal patterns are observed. However, the OSTIA-derived results appear smoother, likely due to the inherent characteristics of each seasonal climatology, with OSTIA benefiting from regular and more systematic measurements, adding finer resolution to the seasonal variability.

For the temperature dataset from Dotto *et al.* (2021) (Figure 3.9e-g), the seasonal amplitude of heat transport driven by the BC varies from winter minima to summer maxima, with ranges as follows (higher maxima increasing eastward, downstream the BC): 0.12×10^{12} to 2.58×10^{12} W in the WT; 0.39×10^{12} to 4.36×10^{12} W in the CT; and, 1.38×10^{12} to 5.44×10^{12} W in the ET. When using the OSTIA temperature dataset (Figure 3.9i-k), the seasonal amplitude exhibits similar variability, with ranges as follows (higher maxima also increasing eastward, downstream the BC): 0.20×10^{11} to 3.52×10^{11} W in the WT; 0.33×10^{11} to 5.59×10^{11} W in the CT; and, 0.41×10^{11} to 6.67×10^{11} W in the ET.

In contrast, for the temperature dataset from Dotto *et al.* (2021) (Figure 3.9e-g), the heat transport driven by the CC exhibits lower seasonal variability, oscillating between an autumn minimum and a summer maximum, with ranges as follows (maximum estimates slightly decreasing eastwestward, upstream the BC): 0.24×10^{12} to 2.13×10^{12} W in the WT; 0.23×10^{12} to 1.87×10^{12} W in the CT; and, 0.09×10^{12} to 1.74×10^{12} W in the ET. When using the OSTIA temperature dataset (Figure 3.9i-k), the seasonal variability follows a similar pattern, but in this case the minimum is in winter, with ranges as follows: 0.04×10^{11} to 2.67×10^{11} W in the WT; 0.03×10^{11} to 2.48×10^{11} W in the CT; and, 0.02×10^{11} to 2.02×10^{11} W in the ET.

These results highlight the marked seasonal and spatial variability of the BC, which transports water masses towards the northeast in the BS. These waters are seasonally originated in the Bellingshausen Sea and Gerlache Strait, where significant seasonal temperature fluctuations exist due to summer heating and ice melting (Tokarczyk, 1987; García *et al.*, 1994; Sangrà *et al.*, 2011). Meanwhile, the CC transports more homogeneous water masses toward the southwest in the BS. These waters are originated in the Weddell Sea, exhibiting lower seasonal temperature variability due to a more limited response to seasonal thermal forcing (Grelowski *et al.*, 1986; Tokarczyk, 1987; García *et al.*, 1994; Hofmann *et al.*, 1996; García *et al.*, 2002c; Zhou *et al.*, 2002).

3.3.4.4 Heat transport balance

When evaluating the heat transport balance to quantify the heat exchange between the inflow and outflow from the Bellingshausen and Weddell seas through the BS (Figure 3.9h, l), we recover the negative sign of the CC's volume transport to preserve the opposite direction of the boundary currents. Thus, positive values of the heat transport balance indicate a larger heat transport driven by the BC, contributing to a surplus of heat towards the northeast. Conversely, negative values of the heat transport balance indicate a larger heat transport driven by the CC, contributing to a surplus of heat towards the southwest.

Overall, heat transport balances computed from the temperature climatology developed in Dotto *et al.* (2021) and the OSTIA dataset (Figures 3.9h and 3.9l, respectively) indicate a reduction in net heat transport during winter, particularly between July and August. This reduction may be attributed to the more homogeneous temperatures across the strait during this period and the larger sea-ice coverage, which reduces heat exchange between the ocean and the atmosphere. For heat transport estimates based on Dotto *et al.* (2021), the net balance (0–100 m depth) during winter approaches zero in the western and central transects, increasing to higher positive values towards the eastern transect.

For heat transport estimates based on OSTIA (0–10 m depth), the general pattern is analogous, with a notable difference: the net heat transport in the three transects of study approaches zero in winter (July and August), extending for a longer period year-round in the WT but in spring and early summer. When examining whether this feature also applies to estimates based on Dotto *et al.* (2021) but limited to the top 10 m of the water column, we observe a similar pattern. This suggests that the mismatch in net heat transport estimates in Figures 3.9h and 3.9l can be attributed to the different vertical extent considered in the computations.

Through spring, both net heat transports (Figures 3.9h and 3.9l) increase, reaching their maximum values in January before beginning a decreasing trend. This pattern becomes more pronounced moving eastward. This indicates that heat exchange is more prominent near the Weddell Sea and less prominent near the Bellingshausen Sea during spring and summer. These results provide the first comprehensive overview of the heat transport balance driven by the boundary currents of the BS.

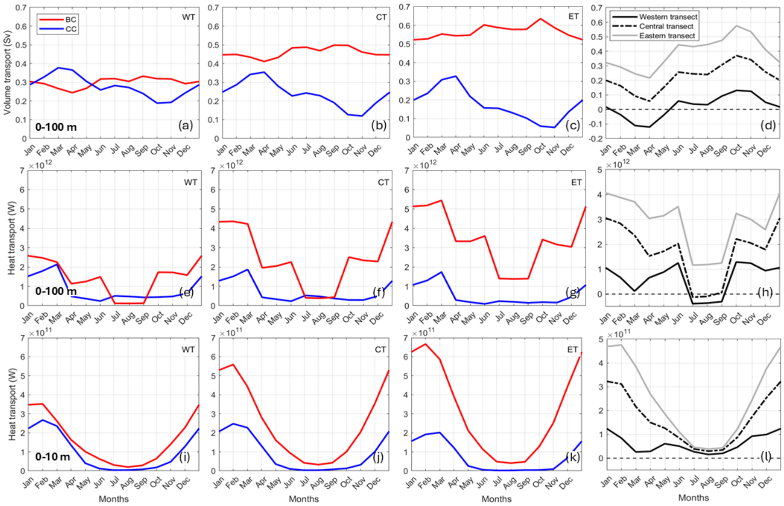

Figure 3.9. Monthly climatology of near-surface (a-d) volume (0-100 m), and (e-h, i-l) heat transport using Dotto *et al.* (2021) seasonal climatologies (0-100 m) and Sea Surface Temperature (0-10 m), respectively, across the three transects of study (WT, CT and ET; see their locations in Figure 3.1). The climatologies are monthly-averaged from January 1993 to December 2022. Seasonal climatological values from Dotto *et al.* (2021) are placed above the months they precede: summer (Jan–Mar), autumn (Apr–Jun), winter (Jul–Sep), and spring (Oct–Dec). Bransfield Current (BC) volume transport to the northeastward is shown in red, while Antarctic Coastal Current (CC) volume transport to the southwestward is shown in blue. The right-hand panels are the respective balances between the BC and the CC.

3.4 Conclusions

This study provides a comprehensive analysis of the near-surface layers of the boundary currents in the BS, using 30 years of multi-platform satellite data to assess their spatiotemporal variability and contributions to interbasin exchange.

The BC exhibits consistent strengthening up to King George Island across all seasons, with altimeter-derived volume transport (0–100 m depth) increasing from 0.24–0.33 Sv in the western transect to 0.52-0.64 Sv in the eastern transect in the BS, while decreasing downstream as it recirculates around the SSI. Heat transport peaks in summer, reaching 5.44×10^{12} W based on hydrographic climatology estimates (0–100 m depth; Dotto *et al.*, 2021) and 6.67×10^{11} W derived from the OSTIA SST product (0–10 m depth). In contrast, the CC displays pronounced seasonality in volume transport (0-100 m depth), oscillating between 0.19–0.38 Sv in the western transect and 0.05–0.33 Sv in the eastern transect in the BS. Its heat transport also peaks in summer, reaching 2.13×10^{12} W (0–100 m depth; Dotto *et al.*, 2021) and 2.67×10^{11} W (OSTIA; 0–10 m depth), respectively.

A key finding is the heat transport balance approaching zero during winter, particularly in the western transect, driven by homogeneous temperatures (due to wind-driven mixing) and extensive sea ice coverage. This marks periods of reduced interbasin heat exchange and highlights the interplay between temperature gradients, wind stress, and sea ice extent in regulating the boundary currents and local hydrography. Notably, significant positive correlations are observed between the BC and along-strait wind stress, suggesting its near-surface variability is strongly influenced by wind forcing. The CC, in comparison, displays weaker but consistent negative correlations with along-strait wind stress, indicating a distinct response to atmospheric forcing compared to the BC. These findings highlight the asymmetric contributions and forcings of the BC and CC in shaping regional hydrography, sea ice dynamics, and interbasin exchange. Furthermore, the position and strength of the PF are found to be closely tied to the distinct volume and heat transport driven by these currents, with potential impacts on local ecosystem structure and function (Veny *et al.*, 2024).

The Appendix A presents critical findings from the analysis of surface drifter data and two open-access global ocean reanalysis products, offering complementary insights into the boundary currents of the BS. On the one hand, surface drifter data confirm the downstream broadening of the BC as a coherent northeastward-flowing jet and the continuous nature of the CC flowing southwestward along the AP during summertime, emphasizing the challenges of fully characterizing their year-round variability from direct velocity measurements. On the other hand, the open-access global ocean reanalysis products (GLORYS12V1 and HYCOM) are found to inadequately represent the BS circulation. Neither product captures the CC as a continuous and spatially coherent feature, nor do they reproduce the observed heat transport balances (not shown). These limitations emphasize the importance of integrating high-resolution observational data and advancing model capabilities to better resolve boundary current dynamics in this region.

Overall, this study establishes a critical baseline for understanding climate-driven changes in the near-surface layers of the boundary currents of the BS, including shifts in volume and heat budgets, with implications for glacier melt, sea ice persistence, and, ultimately, broader Southern Ocean circulation. Future research should focus on subsurface dynamics to complement these insights, as well as on the impacts of long-term climate variability on the coupled ocean-atmosphere-ice system in the AP region.

Chapter 4

Biophysical coupling and phytoplankton blooms

This chapter has been published as:

Veny, M., Aguiar-González, B., Marrero-Díaz, Á., Pereira-Vázquez, T., & Rodríguez-Santana, Á. (2024). Biophysical coupling of seasonal chlorophyll-a bloom variations and phytoplankton assemblages across the Peninsula Front in the Bransfield Strait. *Ocean Science*, *20*, 389–415. https://doi.org/10.5194/os-20-389-2024.

4.1 Introduction

Antarctic marine ecosystems are highly dependent on the seasonal cycle of the ocean–atmosphere interaction and associated sea ice dynamics (Schofield *et al.*, 2010; Ducklow *et al.*, 2013; Montes-Hugo *et al.*, 2009; Sailley *et al.*, 2013; Brown *et al.*, 2019). Through this work we aim to characterize the seasonal variability in the biophysical coupling supporting the surface chlorophyll-a bloom in the Bransfield Strait (BS; Figure 4.1), which is located in the Southern Ocean (SO) between the South Shetland Islands (SSI) and the Antarctic Peninsula (AP).

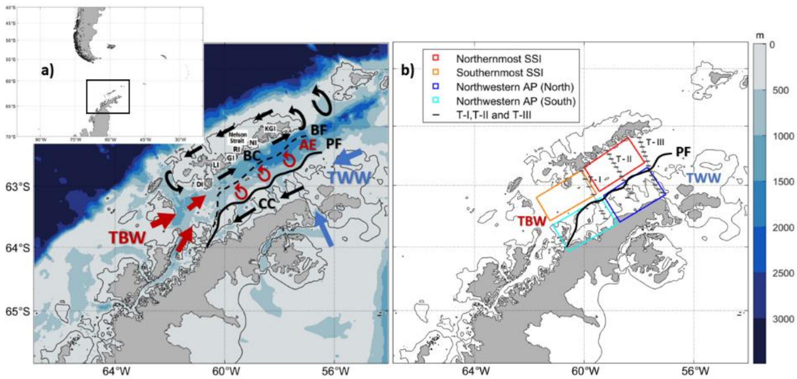

Figure 4.1. (a) Sketch of the circulation in the Bransfield Strait. Abbreviations for the South Shetland Islands (SSI) include DI (Deception Island), LI (Livingston Island), GI (Greenwich Island), RI (Robert Island), NI (Nelson Island) and KGI (King George Island). Abbreviations for major oceanographic features are as follows: AE (anticyclonic eddy), BC (Bransfield Current), BF (Bransfield Front), CC (Antarctic Coastal Current), PF (Peninsula Front), TBW (Transitional Bellingshausen Water) and TWW (Transitional Weddell Water). (b) Map showing cruise transects and boxes selected for dedicated analysis. The transects are from two different oceanographic cruises and include T–I and T–III from CIEMAR (December 1999) and T–II from COUPLING (January 2010). Additionally, four boxes are defined between the SSI and the Antarctic Peninsula (AP): Northernmost SSI (red), Southernmost SSI (orange), Northwestern AP (North) (dark blue) and Northwestern AP (South) (light blue). The 200 m isobath is highlighted with a black contour in both panels.

The BS is connected to the west with the Bellingshausen Sea and to the east with the Scotia and Weddell seas (Figure 4.1). The confluence of water masses of different origin in this area leads to a highly dynamic system where different ocean properties interact. Most previous studies have described the ocean surface dynamics of the BS based on summertime data (Figure 4.1a), when two inflows enter the strait and circulate cyclonically (Grelowski *et al.*, 1986; Hofmann *et al.*, 1996; Zhou *et al.*, 2006; Sangrà *et al.*, 2017). The horizontal and vertical structure of the summertime circulation and hydrography in the BS, when the chlorophyll-a bloom develops, may be summarized as follows.

The western inflow is the Bransfield Current (BC; Niller *et al.*, 1991; Zhou *et al.*, 2002, 2006) which is a coastal jet flowing to the northeast and transporting transitional zonal water with Bellingshausen influence (Transitional Bellingshausen Water, TBW) along the southern slope of the SSI. TBW is typically found within the first 300 m as well-stratified and relatively warm (θ > -0.4ºC) and fresh (<34.45) water (Sangrà *et al.*, 2017), seasonally originating in the Bellingshausen Sea and Gerlache Strait due to summer heating and ice melting (Tokarczyk, 1987; García *et al.*, 1994; Sangrà *et al.*, 2011). The eastern inflow is the Antarctic Coastal Current (CC), which travels southwestward and transports transitional zonal water with Weddell influence (Transitional Weddell Water, TWW) in this area of Antarctica, countering the northern AP coastline. TWW is distinguished by colder (θ < -0.4ºC) and saltier (> 34.45) waters than TBW (Sangrà *et al.*, 2017), coming from the Weddell Sea (Tokarczyk, 1987; García *et al.*, 1994) and being rather homogeneous throughout the water column (Grelowski *et al.*, 1986; Hofmann *et al.*, 1996; García *et al.*, 2002c; Zhou *et al.*, 2002). Between the BC and the CC, there is a street of mesoscale anticyclonic eddies (AEs) with TBW characteristics (Sangrà *et al.*, 2011, 2017). Lastly, the BC recirculates around the islands, transporting TBW as a part of the summertime circulation (Sangrà *et al.*, 2017).

As will be analysed thoroughly in this work, where TBW and TWW encounter each other, a key feature in the biophysical coupling of the chlorophyll-a bloom emerges, the Peninsula Front (PF; García *et al.*, 1994; López *et al.*, 1999). The PF is generally formed at about 20–30 km from the AP slope as a mesoscale shallow structure 10 km wide (Sangrà *et al.*, 2011), confronting TBW and TWW and expanding from the surface down to ~100 m. On the opposite side of the BS, closer to the SSI slope, one finds the subsurface Bransfield Front (BF) between 50 and 400 m (Niller *et al.*, 1991; García *et al.*, 1994; López *et al.*, 1999), where TBW opposes TWW. The latter water mass widens its domain at depth over the whole strait. Generally, the BF extends between 10 and 30 km offshore from the SSI coastlines, being at its widest when approaching King George Island (Veny *et al.*, 2022).

As for the biochemical context, SO waters are characterized by high-nutrient, low-chlorophyll (HNLC) conditions which are equivalent to high concentrations of inorganic macronutrients but low phytoplankton abundance and rates of primary production (Mitchell and Holm-Hansen, 1991; Chisholm and Morel, 1991). Chlorophyll-a (chl-a) concentrations in the SO are frequently around 0.05–1.5 mg m^{-3} (Arrigo *et al.*, 1998; El-Sayed, 2005; Marrari *et al.*, 2006).

However, inshore waters west of the Antarctic Peninsula (wAP) are among the most productive regions of the SO (El-Sayed, 1967; Comiso *et al.*, 1990; Sullivan *et al.*, 1993). Thus, the chl-a concentration in the wAP differs from that found in the SO, with values ranging more extensively from 0.16 to 7.06 mg m^{-3} (Aracena *et al.*, 2018). Yet, Hewes *et al.* (2009) reported that concentrations in this region are generally not higher than 3 mg m^{-3} based on satellite and *in situ* data. Previous studies, based mainly on summertime data (a few during late spring), have also characterized the spatial distribution of chl-a in the BS. The distribution was described as patchy and related to the spatial domain of each characteristic water mass (Basterretxea and Arístegui,

1999) and the upper-mixed-layer (UML) depth, which reflects vertical stability (Lipski and Rakusa-Suszczewski, 1990; Hewes *et al.*, 2009). Then, chl-a was found to be inversely correlated with UML depth and positively correlated with temperature; i.e. concentrations reach their maxima when UML depth is shallow, temperature is relatively high and surface waters are iron-replete (Hewes *et al.*, 2009). More recently, García-Muñoz *et al.* (2013) reported that the highest phytoplankton concentrations along a cross-strait central transect in the BS were correlated with the relatively warm and stratified TBW. Nanophytoplankton (2–20 μm) was found to be predominant throughout the study area, which was dominated by small diatoms. However, haptophyte distribution co-varied with small diatoms and also appeared in well mixed TWW. As for diatoms, García-Muñoz *et al.* (2013) also identified a shift from smaller to larger diatoms when closer to the AP. Sharply, cryptophytes were restricted to the stratified TBW. These authors concluded, for the first time in the literature, that phytoplankton assemblages around the SSI were strongly connected with the Bransfield current system. This is the seed of our hypothesis: the horizontal extent of the surface signal of chl-a bloom in the BS may vary monthly from spring to summer (months of bloom development) according to the spatial distribution of the PF, through which TBW and TWW interact and embed different phytoplankton assemblages. This being confirmed, one could advocate for long-term monitoring of the biophysical coupling between the surface chl-a bloom and the PF using remotely sensed observations of chl-a and sea surface temperature (SST).

Nevertheless, the chl-a distribution in high latitudes has also been reported to be coupled to other biophysical factors such as sea ice formation and atmospheric forcing. It is known that the seasonal sea ice extent and its timing are likewise determining factors for chl-a development (Garibotti *et al.*, 2003; Smith *et al.*, 2008). Furthermore, sea ice conditions are influenced by atmospheric forcing such as the regional wind stress magnitude and direction, which vary from year to year (Smith *et al.*, 2008). In this manner, wind alterations significantly affect the sea ice concentration around West Antarctica (Holland and Kwok, 2012; Eayrs *et al.*, 2019), although there are also seasonal and regional variations in the response (Kusahara *et al.*, 2019).

Given the above scenario, one must acknowledge that chl-a concentrations are not independently controlled by a single factor and their temporal variations are complex, influenced by seasonal, intra- and interannual processes (Siegel *et al.*, 2002; Stenseth *et al.*, 2003); e.g. sea ice–ocean interactions may even evolve differently from one season to the next (Stammerjohn *et al.*, 2012; Holland, 2014).

In this work, we provide a comprehensive description of the seasonal variations in chl-a concentrations in the BS, accounting for the biophysical coupling supporting their development. We hypothesize that this biophysical coupling is strongly conditioned by the spatiotemporal variability in the PF, as has been already argued.

The structure of this paper is as follows. In Section 4.2, we describe the data and methods. In Section 4.3, we present and discuss the results distributed in four subsections. In Section 4.3.1, we set our hypothesis by analysing observational data from two oceanographic cruises: CIEMAR (December 1999) and COUPLING (January 2010). In Section 4.3.2, we construct satellite-based climatologies and examine the seasonally varying horizontal distribution of SST, sea ice coverage (SIC), chl-a concentrations, wind stress and Ekman pumping. In Section 4.3.3, we present the monthly evolution of the latter variables, along with air temperature, in order to characterize the spatiotemporal variability in the bloom according to four distinct regions (Figure 4.1b), which will be accounted for in the text. In Section 4.3.4, we address a review of works investigating the phytoplankton assemblage in the BS, bearing in mind the biophysical coupling previously described, in order to provide further insights based on state-of-the-art knowledge. Lastly, in Section 4.3.5, we construct satellite-based monthly climatologies of SST and chl-a along the same transects sampled during the CIEMAR and COUPLING cruises to present a climatological context for our hypothesis, through which the spatial distribution of the chl-a blooms in the BS varies according to the PF (monitored via SST), which contours the hydrographic area for TBW and TWW and hosts different phytoplankton assemblages. Section 4.4 presents a summary of the main conclusions. Finally, in Appendices B and C, we analyse the goodness of fit of three available SST products and study the frontal probability of the Peninsula Front, respectively.

4.2 Data and methods

In situ observations and remotely sensed measurements are detailed in the following, separately, for clarity. Seasons are defined following Zhang *et al*. (2011) and Dotto *et al*. (2021) as summer (January–February–March), autumn (April–May–June), winter (July–August–September) and spring (October–November–December).

4.2.1 *In situ* observations: Antarctic cruises

The data inspiring the hypothesis that we address in this work, i.e. the spatial distribution of the chl-a bloom in the BS as strongly conditioned by the PF, rely to a great extent on conductivity–temperature–depth (CTD) and fluorescence measurements collected from two interdisciplinary cruises: CIEMAR and COUPLING. The fluorescence measurements were collected with an ECO fluorometer, which measures fluorescence from chl-a, fDOM (fluorescent dissolved organic matter), uranine, rhodamine, and phycocyanin and phycoerythrin. In this work, we analyse the fluorescence from chl-a (Hernández-León *et al.*, 2013; Sangrà *et al.*, 2014).

On the one hand, the CIEMAR cruise was conducted in December 1999 (Corzo *et al.*, 2005; Primo and Vázquez, 2007; Sangrà *et al.*, 2011), and two transects covered the region from Livingston Island and King George Island towards the northern tip of the AP. On the other hand, the COUPLING cruise was conducted in January 2010 (Hernández-León *et al.*, 2013; Sangrà *et al.*, 2014, 2017), and a transect covered the region from the Nelson Strait to the AP tip. Both cruises were carried out on board the R/V *Hespérides*. For further details about the CTD station map of both cruises, the reader is referred to Sangrà *et al.* (2011, 2017).

Additionally, *in situ* surface and subsurface (10 m depth) temperature measurements were downloaded from PANGAEA (https://www.pangaea.de/, last access: 9 March 2022) and the World Ocean Database (WOD; https://www.ncei.noaa.gov/products/world-ocean-database, last access: 25 February 2022) in order to assess the goodness of available open-access remotely sensed products of SST and support the choice of the product providing the best fit. In Table B1 of the Appendix B, a summary of the cruises and corresponding dates for the CTD measurements used is presented.

4.2.2 Remotely sensed products: sea surface temperature and sea ice coverage

We use satellite data of SST and SIC from the Operational Sea Surface Temperature and Sea Ice Analysis (OSTIA; Good *et al.*, 2020) downloaded from the Copernicus Marine Environment Monitoring Service (CMEMS; https://marine.copernicus.eu/, last access: 12 March 2022) and developed by the United Kingdom Met Office. The motivation behind this choice is supported by a quantitative intercomparison between available SST open-access products and *in situ* temperature measurements (see this analysis in Appendix B).

OSTIA provides the SST free of diurnal variability and the sea ice concentration. It is a reprocessed dataset with a high grid resolution of 0.05°, which accounts for both *in situ* and satellite data and presents a processing level L4. This work analyses OSTIA data from 1998 to 2018.

4.2.3 Remotely sensed products: chlorophyll-a

We compute monthly climatologies of surface chl-a concentrations based on multi-sensors and algorithms. The product name is OCEANCOLOUR_GLO_BGC_L4_MY_009_104, obtained from CMEMS (https://marine.copernicus.eu/, last access: 16 February 2023). The chl-a data have a spatial resolution of 4 km, a temporal range from September 1997 to the present and a processing level L4. This work analyses concentrations from 1998 to 2018.

4.2.4 Remotely sensed products: wind and air temperature

We use the monthly averaged reanalysis of air temperature at 2 m and wind components at 10 m from ERA5 (Hersbach *et al.*, 2020), which have a horizontal resolution of 0.25° over the period 1940 to the present. From the wind components, we calculate the wind stress and Ekman pumping.

We calculate the wind stress (τ) and wind stress zonal (τ_x) and meridional (τ_y) components following Equations (4.1)-(4.3) (Patel, 2023):

$$\tau = \rho \cdot U_{10}^2 \cdot C_D \tag{4.1}$$

$$\tau_x = \rho \cdot U_{10} \cdot u \cdot C_D \tag{4.2}$$

$$\tau_y = \rho \cdot U_{10} \cdot v \cdot C_D \tag{4.3}$$

where ρ is the air density (1.2 kg m^{-3}); $U_{10} = \sqrt{u^2 + v^2}$ is the absolute value of the wind speed at 10 m above the surface (u and v are the eastward and northward wind speed components, respectively); x and y are the eastward and northward spatial coordinates; and, C_D is the drag coefficient, which is a function of wind speed, U_{10}. The equations used for wind stress computation are based on the Gill (1982) formula and a non-linear C_D based on Large and Pond (1981), modified for low wind speeds (Trenberth *et al.*, 1990). We note that the mean C_D we obtained for our climatological maps in the BS is 1.4x10^{-3} ± 0.16x10^{-3}, analogous to the values reported by Kara *et al.* (2007) over the SO.

We also compute the Ekman vertical velocity (Equation 4.4) as follows:

$$w_E = \frac{1}{\rho_0}\, curl\left(\frac{\tau}{f}\right) \tag{4.4}$$

where ρ_0 is the water density (1025 kg m^{-3}) and $f = 2\Omega sin\varphi$ is the Coriolis frequency (Ω is the Earth rotation rate, 7.2921x10^{-5} rad s^{-1}, and φ is the latitude). Positive (negative) w_E values indicate upward (downward) velocities leading to upwelling (downwelling).

4.3 Results and discussion

In this section we assess the major physical drivers potentially conditioning the vertical and horizontal structure of the chl-a bloom in the BS. To this aim, in Section 4.3.1 we analyse the vertical and horizontal structure of two chl-a blooms in the BS based on hydrographic measurements from two cruises (1999 and 2010) along three cross-strait transects (T- I, T-II, T-III). In Section 4.3.2 we analyse the seasonal variations in the horizontal structure of the chl-a bloom and the PF from a climatological perspective based on remotely sensed observations over a 21-year period (1998–2018): SST, SIC, wind stress and Ekman pumping. Next, in Section 4.3.3, we examine in detail the monthly climatologies of selected boxes of study in the BS (adding air temperature to the analysis). In Section 4.3.4, we provide a summary review of the research on the phytoplankton assemblage in the BS. Lastly, in Section 4.3.5 we construct satellite-based monthly climatologies of SST and chl-a along the same locations as the transects T–I, T–II and T–III to provide a statistically robust (i.e. climatological) context to our hypothesis, through which the chl-a bloom extent varies according to the PF.

4.3.1 Vertical and horizontal structure along CIEMAR and COUPLING transects

We present the vertical structure of temperature, salinity, density and fluorescence in the BS (Figures 4.2, 4.3 and 4.4) based on data collected during the multidisciplinary CIEMAR and COUPLING cruises in late spring 1999 and early summertime 2010, respectively. The physical oceanographic aspects from these cruises were first presented in Sangrà *et al*. (2011, 2017).

Previous studies based on these measurements are in line with biophysical phenomena focused, among other aspects, on turbulence as a driver for phytoplankton distribution as well as on mesoscale physical features as key players in determining phytoplankton assemblages (García-Muñoz *et al*., 2013; Macías *et al*., 2013; Sangrà *et al*., 2014). Following COUPLING cruise measurements, García-Muñoz *et al*. (2013) concluded that phytoplankton assemblages around the SSI were strongly connected with the Bransfield current system. Furthermore, it was suggested that, considering the recurrence of the Bransfield current system during the austral summer, the observed distribution of phytoplankton, which responded to this current system, should also be a quasi-permanent feature (García-Muñoz *et al.*, 2013). In the following, we combine the measurements from the two cruises for the first time to address this hypothesis, where we add and highlight that the key player appears to be the cross-strait gradient marked at the surface by the PF and that this may enable the long-term monitoring of the biophysical coupling between the surface chl-a bloom and the PF based on satellite measurements.

For clarity, we name the three transects of study T–I, T–II and T–III moving from west to east. Thus, transect T–I (Figure 4.2) and T–III (Figure 4.4) correspond to CIEMAR and present novel measurements of fluorescence (not previously published), while transect T–II (Figure 4.3), located between T–I and T–III, corresponds to COUPLING. The three transects originate over the shelf of the SSI and extend towards the AP, running nearly perpendicular to the main axis of the strait. Notably, measurements from both sea trials agree well in showing a coherent vertical and horizontal structure of hydrography and fluorescence. In Figures 4.2–4.4, two panels are always dedicated to showing the temperature–salinity (*T–S*) diagram and the station map to help the reader in following the ocean property descriptions.

Starting with T–I (Figure 4.2), this originates to the south of Livingston Island and extends towards the AP. Along T–I, temperatures are above 0ºC in the upper 40 m for its full extent (Figure 4.2a), being relatively high in the proximity of the SSI at a distance of 0–20 km and close to the AP, where they reach near-surface values and exceed 0.6 and 0.4ºC, respectively. On the other hand, salinity is remarkably fresher and lighter near the SSI ($S < 34$ and $\sigma_\theta \lesssim 27.3$ kg m^{-3}), as opposed to saltier and denser waters towards the AP ($S >$ 34.3 and σ_θ ~27.6 kg m^{-3}; Figure 4.2b and c, respectively). Fluorescence levels exceeding 2–3 (Figure 4.2d) peak in the warmest (> 0.2ºC) and lightest surface waters (upper 50 m) near the SSI (stations B1–B2) and near the AP (stations B5–

B7). The isopycnal of 27.64 kg m^{-3} is highlighted in black in all vertical sections as a reference to the water mass boundary between TBW (σ_θ <27.64 kg m^{-3}) and TWW (σ_θ >27.64 kg m^{-3}; Sangrà *et al.*, 2011, 2017). These observations indicate the presence of relatively warm TBW flowing near the surface to the south of Livingston Island. Coastal signals of Bransfield Strait Shelf Water (BS Shelf Water), characterized by lower salinity values (Zhou *et al.*, 2006; Polukhin *et al.*, 2021), were also detected. In addition, relatively cold TWW flows closer to the AP at deeper levels (> 60 m depth), where fluorescence sharply diminishes (< 0.5) along the entire transect (Figure 4.2d). The PF is not visible along T–I given the basin-wide extent of TBW at surface, which prevents shoaling of TWW.

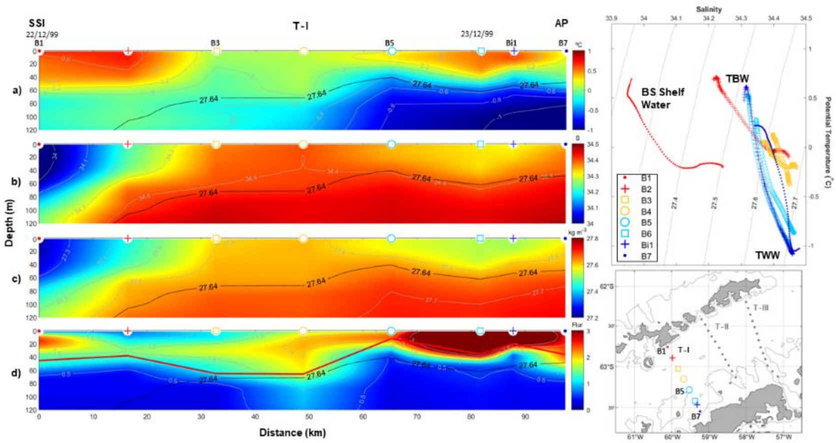

Figure 4.2. Vertical sections of ocean properties along transect T–I surveyed during the CIEMAR cruise (December 1999), running from Livingston Island to the Antarctic Peninsula. (a) Potential temperature, (b) salinity, (c) potential density and (d) fluorescence are shown on the left-hand-side panels. The solid black line represents the isopycnal of 27.64 kg m^{-3}, used as a reference to distinguish between transitional zonal water with Bellingshausen influence (TBW) and transitional zonal water with Weddell influence (TWW; Sangrà *et al.*, 2017). The solid red line in (d) shows the upper-mixed-layer depth computed following Holte and Talley (2009). The top right-hand-side panel displays a temperature-salinity diagram to highlight water masses: Bransfield Strait (BS) Shelf Water, TBW and TWW. Different marks and colours are displayed to represent data at each station. The bottom right-hand-side panel shows a map depicting the stations of the transect T–I.

T–II (Figure 4.3) originates to the south of the Nelson Strait and extends towards the AP. Largely, along T–II, TBW is visible as warmer (θ > -0.4ºC) and fresher (<34.45) than TWW (Sangrà *et al.*, 2017). The subsurface signal of TWW extends towards the SSI, confronting TBW between 60–120 m depth at around stations 2–3, where they form the BF (Sangrà *et al.*, 2011). Subsequently, the high-fluorescence patch (>1) extends within the warmest and freshest surface layers (Figure 4.3d) from the surface down to 60 m depth at its deepest, contouring the isotherm of 0.2 from the SSI until stations 9–10. At this location, the 0.2ºC isotherm reaches the surface, temperature decreases rapidly towards the AP (< -0.6ºC; Figure 4.3a), and salinity and density increase (> 34.3 and > 27.64 kg m^{-3}; Figure 4.3b and c). This gradient forms the PF, where TBW and TWW confront each other close to the AP. Remarkably, near-surface (0–30 m) fluorescence levels decrease below 0.5 (Figure 4.3d) on the TWW side of the PF.

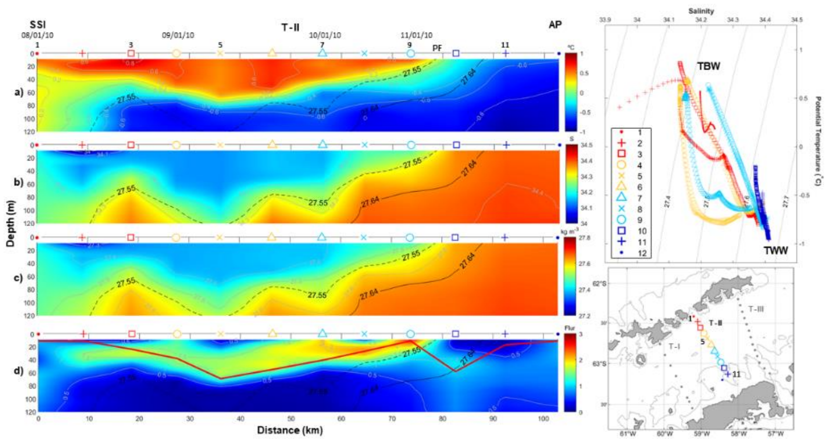

Figure 4.3. The same as in Figure 4.2 but for T–II, surveyed during the COUPLING cruise (January 2010) and running from the Nelson Strait to the Antarctic Peninsula. Additionally, the dashed black line represents the isopycnal of 27.55 kg m^{-3}, which is used as a reference more adjusted to our dataset to distinguish between TBW and TWW.

Lastly, T–III (Figure 4.4) originates to the south of King George Island and extends towards the AP. Generally, we observe an analogous vertical structure to that described for T–II, suggesting that a horizontal coherence exists between transects, especially when accounting for the fact that differences with T–I are due to the latter being at a farther distance from the Weddell Sea and, hence, presenting a weaker signal of TWW at the surface. As observed in Figures 4.2 and 4.3, the chl-a bloom suggested by high fluorescence values (> 1) is again embedded within the pool of TBW closer to the SSI, where waters are relatively warm and fresh as compared to TWW close to the AP. Moreover, the PF (stations T10–T11) appears to delimit the surface's easternmost reach of the patch with the highest fluorescence. However, we must also note that, between the PF and the AP, a less prominent and coherent patch of values higher than the baseline exists down to nearly 120 m depth, in both T–II and T–III (fluorescence >0.5 and >1, respectively).

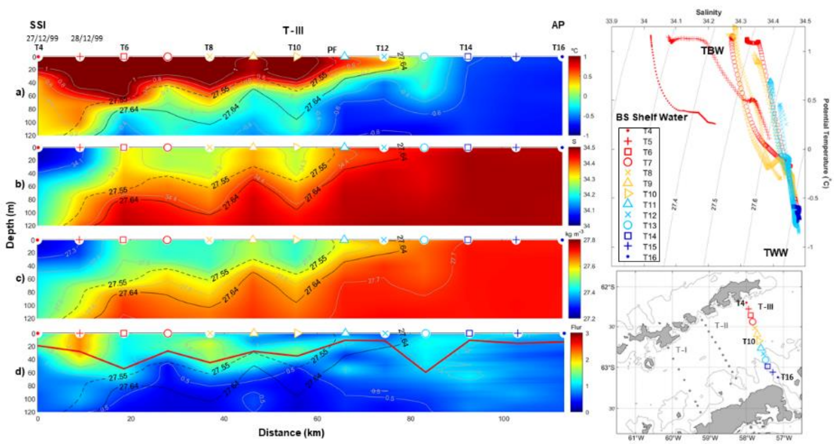

Figure 4.4. The same as in Figure 4.2 but for T–III, surveyed during the CIEMAR cruise (December 1999) and running from King George Island to the Antarctic Peninsula. Additionally, the dashed black line represents the isopycnal of 27.55 kg m^{3}, which is used as a reference more adjusted to our dataset to distinguish between TBW and TWW.

Remarkably, two other studies (Basterretxea and Arístegui, 1999; Gonçalves-Araujo *et al.*, 2015) have also captured a consistent cross-strait pattern where the highest chl-a concentrations are embedded within the TBW reservoir in the first ~ 60 m of the water column, and the easternmost extent of this signal coincides with the location of the PF, through which TBW and TWW interact. In both cases, in spite of the sharp decrease in chl-a across the PF, chl-a concentrations were not low in the TWW reservoir and, in fact, relatively high although occupying a wider depth range (0–100 m). Their vertical sections were constructed from ship-based measurements collected along a transect parallel to T–III but farther north, departing from King George Island, in January 1993 and February–March 2009: Figure 6 in Basterretxea and Arístegui (1999) and Figure 3 in Gonçalves-Araujo *et al.* (2015), respectively. This supports the existence of different phytoplankton assemblages occupying different niches according to the dominant water masses.

In all (d) panels from Figures 4.2–4.4, a solid red line is added to indicate UML depth (Holte and Talley, 2009). Roughly, this estimate of the UML depth fits well with the depth of the high-fluorescence patch embedded within the TBW reservoir, which keeps phytoplankton under favourable light conditions, enables a better supply of dissolved iron (Prézelin *et al.*, 2000) and keeps phytoplankton within a depth range with proper conditions for accumulation of phytoplankton biomass (Mukhanov *et al.*, 2021; Mendes *et al.*, 2023). Accordingly, relatively high fluorescence (> 0.5) is accumulated along the entire BS in T–I, where UML depth is relatively shallow (< 60 m), especially at stations B5–B7 (fluorescence above 2 and UML depths of ~ 15 m). The same pattern applies along T–II and T–III, with the high-fluorescence patch embedded within the UML. In T–II, the highest fluorescence (~2) is located near the PF, at station 9, where the lowest UML depths occur (10 m). Similarly, in T–III a fluorescence of 2 is closer to the SSI station 2 where UML depths are around 25 m. Moreover, near the AP, relatively low

UML depths (10 m) are also observed in station T14 jointly with a fluorescence of 1.

Following results in García-Muñoz *et al.* (2013), the fluorescence observations presented here from the COUPLING cruise (T–II in Figure 4.3) can be attributed to different phytoplankton assemblages, as briefly introduced in Section 4.1, namely cryptophytes in the upper 60 m of the TBW reservoir between the BF and the PF and nanophytoplankton along the full transect but at higher abundances for the largest fraction in the TWW reservoir, accounting for the weaker but deeper signal in fluorescence (from the surface down to 100 m). This suggests that the fluorescence signal measured by the ECO fluorometer might be dominated by cryptophytes. Whether this is also the case for the CIEMAR transects (T–I and T–III in Figures 4.2 and 4.4) is a feature we cannot confirm in the absence of a phytoplankton assemblage study for that cruise. However, a decade apart, the fluorescence distribution appears consistent in showing highest and shallower values within the relatively warm and stratified TBW reservoir, and lower but deeper values within the cold and well-mixed TWW reservoir. The stronger signal in fluorescence during CIEMAR could then be attributed to a higher abundance of cryptophytes within the TBW reservoir if we assume that the pattern observed by García-Muñoz *et al.* (2013) is recurrent over time. Recent studies also support this by confirming the preferred niches of cryptophytes in the BS are the relatively warm, less saline and stratified waters of the TBW reservoir, where they also compete with diatoms (Mendes *et al.*, 2013, 2023; Gonçalves-Araujo *et al.*, 2015; Mukhanov *et al.*, 2021; Costa *et al.*, 2023).

Results from the *in situ* measurements collected during the CIEMAR and COUPLING cruises, occurring a decade apart, plus more recent evidence of phytoplankton assemblages following the ocean dynamics of the Bransfield current system jointly further support the basis of our hypothesis:

the biophysical coupling between the spatial distribution of the surface chl-a bloom and the PF in the BS may benefit from long-term monitoring using remotely sensed observations of chl-a and SST.

In the following section, we analyse a set of satellite-based climatologies with the aim to demonstrate that the horizontal variability in the PF (and hence the interaction between TBW and TWW) plays a major role in determining the spatial extent of the patch with the highest surface chl-a bloom in the BS. We complete this analysis by considering the role of several physical drivers which also contribute to setting the niche for phytoplankton assemblage through a biophysical coupling. We expect this joint climatological perspective of the seasonal variations in the chl-a bloom and the PF, unprecedented in the literature, will provide the basis for their long-term monitoring. Counting on a robust long-term phytoplankton monitoring approach will enable a better understanding of the biophysical coupling that sets the baseline of the marine food web in the BS.

4.3.2 Seasonal variations in the chl-a bloom and Peninsula Front coupling

The remotely sensed climatologies of SST, SIC, chl-a and Ekman pumping (along with wind stress) were computed for the period 1998 to 2018 and are presented in Figures 4.5–4.8, respectively.

Regarding the SST (Figure 4.5), the most outstanding feature governing the summer months in the BS is a strong cross-strait gradient, where high temperatures (> 1ºC) spread around the SSI and lower temperatures (<0ºC) appear to enter into the basin from the Weddell Sea, turning around the AP and spreading southwestward along the peninsula shelf. This strong temperature gradient is the surface signal of the PF, where TBW confronts TWW. Previous studies, based on *in situ* summertime data, have used different thresholds for the isotherm characterizing the location of the PF at surface, where TBW and TWW interact: Sangrà *et al*. (2017) used the isotherm of -0.4ºC, while Catalán *et al*. (2008) used the isotherm of 1ºC. The choice of these isotherms is not trivial, and one must identify the isotherm embedding the water body flowing from the Weddell Sea into the BS, thus separating TWW from TBW. Looking at Figure 4.5a, we note that the climatological isotherm characterizing the PF location at the surface during the summer months corresponds to the 0.6ºC isotherm. Through autumn and spring, the PF is also visible although a different isotherm rises as characteristic of this thermal front, being -1.2 and -0.8ºC, respectively. Lastly, during the winter months the surface signal of the PF vanishes, as one could expect, due to the atmospheric forcing prevailing in the homogenization of the upper ocean. Within the strait, surface temperatures are around -1.8ºC ± 0.2ºC. It is worthwhile noting that in Figures 4.3 and 4.4 we used the 0.2 and 0.8ºC isotherms, respectively, reaching the surface to define the location of the PF, and in Figure 4.5 we used a different isotherm. This is not a contradiction. One must keep in mind that the 0.2 and 0.8ºC characteristic isotherms worked well through synoptic transects, which took place in late December and January, while in Figure 4.5a summertime climatological field is examined after time-averaging 3 data months over a period of 21 years. This accounts for the seasonally varying values provided above, which differ from the synoptic values.

To the best of our knowledge, this is the first time that a remotely sensed SST seasonal climatology is shown with a focus on the BS. In Appendix B we present an examination of the goodness of SST satellite measurements against concomitant *in situ* measurements, finding that a high correlation exists between the product we use (OSTIA) and *in situ* measurements (R^2 = 0.849). Also, the summertime field is in agreement with patterns reported in the literature for this season and based on *in situ* hydrographic measurements (Sangrà *et al*., 2011, 2017). Additionally, we used a recently published seasonal climatology of hydrographic properties in the BS based on in situ measurements (Dotto *et al.*, 2021) and produced a figure (not shown) analogous to our Figure 4.5 (with the same contour lines and colour bar). The comparison supports the major features of the seasonal patterns described above. Exceptions occur north of the SSI in autumn and inside the BS in spring, where the abundance of mesoscale features in the climatology based on *in situ* measurements (Dotto *et al.*, 2021) slightly hampers the view of the mean field pattern.

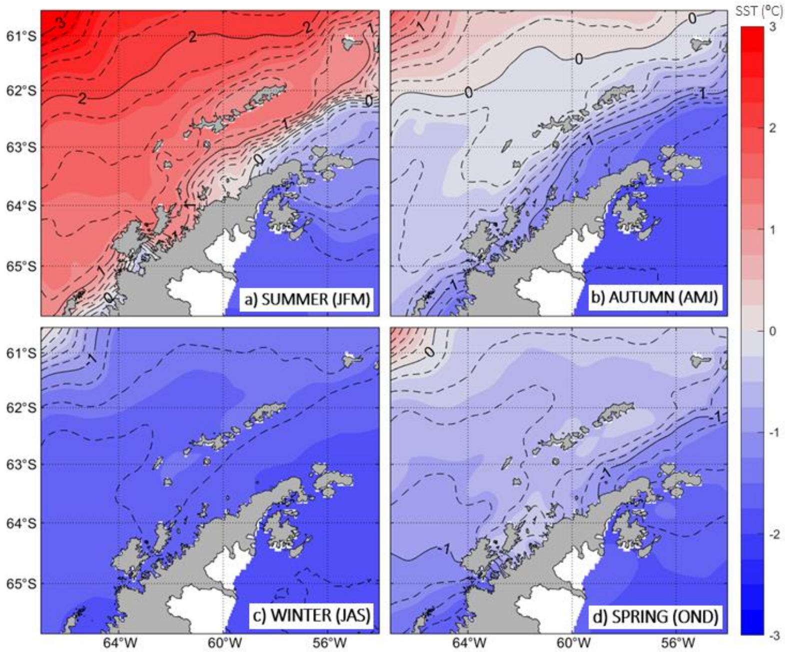

Figure 4.5. Seasonal maps of sea surface temperature (SST; in shades of colours) for (a) summer, (b) autumn, (c) winter and (d) spring. The capital letters between brackets stand for the initial letters of the months. The SST climatologies are averaged from January 1998 to December 2018. The dashed isotherms are plotted at intervals of 0.2ºC, while the solid lines mark each 1ºC interval.

Figure 4.6 shows the seasonal SIC as a percentage of area covered by sea ice. A value of SIC of about 15% is taken as indicative of the presence of sea ice. Thus, during the summer and spring months, the BS is generally free of sea ice with SIC <15%. Through autumn, the atmospheric forcing starts leading the development of the SIC in the BS, which extends firstly over the colder waters of the Weddell Sea intrusion with SIC ranging from 15% to 25% (compare Figures 4.5b and 4.6b). This is in agreement with a recent study developed over the western AP, which addresses the role of subsurface ocean heat in the modulation of the sea ice seasonality and highlights the importance of the upper-ocean variability in setting sea ice concentrations and thickness (Saenz *et al.*, 2023). Towards winter, the SIC is greater than 25% everywhere in the BS (Figure 4.6c), promoted by near-freezing sea surface temperatures of around -1.8ºC ± 0.2ºC (Figure 4.5c).

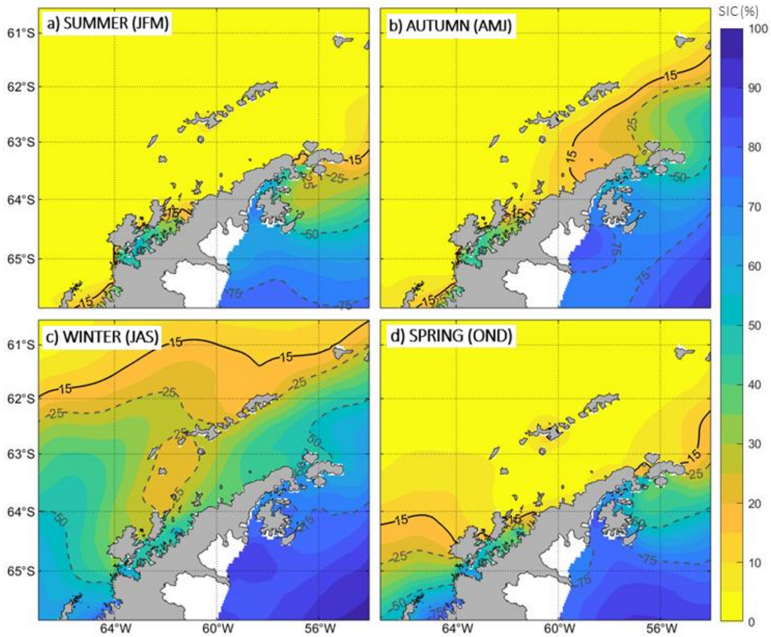

Figure 4.6. The same as Figure 4.5 but for sea ice coverage (SIC). Solid black lines indicate a SIC percentage of 15%, which is the threshold for considering the presence of sea ice significant. Dashed grey lines represent SIC percentages of 25%, 50% and 75%.

Taking into account the fact that the seasonal sea ice retreat is complete from spring to summer in the entire

BS suggests that the larger freshwater inputs reported in the literature over the TBW domain and contributing to the vertical stabilization of the water column might be driven by a warmer oceanic forcing over coastal and glacial areas (Cook *et al.*, 2016) rather than by melting of the open-ocean sea ice.

Following seasonal panels in Figure 4.7, the development of the chl-a bloom in the BS is particularly revealing when using a logarithmic scale, which highlights spatial patterns that are otherwise slightly masked due to the strong signal of chl-a east of the AP in the Weddell Sea. West of the AP, chl-a bloom concentrations have been reported to range normally between 0.5–1 mg m^{-3} (Ducklow *et al.*, 2008; Smith *et al.*, 2008). However, we must note that this threshold varies significantly depending on the study region given that there are areas with naturally either higher or lower phytoplankton concentrations.

Generally speaking, the chl-a bloom in the BS starts developing in spring, reaching its maximum horizontal extent with values above 0.5 mg m^{-3} during the summer months and still presenting patchy regions of high chl-a during autumn (Figure 4.7). We find that in the BS the isoline of 0.5 mg m^{-3} works well as the threshold contouring the chl-a bloom around the SSI, as this appears to embed coherently in space the region with the highest chl-a values during the summer months. Through winter, surface chl-a concentrations drop below 0.25 mg m^{-3} everywhere in the BS except for the region adjacent to the northern shelf of the westernmost SSI (>0.25 mg m^{-3}). We observe that although the BS receives inflows from the Weddell Sea to the east of the AP, the much higher chl-a concentrations present in the Weddell Sea do not extend into the BS. This is in spite of the fact that the waters from the Weddell Sea are continuously propagating around the northern tip of the peninsula and entering the BS. Notably, this feature persists year-round and the chl-a bloom never develops in the climatologies covering at its highest values the entire BS. Differently, at its largest extent, with values higher than 0.5 mg m^{-3} (summer months), the chl-a bloom appears constrained to the domain of TBW sourced from the Bellingshausen Sea, while the presence of TWW marks the boundary where chl-a concentrations drop sharply within the BS. By comparison between Figures 4.5a and 4.7a, it becomes evident that the spatial extent of the surface chl-a bloom surrounding the SSI (chl-a > 0.5 mg m^{-3}) aligns well with the surface signal of the PF in the BS, where TBW and TWW confront each other. To ease visualization of this coupling, the isotherms of 1 and 0.6ºC have been added over the summertime chl-a field (Figure 4.7a).

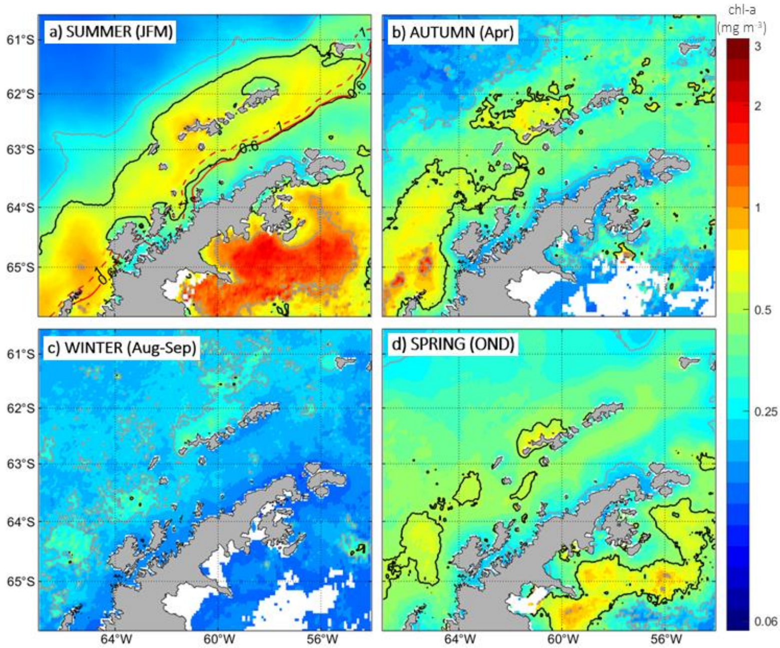

Figure 4.7. The same as Figure 4.5 but for chlorophyll-a (chl-a) concentrations. Solid black lines indicate chl-a concentrations of 0.5 mg m^{-3}, while solid grey lines represent chl-a concentrations of 0.25 and 1 mg m^{-3}. Solid and dashed red lines in (a) indicate 0.6ºC and 1ºC summer isotherms, respectively (see Figure 4.5a). For the autumn season (b), only the mean of April is considered due to the absence of data during other months, which results from the presence of ice cover. Similarly, for the winter season (c), the mean of August and September months are solely considered for the same reason.

This bloom area where chl-a concentrations are higher than 0.5 mg m^{-3} coincides in the cross-strait direction with the chl-a bloom boundaries reported by García-Muñoz *et al.* (2013) for cryptophytes and large nanophytoplankton surrounding the SSI (their Figure 4). On the Drake Passage side, the oceanward extent of their bloom ended at the subsurface Shetland Front (García-Muñoz *et al.*, 2013), embedding TBW over the northern shelf of the SSI and accounting for the recirculation of TBW around the archipelago driven by the Bransfield Current (Sangrà *et al.*, 2017). In Figure 4.5a, the alignment of the subsurface Shetland Front to the north of the SSI is suggested by the isotherm of 1.6ºC, which roughly follows the oceanward extent of the surface chl-a bloom (Figure 4.7a). On the BS side, the chl-a bloom investigated in García-Muñoz *et al.* (2013) also transitioned towards lower values across the PF in agreement with this study (Figures 4.5a and 4.7a) and previous and later works (Basterretxea and Arístegui, 1999; Mendes *et al.*, 2013; Gonçalves-Araujo *et al.*, 2015; Mukhanov *et al.*, 2021). Lastly, we also note the resemblance of our summertime satellite-based climatologies of SST and chl-a (Figures 4.5 and 4.7) with those based on 18 years of summertime hydrographic and chl-a measurements, through which Hewes *et al.* (2009) demonstrate that the distribution of high chl-a around the SSI corresponded to shallow UML depths in iron-rich waters at salinities ~34 (their Figure 4).

In Figure 4.8, the seasonal climatology of the wind forcing acting over the bloom domain is presented following the wind stress field (black vectors) and Ekman pumping (vertical velocity; w_E). The dominant winds in the BS are the westerlies (Vorrath *et al.*, 2020), which flow across the strait with greater basin-wide intensity during winter and spring months. In shades of colours, the Ekman pumping is shown with positive (red) and negative (blue) vertical velocity values, implying that wind stress drives either local upwelling or local downwelling, respectively. Generally, upwelling is observed in the BS throughout the year, with a few spatial and temporal exceptions. Downwelling occurs mostly south of King George Island year-round. During autumn, this downwelling area south of King George Island expands towards the AP more extensively. This feature remains through the winter months, although it is constrained to a smaller extent that does not reach the AP. During winter and spring, the westerlies drive relatively strong upwelling vertical velocities in the BS, especially along the shelf west of the AP.

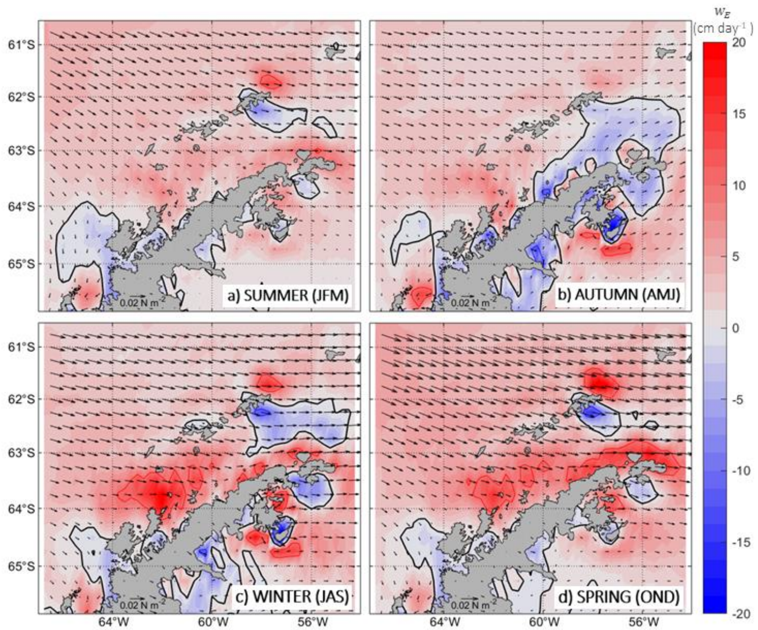

Figure 4.8. The same as Figure 4.5 but for Ekman pumping. Positive (negative) vertical velocities are indicated in shades of red (blue) and represent upwelling (downwelling) processes. Solid black lines refer to zero velocities. Solid red and blue lines represent vertical velocities of 10 and -10 cm d^{-1}, respectively. Black vectors depict the wind stress. The wind stress reference vector is displayed over the southern AP with a value of 0.02 N m^{-2}.

Importantly, during spring and summer (months of chl-a development; Figure 4.7a and d), the westerlies appear slightly stronger along the southern shelf of the SSI (over the domain of TBW) as compared to westerlies acting over the shelf west of the AP (over the domain of TWW). Following this, one could reasonably expect deeper mixed layers over the domain where the wind stress forcing is stronger; however, along the southern shelf of the SSI, winds favour the Bransfield Current transport of TBW via downwelling-favourable Ekman transport while, along the shelf west of the AP, winds exert a moderate counterforcing to the entrance of the Antarctic Coastal Current driving upwelling-favourable Ekman transport. We find that this asymmetry may be contributing to maintaining the two distinct niches across the PF: warmer, less saline and stratified waters transported by the Bransfield Current on the TBW side and colder, saltier and well-mixed waters transported by the Antarctic Coastal Current on the TWW side.

4.3.3 Monthly variations in the chl-a bloom and Peninsula Front coupling

Following results from previous subsections, we note that two areas in the BS are distinctive, not only regarding their ocean dynamics as previously known (Figure 4.1), but also regarding the nature of the chl-a bloom. The first one is where the chl-a bloom spreads with the highest concentrations over the relatively warm and more stratified TBW, flowing northeastward along the southern shelf of the SSI. The second one is the relatively cold and more homogeneous TWW flowing southwestward along the western shelf of the AP.

For further study of the monthly evolution of ocean and atmospheric conditions influencing the development of the surface chl-a bloom over each area, we divided the BS into four boxes of study (Figure 4.1b). These boxes were designed to capture, respectively, the northern and southern domain of the surface chl-a bloom embedded in TBW south of the SSI and northern and southern domain of the surface chl-a bloom embedded in TWW west of the AP. The resulting climatologies of SST, air temperature, SIC, chl-a, along-shore wind stress and Ekman pumping over the period 1998–2018 are presented in Figure 4.9 and reveal several spatiotemporal similarities, and differences, which stand out and provide further insights. To this aim, the wind stress was decomposed into its along-shore ($\tau_{x'}$) and cross-shore ($\tau_{y'}$) components through rotation of the Cartesian components by 36.25° in an anticlockwise sense.

The monthly climatologies of SST and air temperature (Figure 4.9a and b) present a coherent seasonal cycle where warmer (colder) temperatures are found within all the regions for the summer (winter) months. Spatially, SSTs within the boxes south of the SSI are generally warmer than those along the western AP. This is more prominent during the summer months, when cross-strait temperature gradients are higher with differences between boxes at opposite ends of the strait of about 0.6 to 1.4°C (Figure 4.9a). These differences decrease approaching the winter months, when all regions at the surface approach near-freezing temperatures of about -1.8°C from July to August. Evolving through the spring months, temperature differences start to increase again but are not higher than 1°C when comparing boxes along the southern shelf of the SSI and along the shelf of the AP. Because boxes south of the SSI, sourced by TBW, depart from higher temperatures and all regions reach near-freezing temperatures during winter, their seasonal amplitudes are larger (and the slopes are more pronounced) as compared to boxes along the shelf of the western AP, sourced by TWW. Thus, the seasonal amplitude of the SST is more than 1.5 times larger for the southern shelf of the SSI (~3°C) than along the western AP shelf (~1.8°C).

The seasonal amplitude of the air temperature cycle (Figure 4.9b) is larger than that displayed in SST. However, warmer temperatures are once again observed in the boxes situated along the southern shelf of the SSI, where temperatures evolve from 1°C (summer) towards -5 to -6°C (winter), in contrast to the boxes situated along the western

AP shelf, where temperatures evolve from 0ºC (summer) towards -8ºC (winter). As compared to the SST annual cycle, we observe the air temperature is more homogeneous during the summer and spring months (temperature differences among boxes are < 1.25ºC) than during autumn and winter (temperature differences among boxes are > 2.5ºC). This is the reverse pattern to that shown for SST, where more homogeneous temperatures among regions were found through the winter months. The reason behind the more homogeneous pattern in SST during the winter months may be due to seawater approaching near-freezing temperatures, which sets a threshold that homogenizes the ocean surface under an extreme-cooling atmospheric forcing.

The SIC monthly climatology (Figure 4.9c) follows an inverse relationship with SST and air temperature (Figure 4.9a and b), where higher values of SIC are found during the late-autumn, winter and early-spring months and an absence of sea ice is found through late-spring, summer and early-autumn months (< 15% SIC). Through these latter seasons, the sea ice retreat drives melting waters into the environment. This is a key factor in phytoplankton biomass accumulation, since it allows upper-ocean stratification during spring–summer, leading to favourable sunlight conditions for phytoplankton to grow (Ducklow *et al.*, 2013). Then, the SIC peaks in July at about 50% closest to the AP tip and at about 40% farther south along the AP and south of the northernmost SSI. A month later the SIC peaks in August at about 30% south of the southernmost SSI.

Remotely sensed chl-a observations enable the visualization of the monthly evolution from August to April (Figure 4.9d) with a data gap due to sea ice coverage from May to July. Yet, a seasonal cycle is visible with higher chl-a concentrations through the spring and summer months, lower and declining chl-a concentrations through early autumn, and lower and increasing chl-a concentrations through late winter. This latter increasing trend is concomitant with the decrease in SIC, when sea ice starts melting in August (the same month as when SST and air temperature also start increasing). Following the literature, the date of the bloom initiation is determined as the first day at which chlorophyll levels rise to 5% above the climatological median (Siegel *et al.*, 2002) and stay above this value for at least 2 consecutive weeks (Thomalla *et al.*, 2011). This threshold was computed assuming linear interpolation over winter to obtain the climatological median.

Bearing these criteria in mind, our climatologies indicate that the chl-a bloom in the BS starts in mid-October, departing from a baseline for chl-a concentrations of ~0.2 mg m^{-3} in August. From mid-October (early spring) onwards, chl-a concentrations start increasing in the entire BS, although more steeply along the southern shelf of the SSI, and are slightly delayed in the northern box of the western shelf of the AP.

The chl-a peaks through December and February at 0.68 mg m^{-3} south of the southernmost SSI and in February at 0.63 mg m^{-3} south of the northernmost SSI (Figure 4.9d). Along the shelf of the western AP, chl-a peaks to the south in December at 0.43 mg m^{-3} and, 1 month later, to the north in January at 0.37 mg m^{-3}. Generally, although standard deviations are large and overlap each other's cycles, these monthly climatologies suggest a northward development for the chl-a peaks with about 1–2 months of delay.

The pattern described above for the four boxes of study supports the likely existence of two different chl-a blooms that develop simultaneously but are of a different *nature* (i.e. phytoplankton assemblage) in the BS, as suggested by their different intensities and timings (month of initiation and rate of increase). This is in agreement with former results in a series of studies which reported that cryptophytes compete in the BS primarily with diatoms and other nanophytoplankton groups (Mura *et al.*, 1995; García-Muñoz *et al.*, 2013; Mendes *et al.*, 2013, 2023; Gonçalves-

Araujo *et al.*, 2015; Mukhanov *et al.*, 2021; Costa *et al.*, 2023), following strategies to adapt better to water mass distribution in the basin, which ultimately controls the time and space variability in BS phytoplankton communities.

Only two former studies have reported monthly climatologies of the surface chl-a bloom in the BS; however, neither of them framed the boxes of study such that the two blooms were simultaneously, and distinctively, captured. In the first study, Gonçalves-Araujo *et al.* (2015) placed a rectangular box embedding both margins of the BS at the same time, with no distinction between the TBW and TWW domains. The resulting time series (2002–2010) displays a strong interannual variability, with summertime values ranging from ~ 1.1 mg m^{-3} (2006) to 0.37 mg m^{-3} (2003; their Figure 9). In the second study, La *et al.* (2019) placed a slanted rectangular box parallel to the SSI coastline and similar to our two boxes south of the SSI, but in their case it extended towards Elephant Island. The resulting monthly climatology of the chl-a over the period 2002–2014 (12-year mean) displays the cycle from October to April. The chl-a bloom then develops from baseline concentrations below 0.2 mg m^{-3} in October to peak concentrations ranging from ~1.75–1.95 mg m^{-3} (their Figure 2) through February to March. We attribute the higher climatological values in La *et al.* (2019), occurring about 1 month later than in our boxes along the SSI, to the different choice of the study area. In their case the northward extension of the box may be including dynamics out of the BS, from the confluence zone with the Weddell Sea. Also, the latter peak in time for this extended region is in agreement with our results in Figure 4.9d, which suggests the maxima in chl-a develop later as one moves northward along the BS.

Finally, the along-shore wind stress (Figure 4.9e) displays year-round downwelling-favourable winds along the southern shelf of the SSI and upwelling-favourable winds along the shelf of the western AP. In all cases, a quarterly cycle stands out with maximum values (in descending order) in September, December, February and May (i.e. winter, spring, summer and autumn). A similar cycle is found along the shelf of the western AP for the Ekman pumping (Figure 4.9f), where vertical velocities are upwelling favourable (positive) year-round with a quarterly cycle (same maximum time variability). Along the southern shelf of the SSI, vertical velocities are also upwelling favourable (positive) year-round but less intense and more homogeneous through the seasons. Peak vertical velocities are 20, 17.5 and 5 cm d^{-1} for boxes along the shelf of the western AP, south of the southernmost SSI and south of the northernmost SSI, respectively.

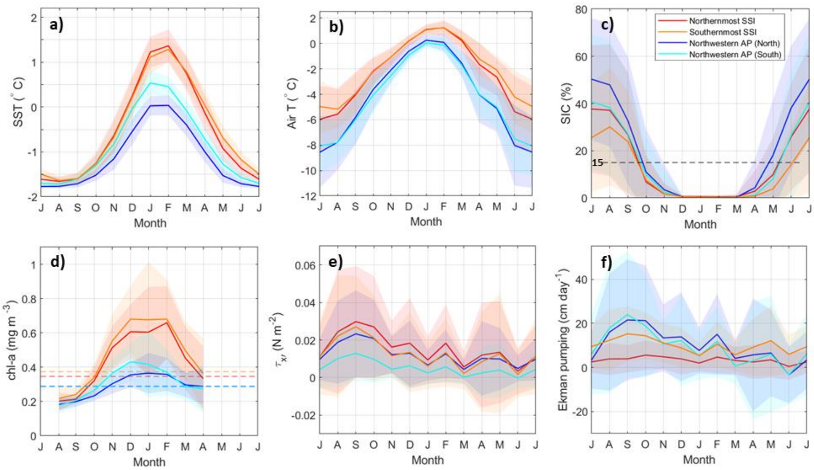

Figure 4.9. Monthly climatology over the period 1998 to 2018 of (a) sea surface temperature (SST), (b) air temperature, (c) sea ice coverage (SIC), (d) chlorophyll-a (chl-a) concentration, (e) along-shore wind stress and (f) Ekman pumping (vertical velocity) for each study box, as delimited in Figure 4.1b. The horizontal dashed line in (c) indicates the threshold (15%) to consider significant the presence of sea ice, while horizontal dashed lines in (d) indicate the threshold set to identify the initiation of the bloom following Siegel *et al.* (2002) and Thomalla *et al.* (2011). The mean monthly values are represented by solid lines, while the corresponding standard deviation is shown in coloured shades.

4.3.4 Spring-summertime phytoplankton assemblages of the chl-a bloom: historical observations

Through the previous section, we have learned that a proper design of study boxes aligned with the climatological summertime position of the PF enables the identification of two distinct chl-a blooms in the BS based on satellite measurements according to two water mass scenarios: TBW and TWW. In this section, we review more than 3 decades of previous studies and indicate their main findings in Table 4.1 so that we can discuss them thoroughly and identify common patterns observed in the past.

In summary, existing observations listed in Table 4.1 support the claim that the phytoplankton community in the BS responds to a variety of factors which may vary from year to year, thus introducing high interannual variability into the phytoplankton assemblage. The factors primarily driving the nature of the chl-a bloom are (1) the vertical stability of the water column; (2) the depth of the UML, which influences the penetration of light into the depth range where biomass may accumulate near the surface; (3) the existence of sea ice retreat, supplying relatively cold freshwater to the environment; and (4) the grazing pressure of herbivorous zooplankton. Berdalet *et al.* (1997) already accounted for these four factors and reported that the combination of them appears to play a major role in the development of, accumulation of and spatial variability in microplankton biomass. After reviewing the most recent studies, we confirm this statement still holds in water and also applies to at least the nanophytoplankton size (there is a scarcity of works investigating picophytoplankton along cross-strait transects in the BS, so we cannot extend the statement robustly to this phytoplankton size). Interestingly, these physical factors may also condition the phytoplankton succession through a given bloom season, and, thus, small cells appear to dominate the phytoplankton community structure during spring as large cells develop to form blooms in summer months (Petrou *et al.*, 2016).

In this context, it is worthwhile highlighting the results from two studies employing multi-year datasets of *in situ* observations of phytoplankton assemblage in the BS through four (Gonçalves-Araujo *et al.*, 2015) and nine (Mendes *et al.*, 2023) different bloom seasons.

On the one hand, in the first study, Gonçalves-Araujo *et al.* (2015) investigated microplankton (20–200 µm) and nanoplankton (2–20 µm) during the summertime periods of 2003, 2004, 2008 and 2009, identifying three main taxonomic groups within the study area: diatoms, flagellates and cryptophytes. From year to year, the surface distribution of phytoplankton size was dominated by nanoplankton in 2003, 2004 and 2008 (> 80% of the total chl-a) with no clear cross-strait gradient. Differently, in 2009 the surface distribution of chl-a presented two distinct domains: (1) in the TBW pool, a mixed community of microplankton and nanoplankton at high (~50%-70%) and low (~30%-50%) percentages of the total chl-a and (2) in the TWW pool, a reversed mixed community of nanoplankton and microplankton at high (~80%) and low (~20%) percentages of the total chl-a. Regarding the taxonomic groups, Gonçalves-Araujo *et al.* (2015) found that interannual variability in species composition resulted from an alternation between diatom-dominated and flagellate-dominated assemblages: 2003 and 2004 were dominated by cryptophytes nearly everywhere in the BS, 2008 by flagellates, and 2009 by a mixture of diatoms close to the SSI and flagellates close to the AP.

Interestingly, in the second study, Mendes *et al.* (2023) investigated a subsequent period of time (2008–2018) based on measurements from nine different years (2011 and 2012 are absent) and demonstrated a strong coupling between biomass accumulation of cryptophytes, summer upper-ocean stability and the mixed layer. For 2008–2018, Mendes *et al.* (2023) reported that cryptophytes present a competitive advantage in environments with significant light level fluctuations, normally found in confined stratified upper layers, and supported that observational finding with laboratory experiments where cryptophytes revealed a high flexibility to grow in different light conditions driven by a fast photo-regulating response. These results provided the basis for understanding why the environmental conditions promoted the success of cryptophytes in coastal regions, particularly in shallower mixed layers associated with lower diatom biomass, and highlighted a distinct competition or niche separation between diatoms and cryptophytes. Regarding long-term variability, Mendes *et al.* (2023) concluded that cryptophytes are gradually outgrowing diatoms along with a decreased size spectrum of the phytoplankton community. This is in agreement with recent results indicating that the increasing meltwater input in the BS can potentially increase the spatial and temporal extent of cryptophytes (Mukhanov *et al.*, 2021), which benefit from the higher stabilization of the water column driven by freshwater input.

This reported shift towards a higher abundance of cryptophytes over diatoms is not trivial and, if it persists in time, will eventually impact the biogeochemical cycling in Antarctic coastal waters due to a shift in trophic processes (Mukhanov *et al.*, 2021). The latter work poses the scenario as follows. The replacement of large diatoms with small cryptophytes favours consumers like salps over Antarctic krill. Salps, a food competitor of Antarctic krill, can feed on a wide range of taxonomic and size compositions of phytoplankton prey. Thus, salps present a much lower feeding selectivity (Haberman *et al.*, 2003) than Antarctic krill, which present positive selectivity for diatoms (large prey) and avoid cryptophytes (smaller prey) when feeding on complex prey mixture (Haberman *et al.*, 2003). The shift towards an increasing role of cryptophytes in BS waters would then lead to constraints in food supply for krill, strengthening the abundance of its competitor. This would threaten not only Antarctic krill populations, but also higher consumers, including penguins, seals and whales, which feed on krill (Loeb *et al.*, 1997).

Reference	Methodology	PFTs in TBW	PFTs in TWW	PFTs in the Bransfield Strait	Date
Mura *et al.* (1995)	Fluorometric method, microscopy analysis	Highest relative contribution to community biomass by eukaryotic picoplankton and DTs	Highest relative contribution to community biomass by eukaryotic picoplankton and DTs	Highest abundance across the PF attributed to CPs	1993 (summer)
Berdalet *et al.* (1997)	Fluorometric and biochemical methods to determine microplankton biomass	Highest values of MP biomass indicators (chl *a*, ATP and protein) found in ice-melting waters and TBW	Lowest values of MP biomass indicators (chl *a*, ATP and protein) found in TWW	The degree of stabilization of the water column, the depth of the UML and the grazing pressure of herbivorous zooplankton, playing a major role in the development of, accumulation of and spatial variability in MP biomass	January 1994 (summer)
García-Muñoz *et al.* (2013)	Flow cytometry, FlowCAM, HPLC/CHEMTAX pigment analysis	Highest abundance of CPs and relatively high abundance of NP (large size)	Higher abundance of NP (large size) and lower abundance of NP (small size)	High abundance of NP (medium size) across the PF	January 2010 (summer)
Mendes *et al.* (2013)	HPLC, CHEMTAX, microscopy analysis	—	—	Dominance of DTs in deeper UML, higher salinity and warmer SST	2008-2009 (late summer)
	HPLC, CHEMTAX, microscopy analysis	—	—	Dominance of CPs in shallower UML, less salinity and colder SST (cold summer with late ice retreat); low diatom biomass in the presence of high nutrient concentrations (particularly silicate) and low chl *a*	2010 (late summer)
Gonçalves-Araujo *et al.* (2015)	Either fluorometric or spectrofluorometric method, microscopy analysis	Dominance of microplanktonic DTs associated with higher chl *a* in shallower UML	Dominance of nanoplanktonic flagellates (CPs, HPs) associated with lower chl *a*in deeper UML	Interannual variability in chl-*a* bloom governed by alternation between diatom-dominated and flagellate-dominated assemblages	2003, 2004, 2008, 2009 (summer)
Mukhanov *et al.* (2021)	Flow cytometry, fluorescence	Presence of CPs (9 µm) and other NP (<3 µm); highest CP abundance and biomass found in the photic layer around the jet of the Bransfield Current	CPs scarce or undetectable	—	January 2020 (summer)
Costa *et al.* (2023)	HPLC, CHEMTAX, microscopy analysis	—	—	Equivalent proportion and abundance of smaller nanoflagellates (CPs, DNs, *Phaeocystis antarctica* and green flagellates) and centric and pennate DTs; CPs prefer low salinities, centric DTs prefer higher salinities (>34), and DNs and centric DTs prefer deeper UML	November 2013-2014 and 2014-2015 (spring)
	HPLC, CHEMTAX, microscopy analysis	—	—	Low diatom biomass accumulation; higher proportion of CPs, DNs and/or pennate DTs with background presence of mixed flagellates; CPs and pennate DTs prefer shallow UML, but CPs occupy colder waters than pennate DTs	2013-2014, 2014-2015, (spring-summer)
	HPLC, CHEMTAX, microscopy analysis	—	—	High diatom biomass accumulation dominated by centric DTs	2015-2016, (spring-summer)
Mendes *et al.* (2023)	HPLC, CHEMTAX, SEM, DNA sequencing, phylogenetic interference	—	—	CPs gradually outgrowing DTs along with a decreased size spectrum of the phytoplankton community	2008-2018 (summer)

Table 4.1. Historical observations investigating the chlorophyll-a bloom in the Bransfield Strait and reporting a description of the phytoplankton assemblage either by water mass domain (TBW or TWW) or without distinction. We must note that in none of the studies is the full spectrum of phytoplankton functional types (PFTs)

covered, and so this review attempts to provide a general overview of the existing knowledge. Abbreviations for PFTs sizes are as follows: microphytoplankton (MP; 20-200 μm), nanophytoplankton (NP; 2-20 μm) and picophytoplankton (PP; 0.2-2 μm). Other abbreviations for PFTs are diatoms (DTs), cryptophytes (CPs), haptophytes (HPs) and dinoflagellates (DNs). Lastly, abbreviations for methodology are high-performance liquid chromatography (HPLC), chemical taxonomy (CHEMTAX) software v1.95 (Mackey *et al.*, 1996) and scanning electron microscopy (SEM).

Based on the above discussion, we find that the biophysical coupling between the chl-a blooms on both sides of the PF is largely the result of interannually varying physical properties determined by the TBW and TWW pools and that some of those physical properties could be easily monitored via remotely sensed observations such as (1) SST to track the extent of the TBW and TWW pools and (2) SIC to monitor the sea ice budget and sea ice retreat as an indication of vertical stability for the water column. Through the last section of this study before the Conclusions, we attempt to highlight the claim that monitoring the spatiotemporal distribution of the chl-a blooms in the BS according to satellite measurements of SST and chl-a may offer pivotal knowledge in future studies about the potential factors driving the long-term variability in the phytoplankton assemblage across the PF.

4.3.5 Monthly variations in SST and chl-a along the CIEMAR and COUPLING transects

As closure to our analyses, we return to the synoptic transects which motivated our hypothesis, based on *in situ* hydrographic and fluorescence measurements (T–I, T–II and T–III; Figures 4.2–4.4), and construct spatiotemporal climatologies of remotely sensed SST and chl-a along the same transects (for reference, a series of black dots denote the spatiotemporal position of the hydrographic stations in the Hovmöller diagrams in Figure 4.10). The aim is to highlight that the monthly variability in the easternmost extent of the chl-a bloom in the TBW pool and the westernmost extent of the chl-a bloom in the TWW pool responds closely to the monthly variability in the PF. We think this approach further supports the potential of long-term monitoring of the observed biophysical coupling via remotely sensed measurements when study boxes are properly placed according to governing ocean dynamics. From early spring (October) to early autumn (April), the PF emerges prominently along transects T–II and T–III (Figure 4.10a), where relatively warm TBW, richer in chl-a along the southern shelf of the SSI (SST >1.4ºC; chl-a ~0.7–0.8 mg m^{-3}), opposes relatively cold TWW that is poorer in chl-a (SST ~ -0.2 to -0.6ºC and chl-a < 0.3-0.4 mg m^{-3}) along the western shelf of the AP (Figure 4.10b).

It is worthwhile noting that the PF delineated along the synoptic transect T–II, found between stations 9–10 (Figure 4.3), corresponds closely to the climatological location of the PF (0.6ºC and 0.5 mg m^{-3}) observed between stations 8–9 (Figure 4.10a). Similarly, along T–III, both the hydrographic PF and the climatological PF are found at the same position, between stations T10 and T11.

As it occurred along the synoptic transect T–I (Figure 4.2), the PF is not visible along the climatological transect T–I (Figure 4.10a), where relatively warm TBW invades the strait, and the TWW signal is absent from early spring (October) to early autumn (April) with SST values ~0.2ºC. The absence of a strong cross-strait temperature gradient along T–I is in agreement with an elongated patch of high chl-a concentrations which expands towards the western shelf of the AP, reaching values of ~0.5 mg m^{-3} as far east as 84 km offshore the SSI (Figure 4.10b). This is analogous to the basin-wide high fluorescence signal shown along the synoptic transect T–I in Figure 4.2.

Throughout the remainder of the year, both SST and chl-a values follow similar patterns along the three climatological transects (T–I, T–II and T–III), displaying basin-wide, lower and more homogeneous values.

Notably, the highest chl-a concentrations are always found offshore along the three climatological transects, embedded in patches of the warmest TBW (SST >1.2–1.4ºC; chl-a ~0.6–0.8 mg m^{-3}). These climatological transects (Figure 4.10b) confirm an earlier suggestion based on Figure 4.9, where the northward spatiotemporal migration of the chl-a bloom is apparent. Here we note that the highest chl-a concentrations along the three climatological transects occur around December in T–I, in December to February in T–II and around February in T–III. In summary, the remotely sensed observations of SST and chl-a concentrations have proven to be of great potential in the monitoring of major features of the chl-a blooms in the BS, accounting for a biophysical coupling between two hydrographic scenarios (TBW and TWW pools) that confront each other along the PF. Importantly, we recall that these two hydrographic scenarios embed different phytoplankton assemblages, as has been discussed based on previous literature and results from this study.

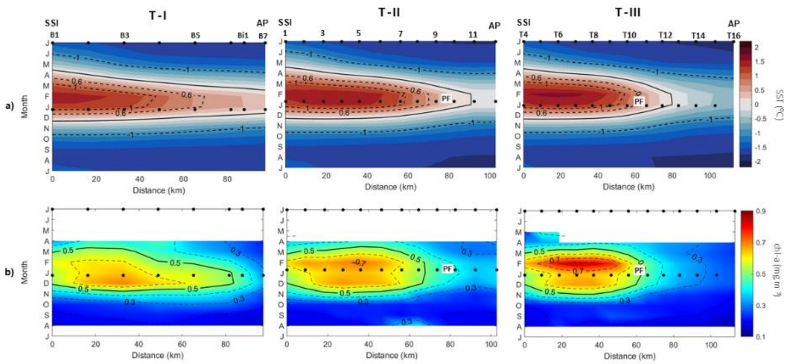

Figure 4.10. Monthly climatology from 1998 to 2018 of (a) sea surface temperature (SST) and (b) chlorophyll-a (chl-a) concentration for each study transect (see Figures 4.2-4.4) from the South Shetland Islands (SSI) to the Antarctic Peninsula (AP). The black markers (dots) situated at the top of the subplots represent the stations' positions along the transects. These same stations are also displayed during the summer months when the cruises were carried out. Additionally, the position of the Peninsula Front (PF), as identified during the cruises and located along the isopycnal of 27.55 kg m^{-3}, is also indicated.

Lastly, it is worthwhile noting that the alignment of the chl-a spatial distribution along an oceanic front is not a novel feature in the world's oceans and has already been investigated in the literature (Moore and Abbott, 2002; Baird *et al.*, 2008; Von Bodungen *et al.*, 2008). Thus, the novelty of our work lies in demonstrating through in situ observations and remotely sensed measurements that such a biophysical coupling has the potential to be used to monitor the chl-a blooms and phytoplankton assemblages occurring seasonally in the BS. This aspect is particularly relevant because the BS is a key region for the sustainability of Antarctic marine ecosystem, which is challenging to monitor due to the hazardous prevailing conditions in polar regions. In future studies, we expect the calculation of the frontal probability (Yang *et al.*, 2023) of the PF through a multi-year time series of SST data may be beneficial for interannually assessing and co-locating the alignment of the thermal front and the chl-a bloom domains using an automated algorithm for the Bransfield Strait study case (see Appendix C for further insights).

4.4 Conclusions

In this study, we address the hypothesis that the spring-to-summertime biophysical coupling controlling the chl-a bloom in the BS could be monitored through a combination of remotely sensed observations of chl-a and SST, which strongly condition the spatiotemporal variability in the phytoplankton assemblage across the PF. Our approach is based on the characterization of climatological fields, following a motivation driven by novel and historical synoptic *in situ* observations which reveal that the PF may be used as a guideline to contour two distinctive niches for phytoplankton assemblage in the BS, both horizontally and vertically.

Based on remotely sensed climatologies, we find that the surface distribution of the seasonal variation in the SST and chl-a in the BS enables the identification of two environmentally different scenarios for phytoplankton, which then grow under different strategies according to the revised literature.

The first scenario is the pool of Transitional Bellingshausen Water, relatively warm and less saline waters in a stratified water column with shallow mixed layers as compared to the second scenario. The second scenario is the pool of Transitional Weddell Water, relatively cold and more saline waters in a well-mixed water column with deeper mixed layers. We find that the climatological isotherm characterizing the PF location at the surface during the summer months corresponds to the 0.6ºC isotherm, which divides the BS in two domains. This division is further supported when we show that the isoline of 0.5 mg m^{-3} concentration of chl-a aligns with the 0.6ºC isotherm, which works well as a threshold contouring the chl-a bloom around the SSI and coherently embedding in space the region with the highest chl-a values during the summer months.

Following the seasonal climatology of the SIC, we notice that the larger freshwater inputs reported in the literature over the TBW domain and contributing to the vertical stabilization of the water column might be driven by a warmer oceanic forcing over coastal and glacial areas of the SSI (Cook *et al.*, 2016; Saenz *et al.*, 2023) rather than by melting of the open-ocean sea ice. On the other hand, the seasonal climatology of the wind stress forcing suggests that the westerlies may play a major role in contributing to (1) stratified waters in the TBW domain via downwelling-favourable Ekman transport along the southern SSI shelf, through which the Bransfield Current flows, and (2) well-mixed upper layers in the TWW domain via upwelling-favourable Ekman transport along the western AP shelf.

Moreover, based on *ad hoc* study boxes located according to the spatial distribution of the remotely sensed chl-a concentrations, we conclude that two different climatological chl-a blooms that develop simultaneously but are of a different *nature* (i.e. phytoplankton assemblage) can be identified in the BS, as suggested by their different intensities and timings (month of initiation and rate of increase). This is in agreement with former results in a series of studies which reported that cryptophytes compete in the BS, primarily with diatoms and other nanophytoplankton groups (Mura *et al.*, 1995; García-Muñoz *et al.*, 2013; Mendes *et al.*, 2013, 2023; Gonçalves-Araujo *et al.*, 2015; Mukhanov *et al.*, 2021; Costa *et al.*, 2023), following strategies to adapt better to the physical environment present throughout that year and which were displayed differently by zones in the monthly climatologies of SST, air temperature, SIC and wind stress forcing. Generally speaking, these studies have reported that TBW chl-a concentrations are commonly characterized by cryptophytes and small diatoms, while TWW chl-a concentrations are more frequently characterized by large diatoms.

We also note that the biophysical coupling between the chl-a blooms on both sides of the PF is largely the result of interannually varying physical properties determined by the TBW and TWW pools, as we revisit our results and compare them against the existing literature on phytoplankton assemblage in the BS. This suggests that the combined analysis of remotely sensed observations of chl-a and SST (as presented in this study) may be of help in elucidating the spatiotemporal variability in the two blooms that occur in the BS during the summer months from year to year. Nevertheless, we must note that a given uncertainty will still exist when it comes to knowing which phytoplankton community may dominate the TBW and the TWW pools from year to year, unless existing remotely sensed phytoplankton assemblage products are further validated in the future. We have explored such products (not shown), but the lack of a product detecting only cryptophytes hampers the assessment of their year-to-year competition with diatoms (for which a product actually exists) in the BS. We assert that this would be of paramount importance for a more comprehensive understanding of the marine ecosystem composition in the BS.

Lastly, we conclude that combined analyses of remotely sensed observations of SST and chl-a concentrations have great potential to capture major features of the chl-a blooms in the BS, accounting for a biophysical coupling between two hydrographic scenarios (TBW and TWW pools) that confronted each other along and across the PF. We think that these results highlight the importance of long-term monitoring of the spatiotemporal distribution of the chl-a blooms in the BS using satellite measurements of SST and chl-a. Such monitoring may prove pivotal for future studies investigating the forcings driving the long-term variability in the phytoplankton assemblage in the BS.

Chapter 5

Conclusions and further research

5.1 Conclusions

This chapter presents the main findings from the preceding chapters, offering a comprehensive synthesis of the insights gained throughout this research. By addressing the seasonal and spatial dynamics of the boundary currents, and biophysical coupling in the Bransfield Strait, this doctoral thesis contributes to advancing our understanding of the physical and ecological processes governing this complex marine system. The key findings presented in the following expand on prior research through novel approaches, methodologies, and extended temporal and spatial data coverage.

1. Seasonal dynamics of the Bransfield Current

The Bransfield Current has been traditionally described as a buoyancy-driven coastal jet that flows northeastward year-round along the southern slope of the South Shetland Islands. Using an extended dataset of direct velocity observations (1999–2014), this chapter confirms that the BC persists throughout all seasons, with significant spatial and seasonal variability:

- **Spatial variability**: Nelson Strait marks a transition point between upstream and downstream regions, with the BC widening downstream near King George Island. The BC's core width varies between 20–30 km upstream and broadens to 40 km downstream of Nelson Strait, aligning with changes in the bathymetry near King George Island. Volume transport increases from upstream to downstream, driven by recurrent inflows from source waters near the SSI.
- **Seasonal variability**: Volume transport remains relatively stable across seasons upstream of Nelson Strait, with values of 0.94 ± 0.15 Sv in summer, 0.88 ± 0.19 Sv in autumn, and 0.65 ± 0.13 Sv in spring.

During winter, transport reduces to 0.50 ± 0.04 Sv south of Greenwich Island. Downstream of Nelson Strait, transport increases consistently across seasons to 1.53 ± 0.17 Sv in summer, 1.29 ± 0.26 Sv in autumn, 1.20 ± 0.15 Sv in winter, and 1.22 ± 0.20 Sv in spring.

- **Vertical structure**: The BC exhibits a surface-intensified structure, with velocities decreasing significantly below 150 m. Its alignment with the islands' slope or channels further influences its spatial pattern.

These findings help identify key regions, such as the upstream BC during winter, where future sampling efforts should be concentrated to enhance our understanding and address existing observational gaps.

2. Interbasin exchange between the Bellingshausen and Weddell seas

Analysing 30 years of multi-platform satellite data, studies in chapter 3 provide climatological insights into the variability of boundary currents and their contributions to interbasin exchange based on long-term recurrent observations (as opposed to opportunistic measurements analysed in chapter 2).

- **Bransfield Current:** The BC strengthens up to King George Island across all seasons, with volume transport increasing from 0.24–0.33 Sv in the western transect to 0.52–0.64 Sv in the eastern transect in the BS (0–100 m depth). Notably, the BC shows little seasonal variability in volume transport. Heat transport peaks in summer, reaching 5.44×10^{12} W (hydrographic climatology, 0–100 m depth) and 6.67×10^{11} W (OSTIA SST product, 0–10 m depth).

- **Antarctic Coastal Current:** The CC exhibits pronounced seasonality, with volume transport oscillating between minimum values in spring and maximum values in summer, which range from 0.19–0.38 Sv in the western transect to 0.05–0.33 Sv in the eastern transect in the BS (0–100 m depth). This seasonal variability reflects the dynamic response of the CC to atmospheric and oceanographic forcings throughout the year. Heat transport also peaks in summer, with values of 2.13×10^{12} W (hydrographic climatology, 0–100 m depth) and 2.67×10^{11} W (OSTIA SST product, 0–10 m depth).

- **Winter heat transport**: Heat transport approaches zero during winter, particularly in the western transect in the BS, due to homogeneous temperatures driven by wind-induced mixing and extensive sea ice coverage.

- **Wind stress and interbasin exchange**: Both the BC and CC correlate significantly with along-strait wind stress, with the BC showing a positive correlation and the CC a negative correlation. This indicates that wind stress plays a critical role in influencing the variability of both currents, albeit in opposite directions.

- **Surface drifters**: Surface drifter data confirm the downstream broadening of the BC as a coherent northeastward-flowing jet and the continuous nature of the CC flowing southwestward along the Antarctic Peninsula during summer. These observations emphasize the challenges of characterizing the year-round variability of both currents using direct velocity measurements.

- **Modeling limitations**: Global ocean reanalysis products inadequately represent BS circulation, failing to capture the CC as a coherent feature and to reproduce observed heat transport balances.

These findings establish a baseline for understanding climate-driven changes in the boundary currents and their implications for broader Southern Ocean circulation.

3. Biophysical coupling and phytoplankton blooms

This chapter integrates data from two Antarctic cruises, CIEMAR (December 1999) and COUPLING (January 2010), and remotely sensed observations spanning 1998–2018, including chlorophyll-a, sea surface temperature, and sea ice coverage. Seasonal climatologies were constructed using these datasets to investigate the biophysical coupling driving phytoplankton blooms in the BS.

- **Two hydrographic scenarios**: The Transitional Bellingshausen Water and Transitional Weddell Water domains represent distinct ecological niches for phytoplankton assemblages, characterized by different temperature, salinity, and mixed-layer depth profiles.
- **Physical drivers**: The Peninsula Front delineates these two scenarios, with the 0.6°C isotherm and 0.5 mg m^{-3} chl-a isoline serving as thresholds. Wind stress and freshwater inputs further regulate stratification and mixing.
- **Phytoplankton strategies**: TBW blooms are dominated by cryptophytes and small diatoms, while TWW blooms feature large diatoms, with seasonal climatologies highlighting different intensities and timings.
- **Remote sensing potential**: Combined SST and chl-a observations effectively capture major features of biophysical coupling, offering a powerful tool for long-term monitoring and understanding phytoplankton variability.

These findings highlight the potential of remote sensing products to advance our understanding of interannual phytoplankton community dynamics, emphasizing the value of further validation to enhance their accuracy and applicability.

General Conclusions

This thesis provides a novel understanding of the Bransfield Strait system by integrating direct measurements, satellite data, and climatological analyses. The Bransfield Current's year-round persistence, boundary current dynamics, and the biophysical coupling driving phytoplankton blooms are all critical elements in understanding regional oceanography and its role in the Southern Ocean system. Key contributions include:

1. Comprehensive characterization of the BC's spatiotemporal variability and volume transport.
2. Identification of seasonal and spatial variability in boundary currents and their role in interbasin exchange.
3. Insights into the ecological implications of physical drivers on phytoplankton assemblages.

5.2 Further research

This research highlights several areas for further investigation:

1. **Wintertime observations**: Addressing gaps in upstream BC dynamics and boundary current variability during winter.
2. **Subsurface dynamics**: Expanding knowledge of subsurface processes influencing volume and heat transport.
3. **Phytoplankton community dynamics**: Validating remote sensing products to resolve interannual variability in phytoplankton assemblages.

4. **Model advancements**: Developing high-resolution models to better capture boundary current and biophysical coupling dynamics.

In summary, this thesis underlines the significance of long-term, multiscale observations and modeling efforts in addressing the complex interplay of physical and biological processes in polar marine systems.

Appendix A

Sea surface velocity from drifters and reanalysis output data

Here, we aim to complement the analysis of remotely sensed observations with an analysis of the historical surface drifter dataset and open-access global ocean reanalysis products to evaluate their potential for producing seasonal climatological fields that establish a baseline for comparison of the ocean circulation in the Bransfield Strait. In this way, we ensure that all possible open-access data sources have been considered in this work to describe the circulation in this region.

Figure A1 presents the seasonal data density maps of gridded surface drifter measurements (see methodology in Section 3.2.2). The numbers within each grid cell represent the number of climatological seasonal profiles available at each location per year. The density maps reveal a low number of profiles in the Bransfield Strait during autumn, winter, and spring, preventing the generation of climatological fields for these seasons. Differently, the higher data density during summer allows for such analyses. Hence, we focus on examining the horizontal velocity of the boundary currents in summer (Figure A2). This map is generated by gridding the data into 25x25 km cells, following the step-by-step time-averaging procedure described in Veny *et al*. (2022) to address the irregular spatial and temporal distribution of data. Only cells with a minimum of two profiles from different years are included in the computation. The final output map is subsequently interpolated to a 5x5 km resolution, and smoothed.

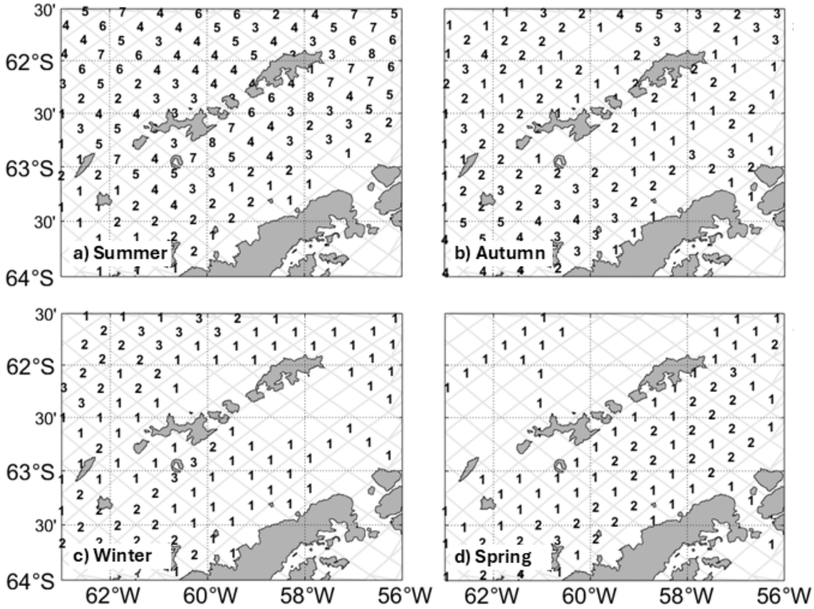

Figure A1. Maps of seasonal data density showing the amount of available climatological velocity profiles per year obtained for each grid cell of 25x25 km in the area of study, from 1979 to present. Panels follow seasons as: a) summer (Jan–Mar), b) autumn (Apr–Jun), c) winter (Jul–Sep), and d) spring (Oct–Dec).

Figure A2 represents the first map in the literature providing a comprehensive overview of the summertime surface circulation in the BS based on direct measurements, including both boundary currents. Existing circulation maps based on surface drifter data depict the BC as a coherent northeastward-flowing jet with speeds of up to 40 cm s^{-1} (Figure 3 in Zhou *et al.*, 2002; Figure 5 in Zhou *et al.*, 2006; Figure 8 in Thompson *et al.*, 2009). However, this is not the case for the CC, which frequently appears in these maps as a fragmented structure with discontinuities and counterflows over the domain near the AP. Additionally, the region where the BC and CC interact in the cross-strait direction is not well defined. The strengthening and widening of the BC are also absent in the above referred maps, where the authors use, in all cases, data spanning the entire year without distinguishing between seasons.

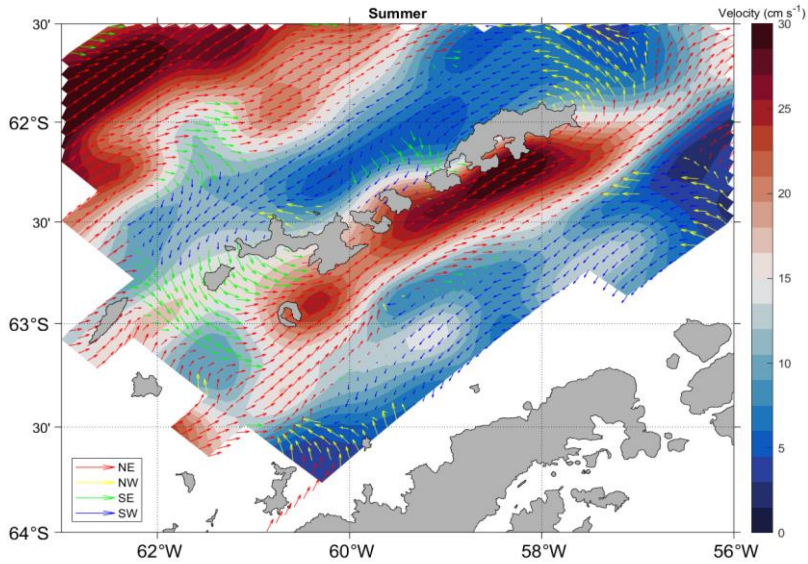

Figure A2. Map of the summer horizontal velocity field at the surface, based on drifter data (see Figure A1). Colour shading represents speed in units of cm s^{-1}, while scaled arrows indicate flow direction. Red arrows denote flows toward the northeast, yellow toward the northwest, green toward the southeast, and blue toward the southwest.

The surface circulation depicted in Figure A2 shows the BC flowing northeastward and strengthening toward King George Island, reaching velocities of 20 cm s^{-1} south of Livingston Island (WT) and up to 30 cm s^{-1} south of King George Island (ET). The BC also broadens from WT to ET, with widths of approximately 30 km and 50 km, respectively. Additionally, the BC is observed recirculating around the SSI and flowing southwestward north of the island shelves. Along the AP and within the BS, the CC flows southwestward at slower velocities, reaching up to 10 cm s^{-1}. Notably, the CC appears as a continuous feature with a coherent spatial structure across the entire strait, forming a well-defined and dynamic boundary between the two currents, which plays a critical role in the region's dynamics (Veny *et al.*, 2024). This spatial pattern, while generally characterized by stronger drifter-derived velocities, aligns with the summertime circulation revealed by altimetry data. Thus, altimetry measurements show the BC achieving maximum velocity south of King George Island (ET) at 20 cm s^{-1} (Figure 3.2) and broadening from 40 km to 55 km (Figure 3.3), while the CC exhibits slower velocities of approximately 4–6 cm s^{-1}.

Given the findings presented in this study, altimetry measurements appear to remain the only observational data source providing complete coverage of the climatological spatiotemporal variability of the boundary currents in the BS. To address this limitation, we examined two open-access global ocean reanalysis products, GLORYS12V1 and HYCOM, as potential complementary datasets, ultimately aiming to evaluate their ability to enhance our understanding of these dynamics.

Unfortunately, in both cases, the reanalysis products failed to accurately represent the BS circulation. A comparison of the monthly circulation maps from altimetry (Figure 3.3) and the reanalysis products (Figure A3) indicates that neither product captures the CC as a continuous and spatially coherent feature flowing southwestward along the AP.

To further investigate, we analysed the correlation between velocities from both reanalysis products and their respective wind stress forcing (not shown), similar to the approach used with remotely sensed altimetry and wind stress measurements (Figure 3.8). The results revealed high positive correlations across the entire strait, in contrast to the expected negative values over the CC domain. Accordingly, we hypothesize that the absence of the CC, replaced by northeastward flows, is likely due to the dominance of westerly winds in driving surface and subsurface (not shown) circulation in both reanalysis products.

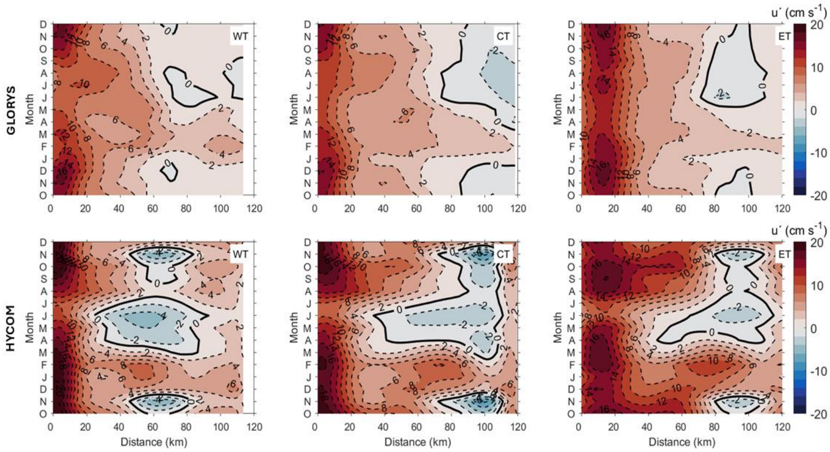

Figure A3. Hovmöller diagram of monthly climatologies of GLORYS12V1 and HYCOM surface velocity (cm s^{-1}) across the three study transects (WT, CT, and ET; see locations in Figure 3.1). The climatologies represent monthly averages for the periods January 1993 to December 2020 for GLORYS12V1 and January 1994 to December 2015 for HYCOM. Positive values (shades of red) indicate northeastward flows, while negative values (shades of blue) indicate southwestward flows. The 0 cm s^{-1} contour is emphasized with a solid, thick black line.

Appendix B
Assessment of the SST products

We assess the goodness of three available SST products by comparison with near-surface (0–1 and 10 m depth) *in situ* temperature measurements collected from a variety of Antarctic cruises (Table B1). By linear regression, the coefficient of determination (R^2) is used to evaluate the performance of the three satellite products, which are (1) Optimum Interpolation SST (OI SST; https://www.remss.com/, last access: 10 March 2022), (2) the European Space Agency Climate Change Initiative (ESA CCI; https://marine.copernicus. eu/, last access: 12 March 2022), and (3) Operational Sea Surface Temperature and Sea Ice Analysis (OSTIA; https://marine.copernicus.eu/, last access: 12 March 2022). For brevity, hereafter, we refer to them as OI SST, ESA CCI and OSTIA, respectively.

The grid spacing for OI SST is ~0.1°, but for both ESA CCI and OSTIA it is 0.05°. Meanwhile, their temporal extents are also different: the OI SST time range is from 1 June 2002 to the present, ESA CCI time range is from 1 September 1981 to 31 December 2016 and the OSTIA time range is from 1 October 1981 to 31 May 2022.

For a fair comparison, because the OI SST product starts globally in 2002, we first compare the three products to the GOAL (GOAL03, GOAL04 and GOAL05) and BREDDIES (2003) cruises at two different depths (0–1 and 10 m; see Table B2 to learn about the number of profiles by depth level used in the analysis, and Table B3 to learn about the results). Based on the low coefficients found for OI SST as compared to ESA

CCI and OSTIA (Table B3), we decide to discard OI SST for further analysis.

Lastly, we use the entire dataset of available hydrographic observations (Table B1) in the study region, making a distinction between whether we use only data falling within the Bransfield Strait (BS), the Gerlache Strait (GS) or both (full domain). These data are summarized in Table B4, where there are indications of the depth levels involved in the analysis: 0–1 m (8 cruises with 539 stations from 1990 to 2010) and 10 m (21 cruises with 1133 stations from 1990 to 2011). Results in Table B5 show the lowest coefficients are found in the Gerlache Strait for both ESA CCI and OSTIA, while these values increase when including measurements from the Bransfield Strait. To some extent, this agrees with the expectation caused by the narrow nature of the Gerlache Strait (~10 km at its narrowest part and ~50 km at its widest part). This implies the ocean in the Gerlache Strait is in close proximity to land nearly everywhere, leading to the discrepancies between remotely sensed and *in situ* observations (Zhang *et al.*, 2004; Xie *et al.*, 2008; Lee and Park, 2021).

Notably, *in situ* measurements at 10 m present a higher correlation with satellite SST everywhere (Table B5). Given the similarity of correlation coefficients for ESA CCI and OSTIA, we select OSTIA because of its longer time record, which is from 1981 to 2020, as opposed to ESA CCI, which ends earlier in 2016. This analysis was performed in 2022.

Cruise	Year	Month	Day	Season
M11/4 (*)	1990	January	1–10, 16	Summer
ANT-XII/2 (PS33)	1994	November December	26–30 1–5	Spring
FRUELA (*)	1995 1996	December January February	3–23, 26–31 2–5, 18–31 1–5	Spring Summer
IR01 (CAV95/96_4)	1996	May	8–9, 12–14	Autumn
ANT-XIV/2 (PS42)	1996	November December	15–28, 30 1, 3–6, 8–24	Spring
NBP97-05	1997	August September	4–23, 25–31 1–5	Winter
ANT-XV/4 (PS49)	1998	March April	31 1–6, 17–22	Summer Autumn
ALBATROSS (*)	1999	March April	23–26, 31 1–2	Summer Autumn
CIEMAR	1999	December	15, 18–30	Spring
BREDDIES	2002 2003	December January	30–31 2–6, 11–14, 17–18, 21	Spring Summer
GOAL03 (*)	2003	January February	23–27, 29, 31 21–23	Summer
GOAL04 (*)	2004	January	18–29	Summer
GOAL05 (*)	2005	January February	19, 21, 24–26, 28–31 1–5, 7	Summer
ANT-XXII/3 (PS67)	2005	March April	12–13, 15–19, 24, 31 1–2	Summer Autumn
SOS Climate I (*)	2008	February March	21–29 1–4	Summer
ANT-XXIV/3 (PS71)	2008	March April	25–31 1–5	Summer Autumn
JC-031	2009	February	13–14, 16–18, 20–21	Summer
SOS Climate II	2009	February March	17–28 1	Summer
COUPLING	2010	January	8–26	Summer
SOS Climate III (*)	2010	February	16–24	Summer
ANT-XXVII/2 (PS77)	2011	January	5–17	Summer

Table B1. Overview of the cruises used to calculate the coefficient of determination (see Section 2.2) and the dates they were carried out. Only cruises marked with an asterisk (*) provide data at depths of 0-1 m.

Cruise	Depth (m)	Profiles
GOAL03, GOAL04, GOAL05	0–1	190
	10	205
BREDDIES	10	61

Table B2. Number of profiles available for each cruise and depth used to analyse the goodness of available open-access remotely sensed products of sea surface temperature.

Cruise	Depth (m)	OI SST	ESA CCI	OSTIA
GOAL03, GOAL04, GOAL05 (BS and GS)	0–1	0.360	0.704	0.707
	10	0.258	0.574	0.512
BREDDIES (BS)	10	0.299	0.785	0.773

Table B3. R^2 coefficients for each SST satellite product (OI SST, ESACCI, OSTIA) compared to *in situ* SST data from four cruises' data at 0-1 and 10 m depths (see number of profiles in Table B2). The analysis is performed for different study regions: the entire study region (BS and GS) and the Bransfield Strait (BS) surroundings (excluding the GS region).

Study region	Depth (m)	Profiles
BS and GS	0–1	539
	10	1133
Gerlache Strait	0–1	417
	10	905
Bransfield Strait	0–1	122
	10	228

Table B4. The same as Table B2 but here extended to eight cruises for depths of 0-1 m and 21 cruises for depths of 10 m. Regarding the Gerlache Strait region, there are only 5 cruises available for depths of 0-1 m (ALBATROSS, FRUELA, GOAL04, GOAL05, M11/4) and 10 cruises for depths of 10 m (ALBATROSS, FRUELA, GOAL03, GOAL04, GOAL05, M11/4, IR01 (CAV95/96_4), ANT-XXVII/2 (PS77), CIEMAR, JC-031).

Study region	Depth (m)	ESA CCI	OSTIA
BS and GS	0–1	0.715	0.719
	10	0.787	0.784
Gerlache Strait	0–1	0.431	0.487
	10	0.515	0.546
Bransfield Strait	0–1	0.815	0.787
	10	0.857	0.849

Table B5. R^2 coefficients for each SST satellite product (ESACCI, OSTIA) compared to *in situ* SST data from eight cruises' data at depths of 0-1 m and 21 cruises' data at depths of 10 m (see number of profiles in Table B4). The analysis is performed for different study regions: the entire study region (BS and GS), only the Gerlache Strait (GS) and the Bransfield Strait (BS) surroundings (excluding the GS region).

Appendix C

Frontal probability of the Peninsula Front

Figure C1 presents the frontal probability (FP; Yang *et al.*, 2023) from the SST and chl-a fields in the Bransfield Strait for the period 1998–2018. The Canny edge-detection algorithm (Canny, 1986) is applied to identify coherent frontal segments. Then, the summertime FP is calculated based on three different cases, using fronts detected on daily data, monthly averaged data and seasonally averaged data over a period of 21 years (in all cases the information corresponds solely to summertime). The FP is defined at each pixel as the times that the pixel is identified as a front as a percentage of the number of total valid pixels for a given time interval.

Results support the choice of the characteristic isotherms and isoline of chl-a used in this study to distinguish two different pools of chl-a development in the BS. Additionally, we note that the signal of the Peninsula Front increases in the FP, especially in SST, when based on time-averaged fields (panels b, c, e, f) as compared to daily fields (a, d). We attribute this to the recurrence of the Peninsula Front, which is better defined when a time-averaging procedure is followed before applying the Canny edge-detection algorithm. Simultaneously, a noisier signal emerges regarding other non-recurrent fronts which are present only occasionally in time-averaged fields, thus leading to their presence only in a few fields when computing the FP.

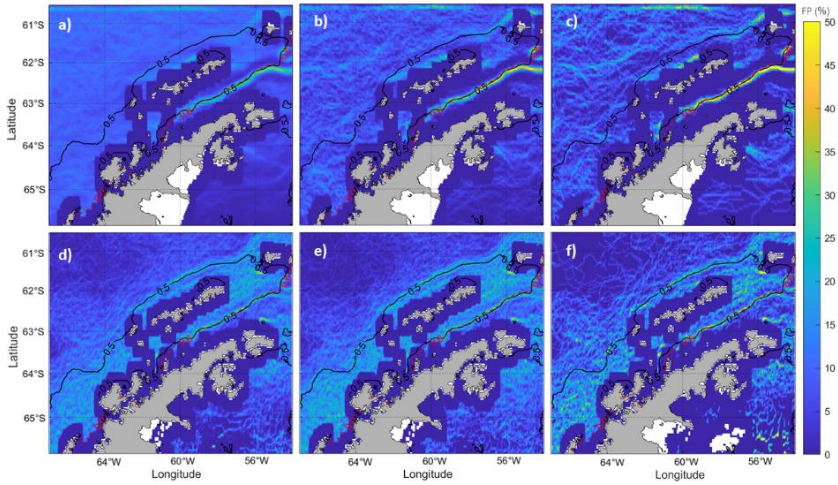

Figure C1. From left to right, the upper panels (a,b,c) show the frontal probability (FP) based on daily, monthly averaged and seasonally averaged data for sea surface temperature across 21 years of summertime. Lower panels (d,e,f) show the same as upper panels but based on chlorophyll-a (chl-a) concentrations. The climatological summertime isotherm of 0.6ºC (dashed red line) and the isoline of 0.5 mg m^{-3} chl-a concentrations (solid black line) as obtained for Figures 4.5 and 4.7 highlight the goodness of our methodology to select them as characteristic environmental values contouring the Peninsula Front in Bransfield Strait.

We suggest that the FP may be used in future studies to code an automated algorithm capable of monitoring the chl-a blooms in the Bransfield Strait based on remotely sensed SST and chl-a data, using the South Shetland Islands and the Antarctic Peninsula as physical boundaries and the Peninsula Front location as the oceanographic frontier contouring the TBW and TWW pools. Thus, interannually co-locating the alignment of the thermal front and the chl-a spatial distribution will enable the computation of accurate areas of integration for the assessment of the surface blooms acting in the Bransfield Strait.

Appendix D
Data availability

The processed 5 min averaged transect data, obtained from direct velocity measurements collected using 150 kHz 'narrow band' Shipboard Acoustic Doppler Current Profilers (SADCPs) along ship tracks from R/V *Nathaniel B. Palmer* and R/V *Laurence M. Gould*, can be accessed on the Joint Archive for Shipboard ADCP webpage (http://ilikai.soest.hawaii.edu/sadcp/index.html).

SADCP measurements with frequencies of 76.8 kHz (R/V *Akademik Sergey Vavilov*) and 38.4 kHz (R/V *Akademik Ioffe*) can be accessed on Mendeley webpage (https://data.mendeley.com/datasets/g58z4mczs7/1; Frey *et al*., 2021a).

Velocity data collected by satellite-tracked surface drifting buoys ('drifters'), are available from the NOAA Global Drifter Program (https://doi.org/10.25921/7ntx-z961; Lumpkin and Centurioni, 2010).

Ocean circulation velocity data from models can be obtained from the GLobal Ocean ReanalYsis and Simulation (GLORYS12V1; https://doi.org/10.48670/moi-00021), and the HYbrid Coordinate Ocean Model (HYCOM; https://www.hycom.org/dataserver/gofs-3pt1/reanalysis).

Climatological seasonal temperature fields are available from the Brazilian High Latitude Oceanography Group (https://zenodo.org/records/4420006; Dotto *et al*., 2021).

The remotely sensed data can be obtained from the Copernicus Marine Environment Monitoring Service (https://marine.copernicus.eu/, Copernicus, 2024) for altimeter-derived surface geostrophic eastward and northward sea water velocity (https://doi.org/10.48670/moi-00148, Global Ocean Gridded L4 Sea Surface Heights And Derived Variables Reprocessed, E. U., 2024) for sea surface temperature and sea ice concentration (https://doi.org/10.48670/moi-00168, Global Ocean OSTIA Sea Surface Temperature and Sea Ice Reprocessed, E. U., 2022; https://doi.org/10.48670/moi-00165, Global Ocean OSTIA Sea Surface Temperature and Sea Ice Analysis, E. U., 2023) and for chlorophyll-a (https://doi.org/10.48670/moi-00281, Global Ocean Colour, 2023). Reanalysis ERA5 data are available from the Copernicus Climate Change Service (https://cds.climate.copernicus.eu/, C3S, 2024) for wind and air temperature (https://doi.org/10.24381/cds.f17050d7, Hersbach *et al.*, 2023).

The BREDDIES, CIEMAR and COUPLING *in situ* data used in this work are available upon request to the corresponding author. However, *in situ* data from some cruises used for assessment of the satellite products can be obtained from PANGAEA (https://www.pangaea.de/, last access: 9 March 2022) as FRUELA 95 (https://doi.org/10.1594/PANGAEA.825643, García *et al.*, 2002a), FRUELA 96 (https://doi.org/10.1594/PANGAEA.825644, García *et al.*, 2002b), NBP97-05 (https://doi.org/10.1594/PANGAEA.761002, Gordon *et al.*, 2001), GOAL03 (https://doi.org/10.1594/PANGAEA.863598, Mata and Garcia, 2016a), GOAL04 (https://doi.org/10.1594/PANGAEA.863599, Mata and Garcia, 2016b), GOAL05 (https://doi.org/10.1594/PANGAEA.863600, Mata and Garcia, 2016c), SOS Climate I (https://doi.org/10.1594/PANGAEA.864576, Mata and Garcia, 2016d), SOS Climate II (https://doi.org/10.1594/PANGAEA.864578, Mata and Garcia, 2016e) and SOS Climate III (https://doi.org/10.1594/PANGAEA.864579, Mata and Garcia, 2016f), while the remaining data can be obtained from the World Ocean Database (https://www.ncei.noaa.gov/access/world-ocean-database-select/dbsearch.html, NOAA, 2024) defined by a number for NODC accession and/or WOD cruise reference: M11/4 (0000419 and/or DE009438), ANT-XII/2 (PS33) (9800029 and/or DE009574), IR01 (CAV95/96_4) (0000469 and/or AR001091), ANT-XIV/2 (PS42) (9900077 and/or DE009604), ANT-XV/4 (PS49) (0038589 and/or DE010544), ALBATROSS (0000861 and/or GB011122), ANT-XXII/3 (PS67) (0038589 and/or DE011945), ANT-XXIV/3 (PS71) (0038589 and/or DE012070), JC-031 (0038589 and/or GB013057) and ANT-XXVII/2 (PS77) (0038589 and/or DE012071).

Appendix E

Institutional acknowledgements

This work has been supported by the Spanish government (Ministerio de Economía y Competitividad) through the projects FLUXES (CTM2015-69392-C3-3-R), SAGA (RTI2018-100844-B-C31) and e-IMPACT (PID2019-109084RB-C21). The first author is also grateful to the Canary government (Agencia Canaria de Investigación, Innovación y Sociedad de la Información de la Consejería de Universidades, Ciencia e Innovación y Cultura) and to the Fondo Social Europeo Plus (FSE+) Programa Operativo Integrado de Canarias 2021-2027, Eje 3 Tema Prioritario 74 (85%) for the financial support awarded through a PhD scholarship (TESIS2021010025). Finally, the authors wish to thank anonymous reviewers for their thoughtful comments to improve these papers.

Appendix F
Resumen en castellano

Introducción

Este capítulo presenta una revisión de observaciones, experimentos de laboratorio y estudios de modelado provenientes de la literatura existente sobre la circulación del Estrecho de Bransfield. En primer lugar, la Sección 1.1 introduce las características más relevantes del Estrecho de Bransfield, destacando su importancia oceanográfica y ecológica. En segundo lugar, la Sección 1.2 se centra en la oceanografía del Estrecho de Bransfield, dividida en dos partes: la hidrografía y la circulación, abordando específicamente las dos principales corrientes de frontera: la Corriente de Bransfield y la Corriente Antártica Costera (Sección 1.2.1); y el acoplamiento biofísico que ocurre dentro del estrecho (Sección 1.2.2). Finalmente, la Sección 1.3 describe los propósitos y la estructura de la tesis.

1.1 Importancia oceanográfica y ecológica del Estrecho de Bransfield

Ubicado en el Océano Austral, el Estrecho de Bransfield (BS) se presenta como un laboratorio natural de características oceanográficas únicas y de profunda importancia ecológica. Este estrecho canal está situado entre las Islas Shetland del Sur (SSI) y el extremo noroeste de la Antártida (AP; Figura 1.1). El BS desempeña un papel esencial en la dinámica climática de la región debido a su ubicación geográfica, actuando como una puerta de intercambio de propiedades oceánicas impulsadas por masas de agua de origen remoto, principalmente los mares de Bellingshausen y Weddell (Grelowski *et al.*, 1986; Hofmann *et al.*, 1996; Zhou *et al.*, 2006; Sangrà *et al.*, 2017), influyendo así también en el ecosistema marino antártico (Mura *et al.*, 1995; García-Muñoz *et al.*, 2013; Mendes *et al.*, 2013, 2023; Gonçalves-Araujo *et al.*, 2015; Mukhanov *et al.*, 2021; Costa *et al.*, 2023).

Además, el BS tiene importantes implicaciones como una región representativa para observar alteraciones en las masas de agua densas de la plataforma del mar de Weddell debido a sus conexiones limitadas con los océanos circundantes y el acceso relativamente sencillo al estrecho (Dotto *et al.*, 2016). En esta región, se pueden monitorear los importantes flujos de agua fría que ingresan desde la plataforma continental del mar de Weddell hacia el BS ya que estas masas de agua actúan como un precursor clave para la formación del Agua de Fondo Antártica.

Reconocer la importancia de la región noroeste de la AP, que incluye el BS, y llevar a cabo análisis exhaustivos de estas rutas de distribución de masas de agua y su variabilidad son pasos fundamentales para obtener una comprensión integral de la dinámica climática dentro del Océano Austral. Este conocimiento también es esencial para comprender la respuesta de la región al cambio climático y su impacto más amplio en la dinámica climática global.

1.2 Oceanografía del Estrecho de Bransfield

El Estrecho de Bransfield es una región marina dinámica que sirve como una zona clave de transición, conectando el mar de Bellingshausen al oeste con el mar de Weddell al este. La confluencia de masas de agua de distintos orígenes impulsa procesos dinámicos que dan forma a sus sistemas físicos y biológicos.

1.2.1 Hidrografía y circulación

Dos corrientes de entrada principales—la Corriente de Bransfield (BC) y la Corriente Antártica Costera (CC)—configuran la circulación del estrecho y sus sistemas frontales (Figura 1.2; Grelowski *et al.*, 1986; Hofmann *et al.*, 1996; Zhou *et al.*, 2006; Sangrà *et al.*, 2017). La BC, un *jet* costero que fluye hacia el noreste, transporta Agua Transicional de Bellingshausen (TBW), relativamente más cálida (θ > -0.4ºC; Figura 1.3) y menos salina (S < 34.45) a lo largo del talud sur de SSI (Figura 1.3). Por otro lado, la CC fluye hacia el suroeste a lo largo del talud norte de la AP, llevando Agua Transicional de Weddell (TWW) más fría (θ < -0.4ºC; Figura 1.3) y salina (S > 34.45). Estas masas de agua interactúan formando estructuras mesoescalares prominentes, como el Frente de Península (PF) en superficie y el Frente de Bransfield (BF) en subsuperficie, las cuales gobiernan el acoplamiento biofísico de la región. El PF, una estructura mesoescalar superficial (~100 m de profundidad), surge de la confluencia de TBW y TWW, aproximadamente a 20-30 km del talud de la península, con un ancho de 10 km. Por el contrario, el BF delimita un frente subsuperficial más profundo (~50-400 m de profundidad), extendiéndose de 10 a 20 km a lo largo del talud de SSI, siendo más ancho y poco profundo al inicio del trayecto de la BC (Sangrà *et al.*, 2011).

Inicialmente, Niller *et al.* (1991) y Zhou *et al.* (2002, 2006) caracterizaron la BC como una corriente de frontera oeste impulsada por la rotacional negativa de la tensión del viento y el efecto β en el interior del estrecho. Sin embargo, observaciones hidrográficas *in situ* posteriores y experimentos de laboratorio realizados por Sangrà *et al.* (2011, 2017) revelaron que la BC se comporta de manera más consistente como una corriente de gravedad impulsada por flotación (ver la configuración experimental en la Figura 1.4, y la simulación de laboratorio en la Figura 1.5). Siguiendo este razonamiento, la TBW, menos densa, fluye a lo largo de la pendiente del SSI sobre la TWW más densa, confinada a una estrecha franja costera por la fuerza de Coriolis y un gradiente de presión impulsado por flotabilidad.

Ampliando los datos hidrográficos del verano, Sangrà *et al.* (2017) definieron el Sistema de la Corriente de Bransfield, identificando TBW también al norte del SSI, lo que sugiere una trayectoria de recirculación de la BC alrededor del SSI, una conclusión respaldada además por experimentos de laboratorio (ver la configuración experimental en la Figura 1.6, y la simulación de laboratorio en la Figura 1.7), así como por las trayectorias de boyas de superficie (Figura 1.8).

Antes de la publicación de los estudios presentados en esta tesis, la única sección vertical basada en observaciones que representaba la circulación a lo largo de todo el Estrecho de Bransfield, vista a partir de mediciones directas de velocidad, fue presentada en Morozov (2007; Figura 1.9).

Por lo general, la BC tiene un ancho de aproximadamente 20 km, con velocidades del *jet* central alcanzando los 40-50 cm s^{-1} cerca de la superficie (Zhou *et al.*, 2002, 2006), y disminuyendo linealmente hacia el fondo (Morozov, 2007; Savidge y Amft, 2009; Poulin *et al.*, 2014). En cambio, la CC fluye más profundamente en la columna de agua, adentrándose en el Estrecho de Bransfield con velocidades máximas alrededor de 5 cm s^{-1} (Morozov, 2007).

Más recientemente, Frey *et al.* (2023) muestran el perfil promedio de velocidad a lo largo del estrecho para las dos principales corrientes de la región, la BC y la CC, donde la última presenta un perfil casi barotrópico alrededor de 5 cm s^{-1} (Figura 1.10). Los modos de la función ortogonal empírica presentados en este análisis proporcionan una representación de cómo varían los perfiles verticales de las velocidades de la BC y la CC con la profundidad. Las diferencias entre los dos sistemas de corrientes son evidentes, con la BC mostrando un perfil baroclínico distinto con un núcleo subsuperficial a ~60 m de profundidad, mientras que la CC es mayormente barotrópica, como se había señalado previamente.

Además, los mapas de circulación basados en datos de boyas de superficie representan a la BC como un jet de flujo coherente que fluye hacia el noreste con velocidades de hasta 40 cm s^{-1} (Zhou *et al.*, 2002, 2006; Thompson *et al.*, 2009). Por el contrario, la CC a menudo aparece como una estructura más fragmentada con discontinuidades y contraflujos cerca de la Península Antártica (Figura 1.11). Es importante destacar que la interacción entre la BC y la CC en la dirección transversal al estrecho sigue sin estar bien definida. Finalmente, debemos señalar que los estudios basados en observaciones previos a esta tesis no abordan las variaciones estacionales del sistema.

En cuanto a la estructura vertical de la BC, se han reportado pocas investigaciones a partir de mediciones directas de velocidad (Morozov, 2007; Savidge y Amft, 2009; Poulin *et al.*, 2014). El estudio observacional más completo hasta la fecha, realizado por Savidge y Amft (2009), utilizó datos extensivos de SADCP recogidos entre 1997 y 2003 a bordo del R/V Nathaniel B. Palmer y el R/V Laurence M. Gould. Sus hallazgos proporcionaron una descripción detallada de la circulación de verano de la BC, revelando que el *jet* se profundiza y el transporte aumenta corriente abajo de la Isla Livingston. Las velocidades alcanzaron valores de hasta 50 cm s^{-1}, con un aumento del transporte de 1 Sv cerca del Estrecho Boyd a 2 Sv al este de la Isla Livingston (Figura 1.12a).

En invierno, Savidge y Amft (2009) reportaron que el flujo a través del Estrecho Boyd se desvía hacia el este entrando al Estrecho de Bransfield para alimentar la BC (Figura 1.12b). Sin embargo, las observaciones corriente abajo fueron insuficientes para confirmar la existencia de un fuerte *jet* hacia el este a lo largo de la plataforma sur del SSI durante el invierno. Sus datos de velocidad agrupados representaron principalmente las condiciones de verano, sin mediciones recogidas durante la primavera o el otoño. En consecuencia, la variabilidad estacional de la BC durante estos períodos de transición ha permanecido sin examinarse hasta recientemente. Wang *et al.* (2022) realizaron un estudio basado en modelos que incluye datos de salida de modelos de verano e invierno (Figura 1.13); sin embargo, la ausencia de vistas de primavera y otoño en sus análisis sigue dejando una ausencia de información crítica en la comprensión del ciclo estacional completo de la BC. Los estudios sobre la CC son aún más limitados, y totalmente ausentes en cuanto a la descripción de sus variaciones estacionales basadas en observaciones.

1.2.2 Acoplamiento biofísico

Estudios previos destacan al BS como una región de distribución irregular pero altamente productiva, con concentraciones de clorofila-a (chl-a) que a menudo superan los 3 mg m^{-3} durante el verano (Hewes *et al.*, 2009; Aracena *et al.*, 2018). Esto contrasta con el océano Antártico circundante, donde las concentraciones de chl-a generalmente oscilan entre 0.05 y 1.5 mg m^{-3} (Arrigo *et al.*, 1998; El-Sayed, 2005).

La elevada productividad en las aguas costeras del BS está estrechamente vinculada a la presencia de TBW, que presenta concentraciones de chl-a más altas en comparación con TWW (Figura 1.14). Factores como la profundidad de la capa de mezcla superficial, la estratificación de las aguas superficiales, y el aumento de las temperaturas y la disponibilidad de hierro se han relacionado con estos niveles elevados de chl-a (Hewes *et al.*, 2009).

Estudios recientes han avanzado en la comprensión de la dinámica del fitoplancton en el BS. García-Muñoz *et al.* (2013) reportaron que los ensamblajes de fitoplancton están vinculados al sistema de la Corriente de Bransfield, con el nanofitoplancton dominando en las aguas estratificadas del TBW y las diatomeas más grandes siendo más prevalentes cerca de la AP (Figura 1.15). Estos hallazgos destacan el potencial del PF para modular la estructura de la comunidad de fitoplancton y la distribución de biomasa de forma estacional.

Sin embargo, la variabilidad de la chl-a en las regiones polares no está impulsada únicamente por las características oceanográficas de las masas de agua. La dinámica del hielo marino y las fuerzas atmosféricas también juegan un papel crucial en la regulación de la producción primaria (Garibotti *et al.*, 2003; Smith *et al.*, 2008). Las variaciones impulsadas por el viento en la extensión y concentración del hielo marino influyen en la disponibilidad de luz y en el afloramiento de nutrientes, lo que complica aún más los patrones estacionales e interanuales de la chl-a (Holland y Kwok, 2012; Kusahara *et al.*, 2019).

Objetivos y esquema de la tesis

Como sugieren estudios previos, el monitoreo de la dinámica oceánica en el Océano Austral es importante para evaluar variaciones y tendencias. Por lo tanto, analizamos el noroeste de la Península Antártica, enfocándonos en aspectos físicos y biológicos.

Esta tesis tiene como objetivo evaluar, por primera vez, de forma cuantitativa y cualitativa, la variabilidad espaciotemporal de la circulación oceánica de la Corriente de Bransfield y de la Corriente Antártica Costera, así como sus implicaciones en la distribución de la clorofila-a, un elemento clave en la red trófica del ecosistema marino.

La hipótesis de trabajo es que la Corriente de Bransfield está presente durante la mayor parte del año, a pesar de que hasta ahora solo ha sido descrita durante el verano antártico. De manera complementaria, se hipotetiza que la Corriente Antártica Costera también forma parte recurrente de la dinámica oceánica del Estrecho de Bransfield, aunque su presencia a lo largo de todo el año y su variabilidad estacionalidad aún no han sido documentadas. Evaluar la variabilidad estacional de ambas corrientes de contorno proporcionará un contexto oceanográfico físico crítico para comprender los procesos de acoplamiento biofísico en el Estrecho de Bransfield. Este esfuerzo proporcionará a la comunidad científica una serie completa de climatologías hidrológicas, dinámicas y biológicas de referencia. Estas climatologías no solo mejorarán nuestra comprensión de la variabilidad natural a lo largo del margen occidental de la Península Antártica—una región polar clave en el contexto del cambio climático global—, sino que también proporcionarán campos promedio estacionales que permitirán una cuantificación estadísticamente más robusta de la importancia de eventos anómalos y tendencias en escalas de tiempo más grandes (como interanuales, decadales).

De manera complementaria, se plantea la hipótesis de que el acoplamiento biofísico de primavera a verano, que controla la variabilidad espaciotemporal del ensamblaje de fitoplancton a lo largo del Frente de Península en el Estrecho de Bransfield, también podría ser monitoreado a través de una combinación de observaciones satelitales de concentraciones de clorofila-a, temperatura superficial del mar y concentración de hielo marino.

Siguiendo lo anterior, esta tesis está estructurada en cinco capítulos. El Capítulo 1 sirve como introducción, proporcionando el contexto y los objetivos del estudio. Los Capítulos 2, 3 y 4 se centran en estudios específicos, cada uno de los cuales incluye una introducción, una descripción de los datos y métodos utilizados, los resultados obtenidos, una discusión de estos resultados y las conclusiones principales.

El Capítulo 2 presenta una climatología de las variaciones estacionales impulsadas por la Corriente de Bransfield (patrones de velocidad y transporte de volumen) durante todas las estaciones utilizando observaciones directas de velocidad. Este capítulo se publicó en *Progress in Oceanography* (Veny *et al.*, 2022).

El Capítulo 3 analiza la variabilidad mensual de las dos corrientes de frontera que fluyen a través del Estrecho de Bransfield —la Corriente de Bransfield y la Corriente Antártica Costera— utilizando datos satelitales. Este capítulo ha sido aceptado para su publicación en *Frontiers in Marine Science* (Veny *et al.*, 2025).

El Capítulo 4 examina el acoplamiento biofísico estacional en todo el Estrecho de Bransfield usando mediciones observacionales y datos satelitales. Este capítulo se publicó en *Ocean Science* (Veny *et al.*, 2024).

Finalmente, el Capítulo 5 presenta las conclusiones generales, integrando los hallazgos de los capítulos anteriores y ofreciendo una perspectiva más amplia.

Conclusiones

Este capítulo presenta los principales hallazgos de los capítulos anteriores, ofreciendo una síntesis integral de los conocimientos adquiridos a lo largo de esta investigación. Al abordar las dinámicas estacionales y espaciales de las corrientes de frontera y el acoplamiento biofísico en el Estrecho de Bransfield, esta tesis doctoral contribuye al avance en la comprensión de los procesos físicos y ecológicos que gobiernan este complejo sistema marino. Los hallazgos clave presentados a continuación amplían investigaciones previas mediante enfoques novedosos, metodologías avanzadas y una mayor cobertura temporal y espacial de los datos.

1. Dinámicas estacionales de la Corriente de Bransfield

La BC ha sido tradicionalmente descrita como una corriente costera impulsada por flotabilidad que fluye hacia el noreste a lo largo del año, bordeando la pendiente sur de las Islas Shetland del Sur. Utilizando un conjunto de datos ampliado de observaciones directas de velocidad (1999–2014), este capítulo confirma que la BC persiste durante todas las estaciones, mostrando una notable variabilidad espacial y estacional:

- **Variabilidad espacial**: El Estrecho Nelson marca un punto de transición entre las regiones corriente arriba y corriente abajo, con la BC ensanchándose corriente abajo cerca de la Isla Rey Jorge. La anchura del núcleo de la BC varía entre 20–30 km corriente arriba y se amplía a 40 km corriente abajo, en alineación con los cambios en la batimetría cerca de la Isla Rey Jorge. El transporte de volumen aumenta corriente abajo debido a flujos recurrentes de aguas provenientes de las Islas Shetland del Sur.

- **Variabilidad estacional**: El transporte de volumen se mantiene relativamente estable en las estaciones corriente arriba del Estrecho Nelson, con valores de 0.94 ± 0.15 Sv en verano, 0.88 ± 0.19 Sv en otoño y 0.65 ± 0.13 Sv en primavera. Durante el invierno, el transporte se reduce a 0.50 ± 0.04 Sv al sur de la Isla Greenwich. Corriente abajo del Estrecho Nelson, el transporte aumenta consistentemente en todas las estaciones, alcanzando 1.53 ± 0.17 Sv en verano, 1.29 ± 0.26 Sv en otoño, 1.20 ± 0.15 Sv en invierno y 1.22 ± 0.20 Sv en primavera.

- **Estructura vertical**: La BC exhibe una estructura intensificada en la superficie, con velocidades que disminuyen significativamente por debajo de los 150 m. Su alineación con la pendiente de las islas o canales influye en su patrón espacial.

Estos hallazgos identifican regiones clave, como la BC corriente arriba durante el invierno, donde deberían concentrarse los esfuerzos futuros de muestreo para mejorar la comprensión y abordar la ausencia de datos observacionales existente.

2. Intercambio entre las cuencas de los mares de Bellingshausen y Weddell

Analizando 30 años de datos satelitales multiplataforma, los trabajos en el capítulo 3 proporcionan información climatológica sobre la variabilidad de las corrientes de frontera y sus contribuciones al intercambio entre cuencas, basada en observaciones recurrentes a largo plazo (en contraste con las mediciones de oportunidad analizadas en el capítulo 2).

- **Corriente de Bransfield**: La BC se intensifica corriente abajo en todas las estaciones, con el transporte de volumen aumentando de 0.24–0.33 Sv en el transecto oeste a 0.52–0.64 Sv en el transecto este del Estrecho de Bransfield (0–100 m de profundidad). El transporte de calor alcanza su máximo en verano, con valores de 5.44×10^{12} W (climatología hidrográfica, 0–100 m) y 6.67×10^{11} W (producto SST OSTIA, 0–10 m).

- **Corriente Antártica Costera**: La CC muestra una marcada estacionalidad, con el transporte de volumen oscilando entre mínimos en primavera y máximos en verano, con valores que van de 0.19–0.38 Sv en el transecto oeste a 0.05–0.33 Sv en el transecto este del Estrecho de Bransfield (0–100 m). Esta variabilidad estacional refleja la respuesta dinámica de la CC a los forzamientos atmosféricos y oceanográficos a lo largo del año. El transporte de calor también alcanza su máximo en verano, con valores de 2.13×10^{12} W (climatología hidrográfica, 0-100 m) y 2.67×10^{11} W (producto OSTIA SST, 0–10 m).

- **Transporte de calor invernal**: El transporte de calor se aproxima a cero en invierno, particularmente en el oeste del Estrecho de Bransfield, debido a la homogeneidad térmica impulsada por la mezcla inducida por el viento y la cobertura de hielo marino.

- **Tensión del viento e intercambio entre cuencas**: Tanto la BC como la CC se correlacionan significativamente con la tensión del viento a lo largo del estrecho, mostrando la BC una correlación positiva y la CC una correlación negativa. Esto indica que la tensión del viento juega un papel fundamental en la influencia de la variabilidad de ambas corrientes, aunque en direcciones opuestas.

- **Derivadores de superficie**: Los datos de los derivadores de superficie confirman la expansión corriente abajo de la BC como un *jet* coherente que fluye hacia el noreste, y la continuidad de la CC, que fluye hacia el suroeste a lo largo de la Península Antártica durante el verano. Estas observaciones destacan los desafíos de caracterizar la variabilidad durante todo el año de ambas corrientes utilizando mediciones directas de velocidad.

- **Limitaciones de modelos**: Los productos globales de reanálisis oceánico representan de manera inadecuada la circulación del BS, no logrando capturar la CC como una característica coherente ni reproducir los balances de transporte de calor observados.

3. Acoplamiento biofísico y floraciones de fitoplancton

Este capítulo integra datos de dos campañas antárticas, CIEMAR (diciembre de 1999) y COUPLING (enero de 2010), así como observaciones remotas correspondientes al período 1998–2018, que incluyen clorofila-a, temperatura de la superficie del mar y cobertura de hielo marino. Se construyeron climatologías estacionales utilizando estos conjuntos de datos para investigar el acoplamiento biofísico que impulsa las floraciones de fitoplancton en el Estrecho de Bransfield.

- **Dos escenarios hidrográficos**: Los dominios de las TBW y las TWW representan nichos ecológicos distintos para los ensamblajes de fitoplancton, caracterizados por diferentes perfiles de temperatura, salinidad y profundidad de la capa mezclada.
- **Factores físicos**: El Frente de la Península delimita estos dos escenarios, con la isoterma de 0.6ºC y la isolínea de 0.5 mg m^{-3} de clorofila-a como umbrales. El esfuerzo del viento y las entradas de agua dulce regulan aún más la estratificación y la mezcla.
- **Estrategias del fitoplancton**: Las floraciones de TBW están dominados por criptófitos y diatomeas pequeñas, mientras que las floraciones de TWW presentan diatomeas grandes, con las climatologías estacionales destacando diferentes intensidades y tiempos.
- **Potencial de satélite**: Las observaciones combinadas de temperatura de la superficie del mar y clorofila-a capturan de manera efectiva las principales características del acoplamiento biofísico, ofreciendo una herramienta poderosa para el monitoreo a largo plazo y la comprensión de la variabilidad del fitoplancton.

Estos hallazgos destacan el potencial de los productos de satélite para avanzar en nuestra comprensión de la dinámica interanual de la comunidad de fitoplancton, enfatizando el valor de una validación adicional para mejorar su precisión y aplicabilidad.

Conclusiones Generales

Esta tesis aporta una comprensión novedosa del sistema del Estrecho de Bransfield mediante la integración de mediciones directas, datos satelitales y análisis climatológicos. La persistencia durante todo el año de la Corriente Bransfield, la dinámica de las corrientes de frontera y el acoplamiento biofísico que impulsa las floraciones de fitoplancton son elementos clave para comprender la oceanografía regional y su papel en el sistema del Océano Austral. Las contribuciones clave incluyen:

1. Caracterización exhaustiva de la variabilidad espaciotemporal de la Corriente Bransfield y su transporte de volumen

2. Identificación de la variabilidad estacional y espacial en las corrientes de frontera y su papel en el intercambio entre cuencas.

3. Perspectivas sobre las implicaciones ecológicas de los factores físicos en los ensamblajes de fitoplancton.

Futuras investigaciones

Esta investigación destaca varias áreas para futuras investigaciones:

1. **Observaciones invernales**: Abordar la ausencia de información en la dinámica de la BC corriente arriba y en la variabilidad de las corrientes de frontera durante el invierno.

2. **Dinámicas subsuperficiales**: Ampliar el conocimiento sobre los procesos subsuperficiales que influyen en el transporte de volumen y calor.

3. **Dinámica de las comunidades de fitoplancton**: Validar los productos de satélite para resolver la variabilidad interanual en los ensamblajes de fitoplancton.

4. **Avances en modelos**: Desarrollar modelos de alta resolución para capturar mejor la dinámica de las corrientes de frontera y del acoplamiento biofísico.

En resumen, este trabajo subraya la importancia de las observaciones a largo plazo y a múltiples escalas y los esfuerzos de modelado para abordar la compleja interacción entre los procesos físicos y biológicos en los sistemas marinos polares.

Bibliography

Annasawmy, P., Horne, J. K., Reiss, C. S., Cutter, G. R., & Macaulay, G. J. (2023). Antarctic krill (Euphausia superba) distributions, aggregation structures, and predator interactions in Bransfield Strait. *Polar Biology*, *46*(2), 151-168. https://doi.org/10.1007/s00300-023-03113-z.

Aracena, C., González, H. E., Garcés-Vargas, J., Lange, C. B., Pantoja, S., Muñoz, F., Teca, E., & Tejos, E. (2018). Influence of summer conditions on surface water properties and phytoplankton productivity in embayments of the South Shetland Islands. *Polar Biology*, *41*, 2135-2155. https://doi.org/10.1007/s00300-018-2338-x.

Arrigo, K. R., Worthen, D., Schnell, A., & Lizotte, M. P. (1998). Primary production in Southern Ocean waters. *Journal of Geophysical Research: Oceans*, *103*(C8), 15587-15600. https://doi.org/10.1029/98JC00930.

Atkinson, A., Siegel, V., Pakhomov, E., & Rothery, P. (2004). Long-term decline in krill stock and increase in salps within the Southern Ocean. *Nature*, *432*(7013), 100-103. https://doi.org/10.1038/nature02996.

Baird, M. E., Timko, P. G., Middleton, J. H., Mullaney, T. J., Cox, D. R., & Suthers, I. M. (2008). Biological properties across the Tasman Front off southeast Australia. *Deep Sea Research Part I: Oceanographic Research Papers*, *55*(11), 1438-1455. https://doi.org/10.1016/j.dsr.2008.06.011.

Barré, N., Provost, C., Renault, A., & Sennéchael, N. (2011). Fronts, meanders and eddies in Drake Passage during the ANT-XXIII/3 cruise in January–February 2006: A satellite perspective. *Deep Sea Research Part II: Topical Studies in*

Oceanography, *58*(25-26), 2533-2554. https://doi.org/10.1016/j.dsr2.2011.01.003.

Basterretxea, G., & Arístegui, J. (1999). Phytoplankton biomass and production during late austral spring (1991) and summer (1993) in the Bransfield Strait. *Polar Biology*, *21*, 11-22. https://doi.org/10.1007/s003000050328.

Berdalet, E., Vaqué, D., Arin, L., Estrada, M., Alcaraz, M., & Fernández, J. A. (1997). Hydrography and biochemical indicators of microplankton biomass in the Bransfield Strait (Antarctica) during January 1994. *Polar biology*, *17*, 31-38. https://doi.org/10.1007/s003000050102.

Brown, M. S., Munro, D. R., Feehan, C. J., Sweeney, C., Ducklow, H. W., & Schofield, O. M. (2019). Enhanced oceanic CO2 uptake along the rapidly changing West Antarctic Peninsula. *Nature Climate Change*, *9*(9), 678-683. https://doi.org/10.1038/s41558-019-0552-3.

C3S (Copernicus Climate Change Service) (2024). Climate Data Store (CDS), https://cds.climate.copernicus.eu/ (last access: 12 March 2022).

Canny, J. (1986). A computational approach to edge detection. *IEEE Transactions on pattern analysis and machine intelligence*, (6), 679-698. https://doi.org/10.1109/TPAMI.1986.4767851.

Catalán, I. A., Morales-Nin, B., Company, J. B., Rotllant, G., Palomera, I., & Emelianov, M. (2008). Environmental influences on zooplankton and micronekton distribution in the Bransfield Strait and adjacent waters. *Polar Biology*, *31*, 691-707. https://doi.org/10.1007/s00300-008-0408-1.

Chelton, D. B., DeSzoeke, R. A., Schlax, M. G., El Naggar, K., & Siwertz, N. (1998). Geographical variability of the first baroclinic Rossby radius of deformation. *Journal of Physical*

Oceanography, *28*(3), 433-460. https://doi.org/10.1175/1520-0485(1998)028%3C0433:GVOTFB%3E2.0.CO;2.

Chisholm, S. W., & Morel, F. M. (1991). What controls phytoplankton production in nutrient-rich areas of the open sea?. *Limnology and Oceanography, 36*, 1507–1511.

Comiso, J. C., Maynard, N. G., Smith Jr, W. O., & Sullivan, C. W. (1990). Satellite ocean color studies of Antarctic ice edges in summer and autumn. *Journal of Geophysical Research: Oceans*, *95*(C6), 9481-9496. https://doi.org/10.1029/JC095iC06p09481.

Cook, A. J., Holland, P. R., Meredith, M. P., Murray, T., Luckman, A., & Vaughan, D. G. (2016). Ocean forcing of glacier retreat in the western Antarctic Peninsula. *Science*, *353*(6296), 283-286. https://doi.org/10.1126/science.aae0017.

Copernicus (2024): Copernicus Marine Service, https://marine.copernicus.eu/ (last access: 16 February 2023).

Corzo, A., Rodríguez-Gálvez, S., Lubian, L., Sobrino, C., Sangrá, P., & Martínez, A. (2005). Antarctic marine bacterioplankton subpopulations discriminated by their apparent content of nucleic acids differ in their response to ecological factors. *Polar Biology*, *29*, 27-39. https://doi.org/10.1007/s00300-005-0032-2.

Costa, R. R., Ferreira, A., de Souza, M. S., Tavano, V. M., Kerr, R., Secchi, E. R., Brotas, V., Dotto, T. S., Brito, A. C., & Mendes, C. R. B. (2023). Physical-biological drivers modulating phytoplankton seasonal succession along the Northern Antarctic Peninsula. *Environmental Research*, *231*, 116273. https://doi.org/10.1016/j.envres.2023.116273.

Dotto, T. S., Kerr, R., Mata, M. M., & Garcia, C. A. (2016). Multidecadal freshening and lightening in the deep waters of the Bransfield Strait, Antarctica. *Journal of Geophysical Research: Oceans*, *121*(6), 3741-3756. https://doi.org/10.1002/2015JC011228.

Dotto, T.S., Mata, M., Kerr, R., & Garcia, C. (2021). A novel hydrographic gridded data set for the northern Antarctic Peninsula. *Earth System Science Data*, *13*, 671-696. https://doi.org/10.5194/essd-13-671-2021.

Ducklow, H. W., Erickson, M., Kelly, J., Montes-Hugo, M., Ribic, C. A., Smith, R. C., Stammerjohn, S. E., & Karl, D. M. (2008). Particle export from the upper ocean over the continental shelf of the west Antarctic Peninsula: A long-term record, 1992–2007. *Deep Sea Research Part II: Topical Studies in Oceanography*, *55*(18-19), 2118-2131. https://doi.org/10.1016/j.dsr2.2008.04.028.

Ducklow, H. W., Fraser, W. R., Meredith, M. P., Stammerjohn, S. E., Doney, S. C., Martinson, D. G., Sailley, S. F., Schofield, O. M., Steinberg, D. K., Venables, H. J., & Amsler, C. D. (2013). West Antarctic Peninsula: an ice-dependent coastal marine ecosystem in transition. *Oceanography*, *26*(3), 190-203. https://doi.org/10.5670/oceanog.2013.62.

Eayrs, C., Holland, D., Francis, D., Wagner, T., Kumar, R., & Li, X. (2019). Understanding the seasonal cycle of Antarctic sea ice extent in the context of longer-term variability. *Reviews of Geophysics*, *57*(3), 1037-1064. https://doi.org/10.1029/2018RG000631.

El-Sayed, S. Z. (1967). On the productivity of the southwest Atlantic Ocean and the waters west of the Antarctic Peninsula. *Biology of the Antarctic Seas III*, *11*, 15-47. https://doi.org/10.1029/AR011p0015.

El-Sayed, S. Z. (2005). History and evolution of primary productivity studies of the Southern Ocean. *Polar Biology*, *28*, 423-438. https://doi.org/10.1007/s00300-004-0685-2.

Ferrari, R., Artana, C., Saraceno, M., Piola, A. R., & Provost, C. (2017). Satellite altimetry and current-meter velocities in the Malvinas Current at 41 S: Comparisons and modes of variations. *Journal of Geophysical Research: Oceans*, *122*(12), 9572-9590. https://doi.org/10.1002/2017JC013340.

Firing, E., Hummon, J. M., & Chereskin, T. K. (2012). Improving the quality and accessibility of current profile measurements in the Southern Ocean. *Oceanography, 25*(3), 164-165.

Fischer, J., & Visbeck, M. (1993). Deep velocity profiling with self-contained ADCPs. *Journal of atmospheric and oceanic technology*, *10*(5), 764-773. https://doi.org/10.1175/1520-0426(1993)010%3C0764:DVPWSC%3E2.0.CO;2.

Frey, D., Gladyshev, S., Krechik, V., & Morozov, E. (2021a). SADCP measurements in the Bransfield Strait in 2017. Mendeley Data [data set]. https://doi.org/10.17632/g58z4mczs7.1 (last access: 28 October 2024).

Frey, D., Krechik, V., Gordey, A., Gladyshev, S., Churin, D., Drozd, I., Osadchiev, A., Kashin, S., Morozov, E., & Smirnova, D. (2023). Austral summer circulation in the Bransfield Strait based on SADCP measurements and satellite altimetry. *Frontiers in Marine Science*, *10*, 1111541. https://doi.org/10.3389/fmars.2023.1111541.

Frey, D. I., Piola, A. R., Krechik, V. A., Fofanov, D. V., Morozov, E. G., Silvestrova, K. P., Tarakanov, R. Yu., & Gladyshev, S. V. (2021b). Direct measurements of the Malvinas Current velocity structure. *Journal of Geophysical Research: Oceans*, *126*(4), e2020JC016727. https://doi.org/10.1029/2020JC016727.

García, M. A., Castro, C. G., Ríos, A. F., Doval, M. D., Rosón, G., Gomis, D., & López, O. (2002a). Physical oceanography during Hespérides cruise Fruela95. *PANGAEA* [data set]. https://doi.org/10.1594/PANGAEA.825643 (last access: 9 March 2022).

García, M. A., Castro, C. G., Ríos, A. F., Doval, M. D., Rosón, G., Gomis, D., & López, O. (2002b). Physical oceanography during Hespérides cruise Fruela96. *PANGAEA* [data set]. https://doi.org/10.1594/PANGAEA.825644 (last access: 9 March 2022).

García, M. A., Castro, C. G., Ríos, A. F., Doval, M. D., Rosón, G., Gomis, D., & López, O. (2002c). Water masses and distribution of physico-chemical properties in the Western Bransfield Strait and Gerlache Strait during Austral summer 1995/96. *Deep Sea Research Part II: Topical Studies in Oceanography*, *49*(4-5), 585-602. https://doi.org/10.1016/S0967-0645(01)00113-8.

García, M. A., López, O., Sospedra, J., Espino, M., Gracia, V., Morrison, G., Rojas, P., Figa, J., Puigdefabregas, J., & Arcilla, A. S. (1994). Mesoscale variability in the Bransfield Strait region (Antarctica) during Austral summer. *Annales Geophysicae*, *12* (9), 856-867. https://doi.org/10.1007/s00585-994-0856-z.

García-Muñoz, C., Lubián, L. M., García, C. M., Marrero-Díaz, Á., Sangra, P., & Vernet, M. (2013). A mesoscale study of phytoplankton assemblages around the South Shetland Islands (Antarctica). *Polar Biology*, *36*, 1107-1123. https://doi.org/10.1007/s00300-013-1333-5.

García-Muñoz, C., Sobrino, C., Lubián, L. M., García, C. M., Martínez-García, S., & Sangrà, P. (2014). Factors controlling phytoplankton physiological state around the South Shetland Islands (Antarctica). *Marine Ecology Progress Series*, *498*, 55-71. https://doi.org/10.3354/meps10616.

Garibotti, I. A., Vernet, M., Ferrario, M. E., Smith, R. C., Ross, R. M., & Quetin, L. B. (2003). Phytoplankton spatial distribution patterns along the western Antarctic Peninsula

(Southern Ocean). *Marine Ecology Progress Series*, *261*, 21-39. https://doi.org/10.3354/meps261021.

Gill, A. E. (1982). Atmosphere-ocean dynamics (International Geophysics Series, Volume 30). *Academic Press*.

Global Ocean Colour (Copernicus-GlobColour) (2023). Bio-Geo-Chemical, L4 (monthly and interpolated) from Satellite Observations (1997–ongoing), E. U. Copernicus Marine Service Information (CMEMS), Marine Data Store (MDS) [data set], https://doi.org/10.48670/moi-00281 (last access: 16 February 2023).

Global Ocean OSTIA Sea Surface Temperature and Sea Ice Reprocessed, E. U. (2022). Copernicus Marine Service Information (CMEMS), Marine Data Store (MDS) [data set], https://doi.org/10.48670/moi-00168 (last access: 12 March 2022).

Gomis, D., García, M. A., López, O., & Pascual, A. (2002). Quasi-geostrophic 3D circulation and mass transport in the western Bransfield Strait during Austral summer 1995/96. *Deep Sea Research Part II: Topical Studies in Oceanography*, *49*(4-5), 603-621. https://doi.org/10.1016/S0967-0645(01)00114-X.

Gonçalves-Araujo, R., de Souza, M. S., Tavano, V. M., & Garcia, C. A. E. (2015). Influence of oceanographic features on spatial and interannual variability of phytoplankton in the Bransfield Strait, Antarctica. *Journal of Marine Systems*, *142*, 1-15. https://doi.org/10.1016/j.jmarsys.2014.09.007.

Good, S., Fiedler, E., Mao, C., Martin, M. J., Maycock, A., Reid, R., Roberts-Jones, J., Searle, T., Waters, J., While, J., & Worsfold, M. (2020). The current configuration of the OSTIA system for operational production of foundation sea surface temperature and ice concentration analyses. *Remote Sensing*, *12*(4), 720. https://doi.org/10.3390/rs12040720.

Gordey, A. S., Frey, D. I., Drozd, I. D., Krechik, V. A., Smirnova, D. A., Gladyshev, S. V., & Morozov, E. G. (2024). Spatial variability of water mass transports in the Bransfield Strait based on direct current measurements. *Deep Sea Research Part I: Oceanographic Research Papers*, *207*, 104284. https://doi.org/10.1016/j.dsr.2024.104284.

Gordo Rojas, M. C. (2013). *Sistema de la Corriente del Bransfield, SCB (Antártida)* (Doctoral dissertation).

Gordon, A. L., & Nowlin Jr, W. D. (1978). The basin waters of the Bransfield Strait. *Journal of Physical Oceanography*, *8*(2), 258-264. https://doi.org/10.1175/1520-0485(1978)008%3C0258:TBWOTB%3E2.0.CO;2.

Gordon, A. L., Visbeck, M., & Huber, B. (2001). Physical oceanography during Nathaniel B. Palmer cruise NBP97-05 (DOVETAIL). *PANGAEA* [data set]. https://doi.org/10.1594/PANGAEA.761002 (last access: 9 March 2022).

Grelowski, A., Majewicz, A., & Pastuszak, M. (1986). Mesoscale hydrodynamic processes in the region of Bransfield Strait and the southern part of Drake Passage during BIOMASS-SIBEX 1983-1984. *Polish Polar Research*, *7*(4).

Haberman, K. L., Ross, R. M., & Quetin, L. B. (2003). Diet of the Antarctic krill (*Euphausia superba* Dana): II. Selective grazing in mixed phytoplankton assemblages. *Journal of Experimental Marine Biology and Ecology*, *283*(1-2), 97-113. https://doi.org/10.1016/S0022-0981(02)00467-7.

Hernández-León, S., Sangrà, P., Lehette, P., Lubián, L., Almeida, C., Putzeys, S., Bécognée, P., & Andrade, M. P. (2013). Zooplankton biomass and metabolism in the frontal zones of the Bransfield Strait, Antarctica. *Journal of Marine Systems*, *111*, 196-207. https://doi.org/10.1016/j.jmarsys.2012.11.001.

Hersbach, H., Bell, B., Berrisford, P., Biavati, G., Horányi, A., Muñoz Sabater, J., Nicolas, J., Peubey, C., Radu, R., Rozum, I., Schepers, D., Simmons, A., Soci, C., Dee, D., & Thépaut, J. N. (2023). ERA5 monthly averaged data on single levels from 1940 to present, Copernicus Climate Change Service (C3S) Climate Data Store (CDS) [data set]. https://doi.org/10.24381/cds.f17050d7 (last access: 12 March 2022).

Hersbach, H., Bell, B., Berrisford, P., Hirahara, S., Horányi, A., Muñoz-Sabater, J., Nicolas, J., Peubey, C., Radu, R., Schep- ers, D., Simmons, A., Soci, C., Abdalla, S., Abellan, X., Bal- samo, G., Bechtold, P., Biavati, G., Bidlot, J., Bonavita, M., De Chiara, G., Dahlgren, P., Dee, D., Diamantakis, M., Dragani, R., Flemming, J., Forbes, R., Fuentes, M., Geer, A., Haimberger, L., Healy, S., Hogan, R. J., Holm, E., Janiskova, M., Keeley, S., Laloyaux, P., Lopez, P., Lupu, C., Radnoti, G., de Rosnay, P., Rozum, I., Vamborg, F., Villaume, S., & Thépaut, J. N. (2020). The ERA5 global reanalysis. *Quarterly Journal of the Royal Meteorological Society*, *146*(730), 1999-2049. https://doi.org/10.1002/qj.3803.

Hewes, C. D., Reiss, C. S., & Holm-Hansen, O. (2009). A quantitative analysis of sources for summertime phytoplankton variability over 18 years in the South Shetland Islands (Antarctica) region. *Deep Sea Research Part I: Oceanographic Research Papers*, *56*(8), 1230-1241. https://doi.org/10.1016/j.dsr.2009.01.010.

Hofmann, E. E., Klinck, J. M., Lascara, C. M., & Smith, D. A. (1996). Water mass distribution and circulation west of the Antarctic Peninsula and including Bransfield Strait. *Foundations for ecological research west of the Antarctic Peninsula*, *70*, 61-80.

Holland, P. R. (2014). The seasonality of Antarctic sea ice trends. *Geophysical Research Letters*, *41*(12), 4230-4237. https://doi.org/10.1002/2014GL060172.

Holland, P. R., & Kwok, R. (2012). Wind-driven trends in Antarctic sea-ice drift. *Nature Geoscience*, *5*(12), 872-875. https://doi.org/10.1038/ngeo1627.

Holte, J., & Talley, L. (2009). A new algorithm for finding mixed layer depths with applications to Argo data and Subantarctic Mode Water formation. *Journal of Atmospheric and Oceanic Technology*, *26*(9), 1920-1939. https://doi.org/10.1175/2009JTECHO543.1.

Huneke, W. G. C., Huhn, O., & Schröeder, M. (2016). Water masses in the Bransfield Strait and adjacent seas, austral summer 2013. *Polar Biology*, *39*, 789-798. https://doi.org/10.1007/s00300-016-1936-8.

Instruments, T. R. (2013). TRDI ADCP Datasheet, Ocean Surveyor.

John D'Errico (2022). inpaint_nans (https://www.mathworks.com/matlabcentral/fileexchange/4551-inpaint_nans), MATLAB Central File Exchange [code]. Retrieved February 10, 2022.

Johnston, N. M., Murphy, E. J., Atkinson, A., Constable, A. J., Cotté, C., Cox, M., Daly, K. L., Driscoll, R., Flores, H., Halfter, S., Henschke, N., Hill, S. L., Höfer, J., Hunt, B. P. V., Kawaguchi, S., Lindsay, D., Liszka, C., Loeb, V., Manno, C., Meyer, B., Pakhomov, E. A. , Pinkerton, M. H. , Reiss, C. S. , Richerson, K., Smith Jr., W. O., Steinberg, D. K., Swadling, K. M., Tarling, G. A., Thorpe, S. E., Veytia, D., Ward, P., Weldrick, C. K., & Yang, G. (2022). Status, change, and futures of zooplankton in the Southern Ocean. *Frontiers in Ecology and Evolution*, *9*, 624692. https://doi.org/10.3389/fevo.2021.624692.

Kara, A. B., Wallcraft, A. J., Metzger, E. J., Hurlburt, H. E., & Fairall, C. W. (2007). Wind stress drag coefficient over the global ocean. *Journal of climate*, *20*(23), 5856-5864. https://doi.org/10.1175/2007JCLI1825.1.

King, M. A., & Padman, L. (2005). Accuracy assessment of ocean tide models around Antarctica. *Geophysical Research Letters*, *32*(23). https://doi.org/10.1029/2005GL023901.

Kreczmer, K., Dąbski, M., & Zmarz, A. (2021). Terrestrial Signature of a recently-tidewater glacier and adjacent periglaciation, Windy Glacier (South Shetland Islands, Antarctic). *Frontiers in Earth Science*, *9*, 299. https://doi.org/10.3389/feart.2021.671985.

Kusahara, K., Williams, G. D., Massom, R., Reid, P., & Hasumi, H. (2019). Spatiotemporal dependence of Antarctic sea ice variability to dynamic and thermodynamic forcing: A coupled ocean–sea ice model study. *Climate dynamics*, *52*, 3791-3807. https://doi.org/10.1007/s00382-018-4348-3.

La, H., Park, K., Chae, J. Y., Park, T., & Park, J. (2019). Climatic factors and their robust evidences controlling phytoplankton biomass in the Bransfield Strait. *Terrestrial, Atmospheric and Oceanic Sciences, 30,* 821–830. https://doi.org/10.3319/TAO.2019.04.30.01.

Lago, L. S., Saraceno, M., Piola, A. R., & Ruiz‐Etcheverry, L. A. (2021). Volume transport variability on the northern Argentine continental shelf from in situ and satellite altimetry data. *Journal of Geophysical Research: Oceans*, *126*(2), e2020JC016813. https://doi.org/10.1029/2020JC016813.

Large, W. G., & Pond, S. (1981). Open ocean momentum flux measurements in moderate to strong winds. *Journal of Physical Oceanography*, *11*(3), 324-336.

Lee, E. Y., & Park, K. A. (2021). Validation Satellite Sea Surface Temperature in the Coastal Regions. In *2021 IEEE*

International Geoscience and Remote Sensing Symposium IGARSS (pp. 7607-7610). https://doi.org/10.1109/IGARSS47720.2021.9553695.

Lenn, Y. D., Chereskin, T. K., Sprintall, J., & Firing, E. (2007). Mean jets, mesoscale variability and eddy momentum fluxes in the surface layer of the Antarctic Circumpolar Current in Drake Passage. *Journal of Marine Research*, *65*(1), 27-58.

Lipski, M., & Rakusa-Suszczewski, S. (1990). Early summer pattern of vertical distribution of chlorophyll-a (Bransfield Strait, Antarctica, November 1986). *Polskie Archiwum Hydrobiologii/Polish Archives of Hydrobiology*, *37*(3), 287-293.

Loeb, V., Siegel, V., Holm-Hansen, O., Hewitt, R., Fraser, W., Trivelpiece, W., & Trivelpiece, S. (1997). Effects of sea-ice extent and krill or salp dominance on the Antarctic food web. *Nature*, *387*(6636), 897-900. https://doi.org/10.1038/43174.

Loeb, V. J., Hofmann, E. E., Klinck, J. M., Holm-Hansen, O., & White, W. B. (2009). ENSO and variability of the Antarctic Peninsula pelagic marine ecosystem. *Antarctic Science*, *21*(2), 135-148. https://doi.org/10.1017/S0954102008001636.

López, O., García, M. A., Gomis, D., Rojas, P., Sospedra, J., & Sánchez-Arcilla, A. (1999). Hydrographic and hydrodynamic characteristics of the eastern basin of the Bransfield Strait (Antarctica). *Deep Sea Research Part I: Oceanographic Research Papers*, *46*(10), 1755-1778. https://doi.org/10.1016/S0967-0637(99)00017-5.

Lumpkin, R., & Centurioni, L. (2019). Global Drifter Program quality-controlled 6-hour interpolated data from ocean surface drifting buoys. NOAA National Centers for Environmental Information. [data set]. https://doi.org/10.25921/7ntx-z961 (last access: 12 December 2024).

Lüpkes, C., & Birnbaum, G. (2005). Surface drag in the Arctic marginal sea-ice zone: A comparison of different parameterisation concepts. *Boundary-Layer Meteorology*, *117*, 179-211. https://doi.org/10.1007/s10546-005-1445-8.

Macías, D., Rodríguez-Santana, Á., Ramírez-Romero, E., Bruno, M., Pelegrí, J. L., Sangrà, P., Aguiar-González, B., & García, C. M. (2013). Turbulence as a driver for vertical plankton distribution in the subsurface upper ocean. *Scientia Marina*, *77*, 541-549. https://doi.org/10.3989/scimar.03854.03A.

Mackey, M. D., Mackey, D. J., Higgins, H. W., & Wright, S. W. (1996). CHEMTAX-a program for estimating class abundances from chemical markers: application to HPLC measurements of phytoplankton. *Marine Ecology Progress Series*, *144*, 265-283. https://doi.org/10.3354/meps144265.

Marrari, M., Hu, C., & Daly, K. (2006). Validation of SeaWiFS chlorophyll-a concentrations in the Southern Ocean: A revisit. *Remote Sensing of Environment*, *105*(4), 367-375. https://doi.org/10.1016/j.rse.2006.07.008.

Mata, M. M. & Garcia, C. A. E. (2016a). Physical oceanography during Ary Rongel cruise GOAL2003. *PANGAEA* [data set]. https://doi.org/10.1594/PANGAEA.863598.

Mata, M. M. & Garcia, C. A. E. (2016b). Physical oceanography during Ary Rongel cruise GOAL2004. *PANGAEA* [data set]. https://doi.org/10.1594/PANGAEA.863599.

Mata, M. M. & Garcia, C. A. E. (2016c). Physical oceanography during Ary Rongel cruise GOAL2005. *PANGAEA* [data set]. https://doi.org/10.1594/PANGAEA.863600.

Mata, M. M. & Garcia, C. A. E. (2016d). Physical oceanography during Ary Rongel cruise SOS-Climate I. *PANGAEA* [data set]. https://doi.org/10.1594/PANGAEA.864576.

Mata, M. M. & Garcia, C. A. E. (2016e). Physical oceanography during Ary Rongel cruise SOS-Climate II. *PANGAEA* [data set]. https://doi.org/10.1594/PANGAEA.864578.

Mata, M. M. & Garcia, C. A. E. (2016f). Physical oceanography during Ary Rongel cruise SOS-Climate III. *PANGAEA* [data set]. https://doi.org/10.1594/PANGAEA.864579.

Mendes, C. R. B., Costa, R. R., Ferreira, A., Jesus, B., Tavano, V. M., Dotto, T. S., Leal, M.C., Kerr, R., Islabão, C. A., Franco, A. D., Mata, M. M., & Secchi, E. R. (2023). Cryptophytes: An emerging algal group in the rapidly changing Antarctic Peninsula marine environments. *Global Change Biology*, *29*(7), 1791-1808. https://doi.org/10.1111/gcb.16602.

Mendes, C. R. B., Tavano, V. M., Leal, M. C., de Souza, M. S., Brotas, V., & Garcia, C. A. E. (2013). Shifts in the dominance between diatoms and cryptophytes during three late summers in the Bransfield Strait (Antarctic Peninsula). *Polar Biology*, *36*, 537-547. https://doi.org/10.1007/s00300-012-1282-4.

Mitchell, B. G., & Holm-Hansen, O. (1991). Observations of modeling of the Antartic phytoplankton crop in relation to mixing depth. *Deep Sea Research Part A. Oceanographic Research Papers*, *38*(8-9), 981-1007. https://doi.org/10.1016/0198-0149(91)90093-U.

Montes-Hugo, M., Doney, S. C., Ducklow, H. W., Fraser, W., Martinson, D., Stammerjohn, S. E., & Schofield, O. (2009). Recent changes in phytoplankton communities associated with rapid regional climate change along the western Antarctic Peninsula. *Science*, *323*(5920), 1470-1473. https://doi.org/10.1126/science.1164533.

Moore, J. K., & Abbott, M. R. (2002). Surface chlorophyll concentrations in relation to the Antarctic Polar Front:

seasonal and spatial patterns from satellite observations. *Journal of Marine Systems*, *37*(1-3), 69-86. https://doi.org/10.1016/S0924-7963(02)00196-3.

Morozov, E. G. (2007). Currents in Bransfield Strait. *Doklady Earth Sciences*, *415* (2), 984-986. https://doi.org/10.1134/S1028334X07060347.

Morozov, E. G., Frey, D. I., Krechik, V. A., Polukhin, A. A., & Sapozhnikov, P. V. (2021). Water masses, currents, and phytoplankton in the Bransfield Strait in January 2020. *Antarctic Peninsula Region of the Southern Ocean: Oceanography and Ecology*, 55-64. https://doi.org/10.1007/978-3-030-78927-5_4.

Mukhanov, V. S., Sakhon, E. G., Polukhin, A. A., & Artemiev, V. A. (2021). Nanophytoplankton in the Bransfield Strait: Contribution of Cryptophyta to the Community Abundance and Biomass During Austral Summer. In: Morozov, E. G., Flint, M. V., & Spiridonov, V. A. (eds). Antarctic Peninsula Region of the Southern Ocean: Oceanography and Ecology, *Advances in Polar Ecology*, 6, 261-276. https://doi.org/10.1007/978-3-030-78927-5_20.

Münchow, A., & Garvine, R. W. (1993). Dynamical properties of a buoyancy-driven coastal current. *Journal of Geophysical Research: Oceans*, *98*(C11), 20063-20077. https://doi.org/10.1029/93JC02112.

Mura, M. P., Satta, M. P., & Agustí, S. (1995). Water-mass influences on summer Antarctic phytoplankton biomass and community structure. *Polar Biology*, *15*(1), 15-20. https://doi.org/10.1007/BF00236119.

Murzina, S. A., Voronin, V. P., Bitiutskii, D. G., Mishin, A. V., Khurtina, S. N., Frey, D. I., & Orlov, A. M. (2023). Comparative Analysis of the Fatty Acid Profiles of Antarctic Krill (Euphausia superba Dana, 1850) in the Atlantic Sector of the Southern Ocean: Certain Fatty Acids Reflect the Oceanographic and Trophic Conditions of the

Habitat. *Journal of Marine Science and Engineering*, *11*(10), 1912. https://doi.org/10.3390/jmse11101912.

Niller, P. P., Amos, A., & Hu, J. H. (1991). Water masses and 200 m relative geostrophic circulation in the western Bransfield Strait region. *Deep Sea Research Part A. Oceanographic Research Papers*, *38*(8-9), 943-959. https://doi.org/10.1016/0198-0149(91)90091-S.

NOAA (2024). World Ocean Database, NOAA, https://www.ncei.noaa.gov/access/world-ocean-database-select/dbsearch.html (last access: 25 February 2022).

Padman, L., Fricker, H. A., Coleman, R., Howard, S., & Erofeeva, L. (2002). A new tide model for the Antarctic ice shelves and seas. *Annals of Glaciology*, *34*, 247-254. https://doi.org/10.3189/172756402781817752.

Patel, R. S. (2023). Wind Stresses computation (https://www.mathworks.com/matlabcentral/fileexchange/53391-wind-stresses-computation), MATLAB Central File Exchange [code]. Retrieved December 26, 2023.

Petrou, K., Kranz, S. A., Trimborn, S., Hassler, C. S., Ameijeiras, S. B., Sackett, O., Ralph, P. J., & Davidson, A. T. (2016). Southern Ocean phytoplankton physiology in a changing climate. *Journal of Plant Physiology*, *203*, 135-150. https://doi.org/10.1016/j.jplph.2016.05.004.

Polukhin, A. A., Morozov, E. G., Tishchenko, P. P., Frey, D. I., Artemiev, V. A., Borisenko, G. V., Vidnichuk, A. V., Marina, E. N., Medvedev, E. V., Popov, O. S., Seliverstova, A. M., & Chultsova, A. L. (2021). Water structure in the Bransfield Strait (Antarctica) in January 2020: Hydrophysical, Optical, and Hydrochemical Features. *Oceanology*, *61*, 632-644. https://doi.org/10.1134/S0001437021050106.

Poulin, F. J., Stegner, A., Hernández-Arencibia, M., Marrero-Díaz, A., & Sangrà, P. (2014). Steep shelf stabilization of the coastal Bransfield Current: Linear stability analysis. *Journal* *of physical oceanography*, *44*(2), 714-732. https://doi.org/10.1175/JPO-D-13-0158.1.

Prézelin, B. B., Hofmann, E. E., Mengelt, C., & Klinck, J. M. (2000). The linkage between Upper Circumpolar Deep Water (UCDW) and phytoplankton assemblages on the west Antarctic Peninsula continental shelf. *Journal of Marine Research*, *58*(2), 165-202. https://doi.org/10.1357/002224000321511133.

Primo, C., & Vázquez, E. (2007). Ascidians collected during the Spanish Antarctic expedition CIEMAR 99/00 in the Bransfield and Gerlache Straits. *Journal of natural History*, *41*(29-32), 1775-1810. https://doi.org/10.1080/00222930701500126.

Saenz, B. T., McKee, D. C., Doney, S. C., Martinson, D. G., & Stammerjohn, S. E. (2023). Influence of seasonally varying sea-ice concentration and subsurface ocean heat on sea-ice thickness and sea-ice seasonality for a 'warm-shelf' region in Antarctica. *Journal of Glaciology*, *69*(277), 1466-1482. https://doi.org/10.1017/jog.2023.36.

Sailley, S. F., Ducklow, H. W., Moeller, H. V., Fraser, W. R., Schofield, O. M., Steinberg, D. K., Garzio, L. M., & Doney, S. C. (2013). Carbon fluxes and pelagic ecosystem dynamics near two western Antarctic Peninsula Adélie penguin colonies: an inverse model approach. *Marine Ecology Progress Series*, *492*, 253-272. https://doi.org/10.3354/meps10534.

Sangrà, P., García-Muñoz, C., García, C. M., Marrero-Díaz, Á., Sobrino, C., Mouriño-Carballido, B., Aguiar-González, B., Henríquez-Pastene, C., Rodríguez-Santana, Á., Lubián, L. M., Hernández-Arencibia, M., Hernández-León, S., & Estrada-Allis, S. N. (2014). Coupling between upper ocean layer variability and size-fractionated phytoplankton in a non-nutrient-limited environment. *Marine Ecology Progress Series*, *499*, 35-46. https://doi.org/10.3354/meps10668.

Sangrà, P., Gordo, C., Hernández-Arencibia, M., Marrero-Díaz, A., Rodríguez-Santana, A., Stegner, A., Martínez-Marrero, A., Pelegrí, J., & Pichon, T. (2011). The Bransfield current system. *Deep Sea Research Part I: Oceanographic Research Papers*, *58*(4), 390-402. https://doi.org/10.1016/j.dsr.2011.01.011.

Sangrà, P., Stegner, A., Hernández-Arencibia, M., Marrero-Díaz, Á., Salinas, C., Aguiar-González, B., Henríquez-Pastene C., & Mouriño-Carballido, B. (2017). The Bransfield gravity current. *Deep Sea Research Part I: Oceanographic Research Papers*, *119*, 1-15. https://doi.org/10.1016/j.dsr.2016.11.003.

Savidge, D. K., & Amft, J. A. (2009). Circulation on the West Antarctic Peninsula derived from 6 years of shipboard ADCP transects. *Deep Sea Research Part I: Oceanographic Research Papers*, *56*(10), 1633-1655. https://doi.org/10.1016/j.dsr.2009.05.011.

Schlitzer, R. (2016). Ocean Data View, http://odv.awi.de/.

Schofield, O., Ducklow, H. W., Martinson, D. G., Meredith, M. P., Moline, M. A., & Fraser, W. R. (2010). How do polar marine ecosystems respond to rapid climate change?. *Science*, *328*(5985), 1520-1523. https://doi.org/10.1126/science.1185779.

Siegel, D. A., Doney, S. C., & Yoder, J. A. (2002). The North Atlantic spring phytoplankton bloom and Sverdrup's critical depth hypothesis. *science*, *296*(5568), 730-733. https://doi.org/10.1126/science.1069174.

Smith, R. C., Martinson, D. G., Stammerjohn, S. E., Iannuzzi, R. A., & Ireson, K. (2008). Bellingshausen and western Antarctic Peninsula region: Pigment biomass and sea-ice spatial/temporal distributions and interannual variabilty. *Deep Sea Research Part II: Topical Studies in Oceanography*, *55*(18-19), 1949-1963. https://doi.org/10.1016/j.dsr2.2008.04.027.

Stammerjohn, S., Massom, R., Rind, D., & Martinson, D. (2012). Regions of rapid sea ice change: An inter-hemispheric seasonal comparison. *Geophysical Research Letters*, *39*(6). https://doi.org/10.1029/2012GL050874.

Stenseth, N. C., Ottersen, G., Hurrell, J. W., Mysterud, A., Lima, M., Chan, K. S., Yoccoz, N. G., & Ådlandsvik, B. (2003). Studying climate effects on ecology through the use of climate indices: the North Atlantic Oscillation, El Nino Southern Oscillation and beyond. *Proceedings of the Royal Society of London. Series B: Biological Sciences*, *270*(1529), 2087-2096. https://doi.org/10.1098/rspb.2003.2415.

Sullivan, C. W., Arrigo, K. R., McClain, C. R., Comiso, J. C., & Firestone, J. (1993). Distributions of phytoplankton blooms in the Southern Ocean. *Science*, *262*(5141), 1832-1837. https://doi.org/10.1126/science.262.5141.1832.

Teira, E., Mouriño-Carballido, B., Martínez-García, S., Sobrino, C., Ameneiro, J., Hernández-León, S., & Vázquez, E. (2012). Primary production and bacterial carbon metabolism around South Shetland Islands in the Southern Ocean. *Deep Sea Research Part I: Oceanographic Research Papers*, *69*, 70-81. https://doi.org/10.1016/j.dsr.2012.07.002.

Thomalla, S. J., Fauchereau, N., Swart, S., & Monteiro, P. M. S. (2011). Regional scale characteristics of the seasonal cycle of chlorophyll in the Southern Ocean. *Biogeosciences*, *8*(10), 2849-2866. https://doi.org/10.5194/bg-8-2849-2011.

Thompson, A. F., Heywood, K. J., Thorpe, S. E., Renner, A. H., & Trasviña, A. (2009). Surface circulation at the tip of the Antarctic Peninsula from drifters. *Journal of Physical Oceanography*, *39*(1), 3-26. https://doi.org/10.1175/2008JPO3995.1.

Tokarczyk, R. (1987). Classification of water masses in the Bransfield Strait and southern part of the Drake Passage using a method of statistical multidimensional analysis. *Polish Polar Research*, *4*(08).

Trenberth, K. E., Large, W. G., & Olson, J. G. (1990). The mean annual cycle in global ocean wind stress. *Journal of Physical Oceanography*, *20*(11), 1742-1760. https://doi.org/10.1175/1520-0485(1990)020%3C1742:TMACIG%3E2.0.CO;2.

Veny, M., Aguiar-González, B., Marrero-Díaz, Á., Pereira-Vázquez, T., & Rodríguez-Santana, Á. (2024). Biophysical coupling of seasonal chlorophyll-a bloom variations and phytoplankton assemblages across the Peninsula Front in the Bransfield Strait. *Ocean Science*, *20*(2), 389-415. https://doi.org/10.5194/os-20-389-2024.

Veny, M., Aguiar-González, B., Marrero-Díaz, Á., & Rodríguez-Santana, Á. (2022). Seasonal circulation and volume transport of the Bransfield Current. *Progress in Oceanography*, *204*, 102795. https://doi.org/10.1016/j.pocean.2022.102795.

Von Bodungen, B., John, H. C., Lutjeharms, J. R. E., Mohrholz, V., & Veitch, J. (2008). Hydrographic and biological patterns across the Angola-Benguela Frontal Zone under undisturbed conditions. *Journal of Marine Systems*, *74*(1-2), 189-215. https://doi.org/10.1016/j.jmarsys.2007.12.007.

Vorrath, M. E., Müller, J., Cárdenas, P., Opel, T., Mieruch, S., Esper, O., Lembke-Jene, L., Etourneau, J., Vieth-Hillebrand, A., Lahajnar, N., Lange, C. B., Leventer, A., Evangelinos, D., Escutia, C., & Mollenhauer, G. (2023). Deglacial and Holocene sea-ice and climate dynamics in the Bransfield Strait, northern Antarctic Peninsula. *Climate of the Past*, *19*(5), 1061-1079. https://doi.org/10.5194/cp-19-1061-2023.

Vorrath, M. E., Müller, J., Rebolledo, L., Cárdenas, P., Shi, X., Esper, O., Opel, T., Geibert, W., Muñoz, P., Haas, C., Kuhn, G., Lange, C. B., Lohmann, G., & Mollenhauer, G. (2020). Sea ice dynamics in the Bransfield Strait, Antarctic Peninsula, during the past 240 years: a multi-proxy intercomparison study. *Climate of the Past*, *16*(6), 2459-2483. https://doi.org/10.5194/cp-16-2459-2020.

Wang, X., Moffat, C., Dinniman, M. S., Klinck, J. M., Sutherland, D. A., & Aguiar-González, B. (2022). Variability and dynamics of along-shore exchange on the West Antarctic Peninsula (WAP) continental shelf. *Journal of Geophysical Research: Oceans*, *127*(2), e2021JC017645. https://doi.org/10.1029/2021JC017645.

Xie, J., Zhu, J., & Li, Y. (2008). Assessment and inter-comparison of five high-resolution sea surface temperature products in the shelf and coastal seas around China. *Continental Shelf Research*, *28*(10-11), 1286-1293. https://doi.org/10.1016/j.csr.2008.02.020.

Yang, K., Meyer, A., Strutton, P. G., & Fischer, A. M. (2023). Global trends of fronts and chlorophyll in a warming ocean. *Communications Earth & Environment*, *4*(1), 489. https://doi.org/10.1038/s43247-023-01160-2.

Zhang, H. M., Reynolds, R. W., & Smith, T. M. (2004). Bias characteristics in the AVHRR sea surface temperature. *Geophysical Research Letters*, *31*(1). https://doi.org/10.1029/2003GL018804.

Zhang, Y., Seidel, D. J., Golaz, J. C., Deser, C., & Tomas, R. A. (2011). Climatological characteristics of Arctic and Antarctic surface-based inversions. *Journal of Climate*, *24*(19), 5167-5186. https://doi.org/10.1175/2011JCLI4004.1.

Zhou, M., Niller, P. P., & Hu, J. H. (2002). Surface currents in the Bransfield and Gerlache straits, Antarctica. *Deep Sea Research Part I: Oceanographic Research Papers*, *49*(2), 267-280. https://doi.org/10.1016/S0967-0637(01)00062-0.

Zhou, M., Niller, P. P., Zhu, Y., & Dorland, R. D. (2006). The western boundary current in the Bransfield Strait, Antarctica. *Deep Sea Research Part I: Oceanographic Research Papers*, *53*(7), 1244-1252. https://doi.org/10.1016/j.dsr.2006.04.003.

Zhou, X., Zhu, G., & Hu, S. (2020). Influence of tides on mass transport in the Bransfield Strait and the adjacent areas, Antarctic. *Polar Science*, *23*, 100506. https://doi.org/10.1016/j.polar.2020.100506.